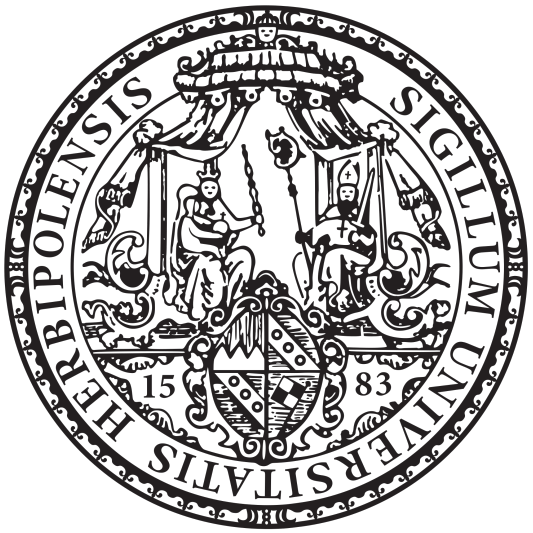

Molecular beam epitaxy and properties of magnetite thin films on semiconducting substrates

Dissertation zur Erlangung des
naturwissenschaftlichen Doktorgrades der
Julius-Maximilians-Universität Würzburg

vorgelegt von
Markus Christian Paul
aus Weißenhorn

Würzburg 2010

Eingereicht am: 03. November 2010

bei der Fakultät für Physik und Astronomie

Gutachter der Dissertation:

1. Gutachter: Prof. Dr. R. Claessen

2. Gutachter: Prof. Dr. W. Ossau

3. Gutachter: Priv.-Doz. Dr. C. W. Schneider

Prüfer im Promotionskolloquium:

1. Prüfer: Prof. Dr. R. Claessen

2. Prüfer: Prof. Dr. W. Ossau

3. Prüfer: Prof. Dr. F. Assaad

Tag des Promotionskolloquiums: 25. März 2011

Contents

List of figures

List of tables

List of acronyms

AFM	atomic force microscopy
APB	anti-phase boundary
APD	anti-phase domain
CBED	convergent beam electron diffraction
CT	charge transfer
DFT	density functional theory
DOS	density of states
EDX	energy dispersive x-ray spectroscopy
EELS	electron energy-loss spectroscopy
ESCA	electron spectroscopy for chemical analysis
EUPS	extreme ultraviolet photoelectron spectroscopy
fcc	face-centered cubic
FWHM	full width at half maximum
HAADF	high-angle annular dark field
HAXPES	hard x-ray photoelectron spectroscopy
IMFP	inelastic mean free path
LEED	low-energy electron diffraction
LSDA	local spin-density approximation
MBE	molecular beam epitaxy
PES	photoelectron spectroscopy
PLD	pulsed laser deposition
RHEED	reflection high-energy electron diffraction
SQUID	superconducting quantum interference device
STEM	scanning transmission electron microscopy
STM	scanning tunneling microscopy
TB	twin boundary
TEM	transmission electron microscopy
TEY	total electron yield
UHV	ultrahigh vacuum
VB	valence band
XAS	x-ray absorption spectroscopy
XMCD	x-ray magnetic circular dichroism
XPS	x-ray photoelectron spectroscopy
XRD	x-ray diffraction
XRR	x-ray reflectivity

Zusammenfassung

Die vorliegende Arbeit beschäftigt sich mit der Molekularstrahlepitaxie von dünnen Magnetitfilmen (Fe_3O_4) auf Halbleitersubstraten und der Charakterisierung ihrer strukturellen, chemischen, elektronischen und magnetischen Eigenschaften.

Magnetitfilme konnten auf ZnO Substraten mit hoher struktureller Qualität und scharfen Grenzflächen durch Kodeposition von Eisen und Sauerstoff gewachsen werden. Die Filme sind strukturell nahezu vollständig relaxiert und weisen innerhalb und außerhalb der Wachstumsebene annähernd die Gitterkonstante von Einkristallen auf. Weiterhin sind die hergestellten Proben phasenrein und zeigen nur an der Oberfläche und in einigen Fällen an der Grenzfläche allenfalls kleine Abweichungen von der idealen Stöchiometrie. Das Wachstum erfolgt im Stranski-Krastanov-Modus und resultiert in einer Domänenstruktur der Filme. Beim Zusammenwachsen der Inseln entstehen Antiphasengrenzen und Zwillingsgrenzen. Die Volumenmagnetisierung der Filme ist annähernd gleich der eines Einkristalls, jedoch ist das Einmündungsverhalten in die Sättigung aufgrund von reduzierter Magnetisierung an Antiphasengrenzen deutlich langsamer. Dagegen ist die Oberflächenmagnetisierung, welche mit der Methode des Röntgenzirkulardichroismus untersucht wurde, erheblich reduziert, was auf eine magnetisch inaktive Schicht an der Oberfläche schließen lässt. Diese Reduzierung der Oberflächenmagnetisierung wurde auch für Filme, die auf InAs oder GaAs deponiert wurden, beobachtet.

Ebenfalls konnte Magnetit mit nahezu idealem Eisen-Sauerstoff-Verhältnis auf InAs gewachsen werden. Bei diesem Substrat treten jedoch Grenzflächenreaktionen des Indiumarsenids mit Sauerstoff auf, die eine Arsenoxidphase und eine Indiumanreicherung bewirken. Die Filme wachsen hier nur polykristallin.

Für die Herstellung von Fe_3O_4/GaAs-Filmen wurde die Methode der Nachoxidation von epitaktischen Eisenfilmen benutzt. Das Wachstum läuft dabei durch Transformation der obersten Lagen des Eisenfilms zu Magnetit ab. Abhängig von den genauen angewandten Wachstumsbedingungen bleibt dabei eine Eisenschicht unterschiedlicher Dicke an der Grenzfläche übrig. Die strukturellen Eigenschaften sind im Vergleich zu Filmen auf InAs verbessert und die Proben sind gut entlang der [001]-Richtung orientiert. Die magnetischen Eigenschaften werden ebenfalls durch die Eisen-Grenzflächenschicht beeinflusst. Die Sättigungsmagnetisierung ist erhöht und tritt bei niedrigeren Magnetfeldern auf. Dieses Verhalten ist offenbar mit einer geringeren Dichte an Antiphasengrenzen aufgrund des andersartigen Wachstumsmechanismus verknüpft. Auftretende Grenzflächenphasen wurden quantifiziert und unterschiedliche Wachstumsbedingungen im Hinblick auf die Grenzflächenzusammensetzung verglichen.

Abstract

The present thesis is concerned with molecular beam epitaxy of magnetite (Fe_3O_4) thin films on semiconducting substrates and the characterization of their structural, chemical, electronic, and magnetic properties.

Magnetite films could successfully be grown on ZnO substrates with high structural quality and atomically abrupt interfaces. The films are structurally almost completely relaxed exhibiting nearly the same in-plane and out-of-plane lattice constants as in the bulk material. Films are phase-pure and show only small deviations from the ideal stoichiometry at the surface and in some cases at the interface. Growth proceeds via wetting layer plus island mode and results in a domain structure of the films. Upon coalescence of growing islands twin-boundaries (rotational twinning) and anti-phase boundaries are formed. The overall magnetization is nearly bulk-like, but shows a slower approach to saturation, which can be ascribed to the reduced magnetization at anti-phase boundaries. However, the surface magnetization which was probed by x-ray magnetic circular dichroism was significantly decreased and is ascribed to a magnetically inactive layer at the surface. Such a reduced surface magnetization was also observed for films grown on InAs and GaAs.

Magnetite could also be grown with nearly ideal iron-oxygen stoichiometry on InAs substrates. However, interfacial reactions of InAs with oxygen occur and result in arsenic oxides and indium enrichment. The grown films are of polycrystalline nature.

For the fabrication of Fe_3O_4/GaAs films, a postoxidation of epitaxial Fe films on GaAs was applied. Growth proceeds by a transformation of the topmost Fe layers into magnetite. Depending on specific growth conditions, an Fe layer of different thickness remains at the interface. The structural properties are improved in comparison with films on InAs, and the resulting films are well oriented along [001] in growth direction. The magnetic properties are influenced by the presence of the Fe interface layer as well. The saturation magnetization is increased and the approach to saturation is faster than for films on the other substrates. We argue that this is connected to a decreased density of anti-phase boundaries because of the special growth method. Interface phases, viz. arsenic and gallium oxides, are quantified and different growth conditions are compared with respect to the interface composition.

1 Introduction

> "We have, hopefully, convinced the reader that 98 % spin polarization is not 100 % spin polarization, even at 1.6 K." (Dowben and Skomski) [1]

Magnetite (Fe_3O_4) has been one of the most widely used and studied materials of mankind since its discovery as the first magnetic material around 1500 B.C. To name just a few examples, it bears importance as a prevalent magnetic mineral in earth's crust, as an ore material, as magnetic sensor used by certain organisms, as corrosion product of steel, as catalyst in surface science, or as magnetic device in computer memory cores and magnetic recording.

In recent years, it has above all gained huge attention from researchers as an attractive material for the nascent field of spintronics and magnetoelectronics [2]. Novel spintronic devices would combine standard microelectronics with spin-dependent effects [3]. The paradigm for such a device is the spin field-effect transistor proposed by Datta and Das [4], in which a spin-polarized current in the semiconducting channel is controlled by a gate voltage. This is analogous to a standard field effect transistor where an unpolarized current is controlled. However, the spin-polarized current can also be manipulated by the relative orientation of the ferromagnetic contacts and by the electric field from the gate, which induces a spin precession due to spin-orbit coupling.

In addition, spintronics has promised—but up to now not yet fulfilled—some major advantages over standard microelectronics such as non-volatility of data storage, increased data-processing speed, decreased electric power consumption, and increased integration densities. A current example of a magnetoelectronic effect is tunneling magnetoresistance in magnetic tunnel junctions, which are active members of magnetic random access memory or magnetic field sensors [5, 6].

In this spintronics context, the key characteristics of magnetite are its high ferrimagnetic ordering temperature of 858 K [7], a theoretically predicted spin polarization of -100 % of its conduction electrons [8], and a conductivity of $2.5 \cdot 10^4\,(\Omega m)^{-1}$ at room temperature [9], which matches well the value of semiconducting materials (cf. Secs. 2.2 and 2.3). This half-metallic density of states (DOS) at the Fermi level, E_F, resulting in -100 % spin polarization is schematized in Fig. 1.1. Majority-spin states exhibit a band gap and only minority-spin electrons are available for conduction. The mobility of the conduction electrons (0.1 to 1 cm^2/Vs [10]) is, however, significantly lower than in a normal metal.

A high spin polarization and a conductivity match are both crucial to facilitate the injection of a spin-polarized current into a semiconducting host by means of transport

across an ohmic contact [11, 12]. There are several reasons to use a standard semiconductor as the channel, inside which the spin-polarized current can be controlled. Semiconductors are versatile in terms of microstructure fabrication, doping, bipolar transport, and the possible combination with conventional electronics and technology [13]. Moreover, semiconductors, in particular GaAs [14], possess a large spin-diffusion length on the order of several micrometers and high mobilities.

The delicate question for materials science, how to combine a magnetic oxide with a semiconductor material such as Si, GaAs, InAs, or ZnO was the main motivation for the present thesis. Interestingly, reports on the growth and investigation of such hybrid structures are still relatively uncommon in the relevant literature. Besides the aspect of spintronics, the fabrication of oxide thin-film microstructures on semiconducting substrates opens up many opportunities to combine the variety of highly interesting physical properties of oxides such as magnetism, superconductivity, high-k dielectricity, or ferroelectricity with existing devices on-chip. For this reason, a clear understanding of growth processes and properties of these hybrid structures is inevitable.

However, direct oxide growth, i.e., growth without a buffer layer, onto semiconductors is often complicated because of their general differences in crystal structure and chemical bonding which can, inter alia, lead to unintended interfacial reactions (cf. Sec. 3.1.5), interdiffusion, structural defects, or relaxation behavior, all of which could influence material properties in an undesirable fashion.

While the basic physical properties of bulk magnetite are well understood, past thin-film works on magnetite concentrated mainly on using chemically inert and well lattice-matched non-semiconductor substrates such as MgO(001) [15–17] or Pt(111) [18, 19]. Since epitaxy potentially influences the atomic structure and, concurrently, the electronic and magnetic properties of a material, its physical characteristics in thin-film form have to be reanalyzed from scratch for each combination of substrate and growth method. For example, it is known that the magnetic properties of magnetite thin films are very different from bulk single crystals (cf. Sec. 2.2). Also, the spin polarization of Fe_3O_4, as determined by photoemission, is considerably lower than its predicted bulk value and ranges between $-55\,\%$ [20–22] for the free (001) surface and $-80\,\%$ [23] for the free (111) surface and $-40\,\%$ for the Fe_3O_4/γ-Al_2O_3 interface [24]. Similarly, the spin polarization deduced from junction magnetoresistance was found to be $-39\,\%$ [25] at low temperatures in case of the aforesaid interface. In this spirit, there remain many open questions on the modification of physical properties which have to be clarified.

The present thesis is organized as follows. Chapter 2 gives an overview over the relevant physical properties of magnetite, viz. its crystal structure, electronic band structure, magnetic properties, and the Verwey transition. In chapter 3, deposition and formation of a thin film and the two important characterization methods of photoelectron spectroscopy (PES) and x-ray magnetic circular dichroism (XMCD) are described in some detail. The consecutive three chapters deal with the characterization and discussion of growth results of magnetite films on the substrates ZnO, InAs, and GaAs. Here, the differences in fabrication and quality of thin films—when using these different

substrates—are highlighted. The last chapter gives a conclusion and a summary of the obtained results.

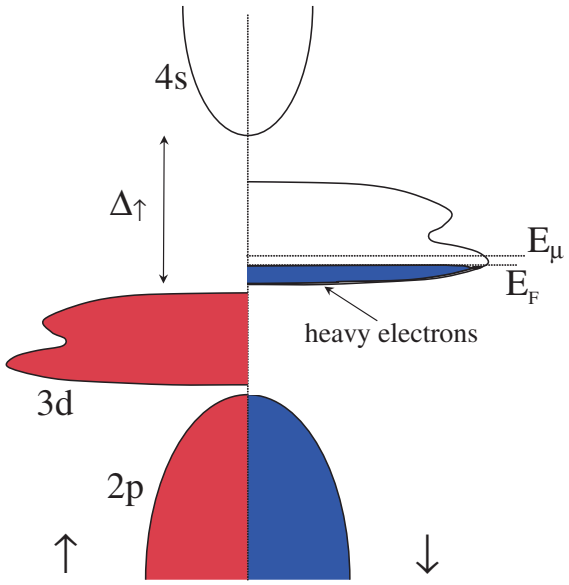

Figure 1.1: *Schematic DOS of a half-metallic ferromagnet. Only minority-spin electrons are present at the Fermi level, E_F, and majority-spin states exhibit a band gap, $\Delta_\uparrow$. The conduction electrons are in localized states with their mobility edge, E_μ, being close to E_F. In the case of magnetite conduction takes place by thermally activated hopping of electrons on octahedrally coordinated Fe sites (Fe_{oct}). The resulting conductivity is two orders of magnitude smaller than in a metal with well delocalized conduction electrons. Therefore, magnetite is often termed a 'bad' metal. Taken from Ref. [26].*

2 Physical properties of magnetite

"A physicist is the atoms' way of thinking about atoms." (Anonymous) [27]

2.1 Crystal structure

Magnetite exhibits the cubic inverse spinel structure (space group $Fd3m$) above the so-called Verwey-transition temperature. This structure is based on a face-centered cubic (fcc) lattice of oxygen anions, which is slightly distorted. The cubic unit cell (see Fig. 2.1) contains 32 oxygen anions and has a lattice constant of 8.3941 Å [28]. In addition, this unit cell hosts eight Fe^{2+} and 16 Fe^{3+} cations. Half of the Fe^{3+} cations occupy eight of the 64 available tetrahedral interstices (Fe_{tet} sites, sometimes also called A sites) of the oxygen lattice, while the other half together with the eight Fe^{2+} cations resides in 16 of the 32 available octahedral interstices (Fe_{oct} sites, sometimes also called B sites). Neighboring octahedra are edge-sharing and have a corner in common with the next tetrahedron. Due to the above mentioned distortion of the fcc O sublattice, the octahedra are weakly deformed trigonally and the tetrahedra are expanded in the direction of their corners.

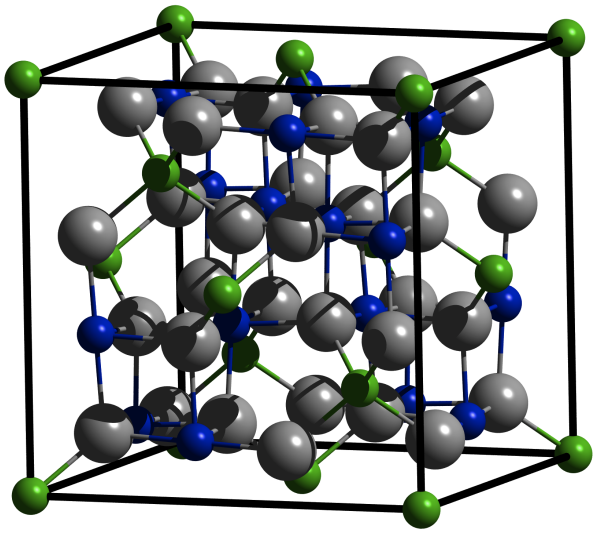

Figure 2.1: *Crystallographic unit cell of magnetite with oxygen (grey), Fe_{oct} (blue), and Fe_{tet} ions (green).*

One intriguing property of the iron oxides is that they can be stabilized over a relatively wide range of stoichiometry. For example, magnetite and maghemite can be described as end members of the solid solution phase $Fe_{3-\delta}O_4$ with δ ranging from 0 to $1/3$. Going from Fe_3O_4 towards γ-Fe_2O_3, the Fe^{2+} ions on octahedral sites are substituted by Fe^{3+} ions and vacancies ($\square$) according to the formula $\left[Fe^{3+}\right]_{tet}\left[Fe^{2+}_{1-3\delta}Fe^{3+}_{1+2\delta}\square_{\delta}\right]_{oct}O_4^{2-}$. Some important structural parameters of the different iron oxides are summarized in Tab. 2.1.

Table 2.1: *Structural parameters of different iron oxides.*

iron oxide	hematite	maghemite	magnetite	wüstite
formula	α-Fe_2O_3	γ-Fe_2O_3	Fe_3O_4	$Fe_{1-x}O$
class	hexagonal	cubic	cubic	cubic
structure	corundum	inverse spinel	inverse spinel	rock salt
space group	$R\bar{3}c$	$Fd3m$	$Fd3m$	$m\bar{3}m$
lattice constants	$a = 5.038\,\text{Å}$ $c = 13.772\,\text{Å}$	$a = 8.33\,\text{Å}$	$a = 8.3941\,\text{Å}$	$a = 4.326\,\text{Å}$
Fe sites	Fe^{3+} oct.	Fe^{3+} oct. Fe^{3+} tet.	Fe^{3+} oct. Fe^{3+} tet. Fe^{2+} oct.	Fe^{2+} oct.
Ref.	[29]	[30]	[28]	[31]

2.2 Magnetism

Bulk magnetite shows ferrimagnetism below an ordering temperature of 858 K [7]. In good approximation its magnetic structure consists of the two interpenetrating sublattices Fe_{tet} and Fe_{oct} with spin magnetic moments as for the free ions. The oxygen ions do not carry a magnetic moment since their $2p$ subshell is completely occupied. A diagram of the Fe $3d$ levels in their respective ligand-field is depicted in Fig. 2.2. The energy levels are filled up with electrons of parallel spin according to Hund's first rule because the magnetic exchange energy is larger than the respective crystal field splittings. The resulting spin magnetic moments of the sublattices are given at the bottom of Fig. 2.2. Magnetic moments of Fe^{3+}_{tet} and Fe^{3+}_{oct} are antiparallel and compensate each other. Hence, the net magnetic moment of the formula unit, viz. $4\,\mu_B$, is due to the Fe^{2+}_{oct} sites. The orbital magnetic moments can be considered as quenched inside the bulk material owing to their coupling to the lattice.

As an extension of the strictly ionic picture the minority-spin electron on the Fe_{oct} sites is mobile and can hop back and forth across the connecting oxygen ion via double-exchange (see label "DE" in Fig. 2.2). The electron is delocalized over the Fe-O-Fe group and effects the mixed valency of the Fe_{oct} sites and the relatively large conductivity of magnetite compared to other oxides. The density of these itinerant charge carriers is directly determined by the density of Fe^{2+}_{oct} ions.

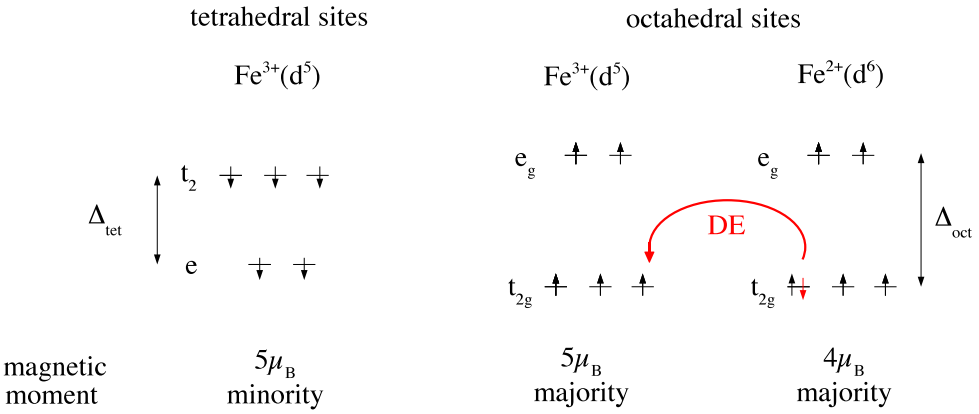

Figure 2.2: *Electronic Fe 3d levels and resulting magnetic moments in the independent electron ligand-field model with high-spin configuration. The Fe 3d levels are split by the tetrahedral and octahedral crystal field stabilization energy, Δ_{tet} and Δ_{oct}, respectively, and filled according to Hund's first rule since the magnetic exchange energy is larger than the crystal field splittings. Magnetic moments of Fe^{3+}_{tet} and Fe^{3+}_{oct} are antiparallel which results in a vanishing net magnetization from these sites. The entire net magnetization results from the moments of Fe^{2+}_{oct} sites.*

The ferrimagnetic order depicted in Fig. 2.2 was first proposed by Néel [32]. It is a consequence of the different indirect, i.e., oxygen-mediated, exchange interactions between Fe ions in the crystal structure. The strongest magnetic coupling of the moments is via the 127° Fe_{tet}-O-Fe_{oct} linkage and is antiferromagnetic super-exchange. This inter-sublattice coupling has an exchange integral of $J_{\text{tet-oct}} = -33.4\,\text{K}$ [33]. Furthermore, the intra-sublattice exchange integrals are $J_{\text{tet-tet}} = -2.1\,\text{K}$ via antiferromagnetic super-exchange and $J_{\text{oct-oct}} = 9.6\,\text{K}$ via ferromagnetic double-exchange due to the mixed valency on Fe_{oct} sites [33].

The Curie temperature of the system, T_C, can be calculated in the mean-field approximation of the two-sublattice model. In the model it depends not only on the exchange integrals but also on the magnitude and number of the magnetic moments and therefore can be much larger than the exchange integrals themselves. Uhl and Siberchicot, e.g., calculated $T_C = 1612\,\text{K}$ for the exchange integrals given above [33].

Without double-exchange interaction the Néel magnetic order is present in the limit $J_{\text{tet-oct}} \gg J_{\text{oct-oct}},\ J_{\text{tet-tet}}$. Yafet and Kittel showed that if $J_{\text{oct-oct}}$ is increased and $J_{\text{tet-oct}}$ is reduced, the Fe_{oct} site moments can be canted with respect to the Fe_{tet} site moments [34]. This canting by the so-called Yafet-Kittel angle causes a lowering of the saturation magnetization in finite fields. Other non-collinear spin structures can occur in disordered spinels [35].

Magnetometry proves a saturation moment of $\mu_S = 4.05\,\mu_B$ per formula unit at 4.2 K [36], which is very close to the net magnetization of $\mu_S = 4\,\mu_B$/f.u. expected in the ionic picture. This experimental value decreases with temperature yielding $3.83\,\mu_B$/f.u.

at room temperature [7] (cf. Fig. 2.5(a)). The saturation magnetic moment also varies with the off-stoichiometry parameter δ (see Sec. 2.1). Theoretically, in the simple ionic model it is $3^1/_3\,\mu_B$ for $\delta = 1/3$ [36, 37]. These values are consistent with saturation magnetizations of 97 and $80\,\mathrm{Am^2/kg}$ for magnetite and maghemite, respectively [38]. The saturation magnetization of the $Fe_{3-\delta}O_4$ phase at room temperature can be estimated by:

$$\mu_S = \frac{3.83}{4} \cdot (4 - 2\delta)\ [\mu_B/\text{f.u.}]. \tag{2.1}$$

Measurements of the magnetic moments obtained by means of polarized neutron diffraction, which probes the local magnetic moments of a compound, yielded $3.82\,\mu_B$ for Fe_{tet} and $3.97\,\mu_B$ for all Fe_{oct} [39]. Although the single moments are significantly different from the integer moments as for free ions, a ferrimagnetic ordering of the Néel-type results in a similar net magnetization.

While the filling of electronic levels is responsible for the size of the moments, the magnetization direction is determined by the magnetic anisotropy energy. Magnetocrystalline anisotropy is the decisive energy in the case of a spherical single crystal. The magnetocrystalline anisotropy constant of bulk magnetite is $K_1 = -1.1 \cdot 10^4\,\mathrm{J/m^3}$ corresponding to an anisotropy field of $\mu_0 H = 30.5\,\mathrm{mT}$ [7], which leads to the easy, intermediate, and hard magnetization directions pointing along [111], [110], and [100], respectively [38]. Magnetocrystalline anisotropy arises mainly from spin-orbit coupling and is a very small correction to the magnetic energy.

In thin films the shape anisotropy energy is the dominating contribution to the magnetic energy for out-of-plane orientation of the applied magnetic field. For this reason, the magnetization is usually oriented in-plane. The shape anisotropy constant and the respective shape anisotropy field are $K_{shape} = 2\pi M_S^2 = 1.39 \cdot 10^5\,\mathrm{J/m^3}$ and $\mu_0 H_{shape} = 2\mu_0 K_{shape}/M_S = 0.6\,\mathrm{T}$ [7].

However, the behavior of magnetite thin films is anomalous compared to bulk single crystals as they are difficult to saturate, behave superparamagnetically, are out-of-plane magnetized in zero field, or possess an irregular magnetic domain structure [40, 41]. Concurrent torque measurements, however, revealed no additional anisotropy in excess of the expected combination of shape, magnetocrystalline, and magnetoelastic anisotropy that could explain the slow saturation behavior [40]. These facts have been ascribed to the existence of anti-phase boundaries (APBs) inside the 'volume' of the films, which introduce additional magnetic couplings at their position inside the crystal [42, 43].

An APB is a two-dimensional structural defect at which the cation sublattice shifts by a vector smaller than the lattice constant in such a manner that the cation sublattice gets out of phase at the boundary. The O sublattice, however, is perfect across such a boundary, and a sample containing only APBs is therefore still monocrystalline. Possible APB shift vectors in magnetite belong either to the $1/2\langle 100\rangle$ or the $1/4\langle 110\rangle$ family of directions. Celotto *et al.* showed for the case of Fe_3O_4/MgO(001) that about 45 % of the phase shifts are in-plane with their boundary plane being perpendicular to the shift and the remaining 55 % of the phase shifts are out-of-plane with their boundary plane being

not perpendicular to the shift but either oriented close to the {100} or {310} family of planes [44].

The new cation arrangement at an APB with bond lengths and bond angles different from the bulk induces new exchange interactions at the boundary. In summary, this results in an enhanced antiferromagnetic interaction between Fe_{tet} sites, in a strongly reduced Fe_{tet}-Fe_{oct} interaction and a very strong antiferromagnetic interaction between Fe_{oct} sites [42]. Thus, both intra-sublattice spin couplings are dominant and antiferromagnetic at an APB, which produces spin canting different from the ferromagnetic spin arrangement inside the domains. Since the magnetic moments at the APB can only be aligned in very large fields, this leads to magnetization values lower than the bulk magnetization in finite fields and to a slow approach to saturation. In addition APBs can act as pinning and nucleation sites of domain walls depending on the local magnetic coupling [45].

Margulies *et al.* [42] have shown that the approach to saturation magnetization is similar to the model case of a one-dimensional chain of ferromagnetically coupled spins with an additional antiferromagnetic coupling at the APB. This one-dimensional model was first discussed by Zijlstra [45] and Dieny *et al.* [46]. It describes the competition between the Zeeman energy in the domains and the new exchange energy at the APB but neglects the magnetocrystalline anisotropy. Insofar, APBs are treated analogously to Bloch walls. However, the width of the APBs is controlled by the external magnetic field and not by the magnetocrystalline field. In this model, the slow approach to the saturation magnetization, M_S, can be described by the law:

$$M = M_S(1 - b/H^{1/2}). \tag{2.2}$$

Here, the parameter b, which describes the difficulty to saturate the film, is proportional to the APB density, ρ. Later, this law of approach to saturation was applied also by Hibma *et al.* [43], and Bataille *et al.* [47, 48]. Bataille *et al.* [48] extended the model to the case of two APBs per chain. They showed that for small APB separations the inner anti-phase domain (APD) is magnetized in the opposite direction and that for fields below a critical value the magnetization inside each single domain is homogeneous. They also found that the extended model is consistent with the weaker dependency of the saturation approach on the APB density: $b(\rho) = \rho^{1/3}$. So, although the one-dimensional model is surely an oversimplification, the law of approach to saturation in Eq. (2.2) still shows a reasonable agreement with experimental data and therefore is employed by many authors.

More recent off-axis electron holography observations of a thin $Fe_3O_4(001)$ film demonstrated that the actual magnetic microstructure is much more complicated and that magnetic domain sizes do not exhibit perfect correspondence to APD sizes [49]. Furthermore, it was found by Kasama *et al.* that the magnetic moment can be aligned out-of-plane locally at APBs and that the coupling between APDs can be antiferromagnetic, although this occurs in less than 10 % of all cases [49].

2.3 Electronic band structure

A localized-electron picture was used to present some magnetic properties of magnetite. In the following, its electronic band structure is explained as described by density functional theory (DFT), which elucidates the itinerant character of the $3d$ electrons and their band formation. However, one has to bear in mind that DFT in the local spin-density approximation (LSDA) only gives a good account for the ground state at zero temperature for systems without strong electron correlation.

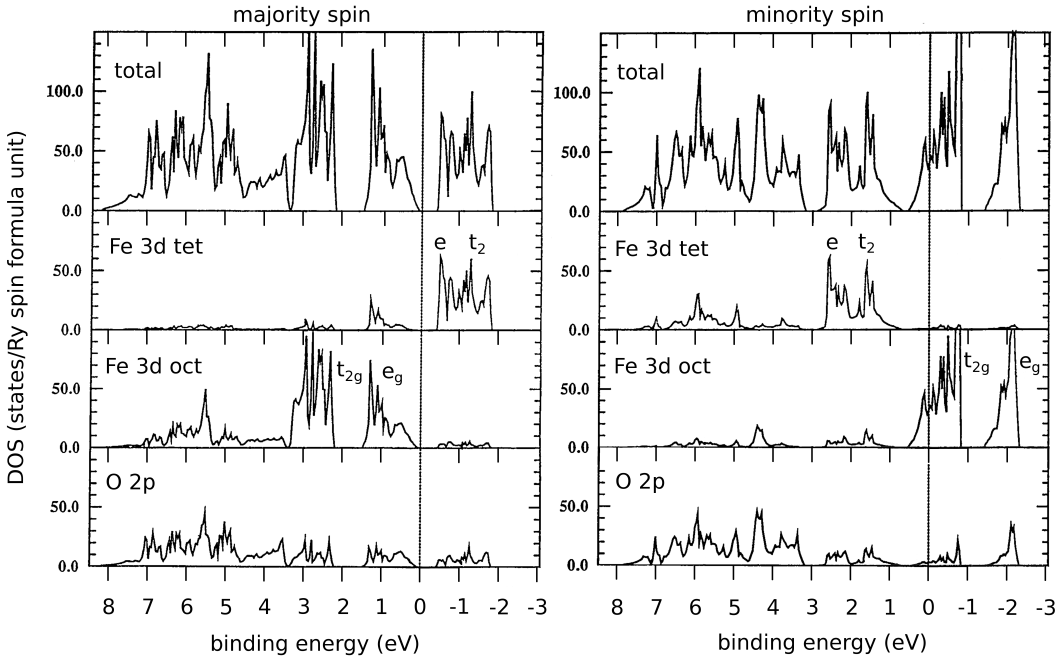

Figure 2.3: *Spin-decomposed, total and site-decomposed DOS calculated by means of DFT in the LSDA approximation by Yanase and Hamada. Adopted from Ref. [8].*

Figure 2.3 displays the site- and spin-decomposed DOS of magnetite from an LSDA calculation by Yanase and Hamada. Majority- and minority-spin states in the binding-energy range from 3.5 to 8 eV are mainly of O $2p$ character with some minor hybridization with Fe $3d$ states. So, similar to the ionic picture O has its $2p$ subshell completely filled. States from from -3 to 3.5 eV are predominantly Fe $3d$-like. $\mathrm{Fe_{oct}}$ states are split into t_{2g} and e_g sets of orbitals by a crystal field stabilization energy of about 2 eV. Analogously, $\mathrm{Fe_{tet}}$ states are split into t_2 and e sets by about 1 eV. The magnetic exchange splitting of about 3.5 eV causes an energy shift of minority- and majority-spin Fe $3d$ states against each other like in a Stoner-model. For $\mathrm{Fe_{oct}}$ the majority-spin states are completely, but the minority-spin states only partially filled. The exchange splitting of $\mathrm{Fe_{tet}}$ states is the other way around, and the majority-spin states are empty, and the minority-spin states

completely occupied. Most importantly, the total majority-spin DOS exhibits an energy gap of about 0.5 eV at E_F, but the minority-spin Fe_{oct} states cross E_F, which results in a half-metallic, ferrimagnetic electronic structure.

Most of the DFT calculations up to now support this half-metallic band picture of magnetite in the high-temperature phase, independently of the particularly used variant, viz. augmented plane-wave [8, 50], augmented spherical wave [37, 51], linear muffin-tin orbital [52–54], or LSDA+U [54]. On the contrary, self-interaction corrected LSDA calculations, which are believed to treat electronic correlations more accurately, by Szotek *et al.* indicated that the inverse spinel order of Fe ions exhibits an insulating ground state [6, 55], and that furthermore the scenario with all Fe ions being trivalent (Fe^{3+}) possesses a lower total energy [56].

DFT calculations are not able to elucidate the exact magnetic moments of the Fe sites. As Penicaud *et al.* [37] have pointed out DFT calculations yielding a band gap in one spin channel imply integer numbers of majority and minority spins. Consequently, the magnetic moment is an integer number of Bohr magnetons as well. In contrast, a magnetic moment calculated directly by DFT in LSDA using an integration over a charge density generally will be a non-integer number, but depends on the choice of the integration radius around a nucleus and therefore is somewhat arbitrary.

2.4 Verwey transition

Magnetite undergoes the so-called Verwey transition at a temperature of about $T_V = 120$ K [57, 58]. Besides a structural change from the cubic high-temperature structure to a monoclinic one, the transition is observed as a sharp drop of the conductivity by two orders of magnitude and as anomalies in other physical properties such as the magnetization [40, 59] or heat capacity [60]. From the beginning, the Verwey transition was interpreted as a charge order-disorder phenomenon on Fe_{oct} sites. Charge localization at low temperature weakens the hopping mechanism of extra electrons on these sites, which is the main mechanism responsible for the conduction in magnetite.

The phase transition is very sensitive to the off-stoichiometry parameter δ and impurity cations on the Fe_{oct} sites. It changes its character from first order to second order and lowers its critical temperature down to 81 K for very small variations from the ideal stoichiometry in the range of $\delta_c = 0.0117$ [59, 61, 62]. Also, residual stress lowers the transition temperature and the magnitude of the discontinuous jump of the conductivity [63]. In thin films the transition is additionally affected by inhomogeneities and APBs [64] in a similar way.

Despite intensive investigations in the past 70 years several questions on the origin of the Verwey transition, such as the existence or exact appearance of charge order or the driving force for the transition, have not been fully resolved. One of the more recent suggestions about the charge order in the monoclinic, insulating, low-temperature state came from Jeng *et al.* [54]. They illustrated by means of LSDA calculations that an

ordering of the conduction electrons into certain Fe^{2+}_{oct}-t_{2g} orbitals, i.e., orbital ordering, drives the charge ordering. Due to screening effects the difference of the resultant charges is only 0.15 e and as such it is much smaller than the one electron expected in a purely ionic picture. A schematic energy level diagram of the involved minority-spin Fe^{2+}_{oct} orbitals is given in Fig. 2.4. Due to a displacement of the $Fe^{3+}(3)$ ion towards the lobes of the occupied t_{2g} orbitals of the $Fe^{2+}(1a,1b,4)$ the latters' energy is lowered, and the energies of empty $Fe^{3+}(3)$ orbitals are raised. Thus, there occurs an ordering of conduction electrons in the t_{2g} orbitals of the Fe^{2+}_{oct} below T_V. The aforesaid displacement of the $Fe^{3+}(3)$ ion explains the most significant structural change of the structural phase transition.

Lorenzo *et al.* [65] have shown by resonant x-ray diffraction that the charge and orbital orders develop concomitantly with the spin-orientation transition, i.e., the change of the easy axis, at the isotropic point T_K. The isotropic point is identified by vanishing magnetic anisotropy constants. T_K and T_V are distinct temperatures which, however, both are related to the Verwey transition. Lorenzo *et al.* concluded that all electronic degrees of freedom are coupled and participate at this phase transition. Since the lattice distortions and orbital fluctuations share the same symmetry, the Verwey transition can be viewed as a Jahn-Teller transition.

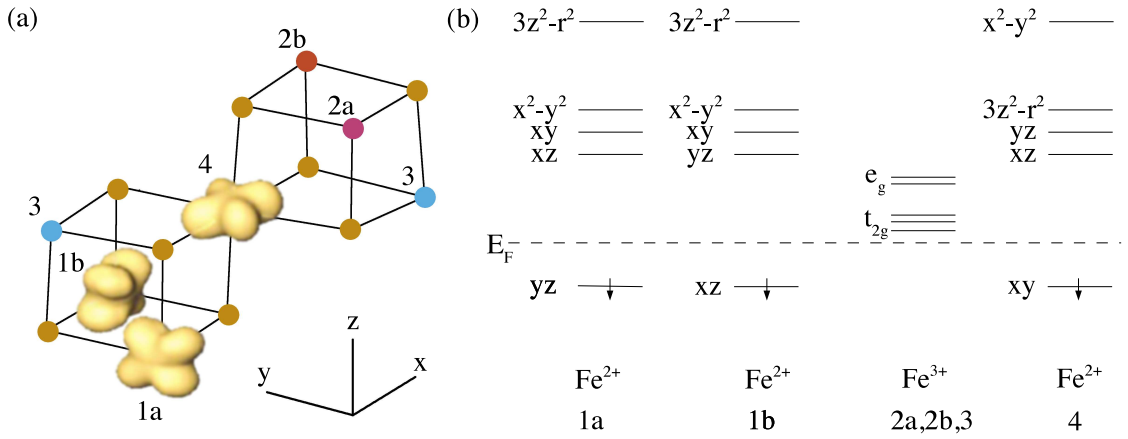

Figure 2.4: *Orbital ordering on the Fe_{oct} sublattice of the low-temperature structure of magnetite as proposed by Jeng et al. The local coordinates are as follows: the z axis is along the c crystal axis, x and y axes point towards the neighboring O atoms in the ab crystal plane. 1a, 1b, 2a, 2b, 3, and 4 refer to inequivalent Fe_{oct} sites in the monoclinic structure. (a) Orientation of occupied orbitals. (b) Schematic orbital energy diagram for the minority Fe_{oct} states. Adopted from Ref. [54].*

One shortcoming of the charge-order model (also called structural-electronic model) for the Verwey transition is that it cannot explain the anomaly in the magnetization curve, $M(T)$, and other magnetic properties such as the magnetoresistance and the magneto-caloric effect. Belov proposed a magneto-electronic model which explains both the low mobility of the conduction electrons and the anomaly in the magnetization

curve [66, 67]. According to his theory, the conduction electrons become localized due to the Vonsovskii exchange interaction which acts between valence and core electrons of all ferromagnetic materials. The spin of the conduction electrons interacts with the field of the magnetic moments of the inner electrons. In the case of magnetite the interaction is antiferromagnetic, and the conduction electrons correspond to the hopping minority electrons on the Fe_{oct} sites and the core electrons to the remaining, strongly localized *d*-electrons with their large magnetic moment. Due to this interaction the conduction electrons order magnetically as a so-called 'electron sublattice' below T_V. Since the magnetic moment of this electron sublattice is antiparallel to the majority Fe_{oct} sublattice, the net magnetic moment becomes partially screened below the phase transition (see Fig. 2.5). The extent of this screening and hence the magnetization jump at the phase transition, $\Delta M(T)$, is strongly influenced by the external magnetic field. It is largest for fields approximately equal to the technical saturation field, i.e., the field required to make an multi-domain grain single domain, around 0.1 to 0.3 T, and is essentially suppressed for high fields.

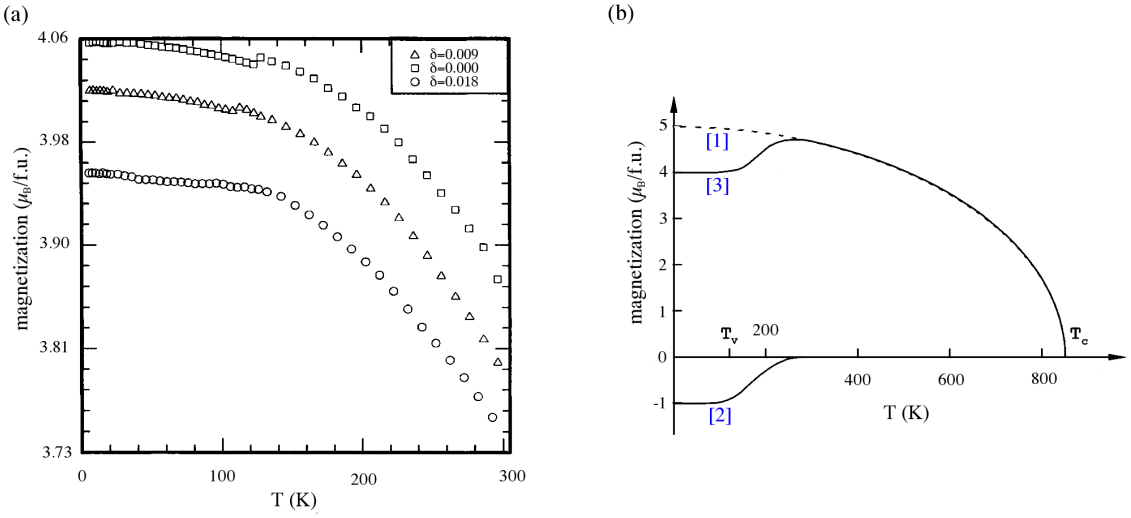

Figure 2.5: *(a) Magnetization measurements of $Fe_{3-\delta}O_4$ single crystals in a field of $\mu_B H = 1$ T reported by Aragón. The anomaly at the Verwey transition is very small in such a high field. Adopted from [59]. (b) Schematic representation of the anomaly of the magnetization at the Verwey transition in the magneto-electronic model. Curve 1: total net magnetization of Fe sublattices, curve 2: magnetization of the electron sublattice, curve 3: sum of curve 1 and 2. Adopted from Ref. [67].*

The dependence of the net magnetization on the external field is also termed 'para-process' and is responsible for the slow saturation behavior of single crystals in the low-temperature phase. With increasing external magnetic field the electron sublattice spins are more and more aligned along the net magnetization direction and hence the magnetization jump at the transition, $\Delta M(T)$, decreases. For a sufficiently large field

the electron sublattice is completely destroyed and the electrons become delocalized. This also explains why the negative magnetoresistance increases strongly on lowering the temperature from 300 to 130 K [66].

The Vonsovskii exchange interaction is also responsible for the low mobility of the conduction electrons above T_V. It induces spin flips during the hopping process, which then requires an additional activation energy and thus reduces the electron mobility [67]. Finally, within the magneto-electronic model, the concurrent structural phase transition is conjectured to be due to the onset of an anisotropic spontaneous magnetostriction.

3 Methods

3.1 Molecular beam epitaxy

> "Molecular beam epitaxy (MBE) is a vacuum deposition method in which well-defined thermal beams of atoms or molecules react at a crystalline surface to produce an epitaxial film. Epitaxial growth, a clean ultrahigh vacuum (UHV) deposition environment, *in situ* characterization during growth, and the notable absence of highly energetic species are characteristics that distinguish MBE from other thin film methods used to prepare functional oxide thin films." (Schlom *et al.*) [68]

3.1.1 Principle and beam fluxes

Figure 3.1 displays a sketch of an experimental setup for MBE. The monocrystalline substrate is located on a sample stage which allows for heating with infrared light or an electron beam. The sample surface can be cleaned by sputtering, i.e., bombardment with energetic ions (Ar^+, $E_{kin} = 1\,\mathrm{keV}$). A molecular beam of O_2 and an atomic beam of Fe impinge on the sample surface to form a thin film of iron oxide. Growth mode and surface structure can be monitored by reflection high-energy electron diffraction (RHEED).

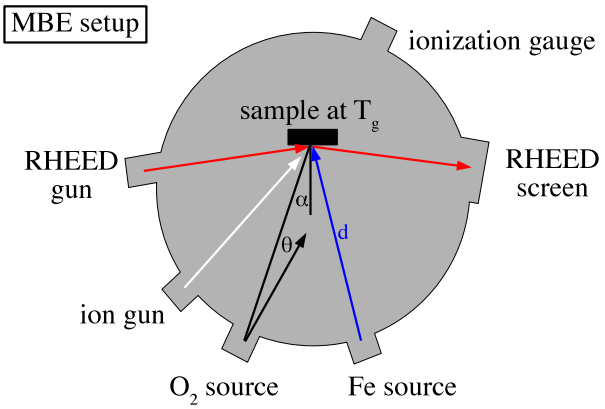

Figure 3.1: *Sketch of an experimental setup for MBE. Different beams are directed onto a sample in a UHV environment.*

In the following the fluxes of the molecular and the atomic beam of the experimental setup in Würzburg shall be estimated. Ultrahigh purity (99.9999%) molecular oxygen is delivered from a high-precision needle valve, passes through a small aperture, and a beam impinges onto the sample surface. Its flux is controlled by measuring the chamber pressure with an ionization gauge at a position which is not directly in the molecular beam, i.e., the measured pressure is not the 'beam equivalent pressure'. The flux of oxygen molecules delivered from the gas can be calculated by the Hertz-Knudsen-equation (cf. Ref. [69]):

$$F_{O_2} = \frac{p}{(2\pi m k_B T)^{1/2}} = 2.69 \cdot 10^{24} \cdot p \ \left[\frac{1}{\mathrm{m^2 s}}\right] \text{with } p \text{ in mbar}, \tag{3.1}$$

with a molecular mass of $m = 32\,\mathrm{u}$ and $T = 300\,\mathrm{K}$. So, the flux is proportional to the pressure p. However, the flux of the molecular beam decreases with d, which is the distance between source and sample, with θ, which is the angle between middle axis of the beam and the line connecting source and sample, and with α, which is the angle between sample normal and beam (see Fig. 3.1), according to

$$F \propto \frac{\cos^4 \theta}{d^2} \cos \alpha. \tag{3.2}$$

Thus, an additional geometric factor, g, taking into account the flux enhancement due to the different position of the ionization gauge compared to the actual sample position, and the atomic sensitivity of the ionization gauge for molecular oxygen, s, has to be added to Eq. (3.1), resulting in

$$F_{O_2} = \frac{g}{s} \cdot 2.69 \cdot 10^{24} \cdot p = \frac{4.22}{1.01} \cdot 2.69 \cdot 10^{24} \cdot p = 1.12 \cdot 10^{25} \cdot p \ \left[\frac{1}{\mathrm{m^2 s}}\right] \text{with } p \text{ in mbar}. \tag{3.3}$$

The flux of the used Fe evaporator cannot directly be determined from Eq. (3.1) since both the temperature of the evaporating rod and the beam equivalent pressure cannot be measured in the used setup. Alternatively, the Fe impingement rate, r (in Å/min·nA), was measured with a quartz-crystal monitor for a constant Fe ion current of the evaporator, I_{Fe}. With the monolayer density of bcc Fe, ρ_{ML}, one arrives at the following relation for the Fe flux

$$F_{Fe} = r g \rho_{ML} = 0.051 \cdot 0.50 \cdot \frac{2}{(2.87 \cdot 10^{-10})^2} \cdot I_{Fe} = 1.03 \cdot 10^{16} \cdot I_{Fe} \ \left[\frac{1}{\mathrm{m^2 s}}\right] \text{with } I_{Fe} \text{ in nA}. \tag{3.4}$$

Now, calculating F_{Fe} with a typical value of $I_{\mathrm{Fe}} = 40\,\mathrm{nA}$, the temperature, and vapor pressure of the rod tip can be estimated from tabulated data[1] to be 1260 K and $4 \cdot 10^{-7}$ mbar, respectively.

For a comparison of different growth conditions the ratio of both fluxes is an important parameter:

$$F_{\mathrm{Fe}}/F_{\mathrm{O_2}} = 9.2 \cdot 10^{-10} \frac{I_{\mathrm{Fe}}}{p} \quad \text{with } p \text{ in mbar and } I_{\mathrm{Fe}} \text{ in nA.} \tag{3.5}$$

When inserting typically used parameters $I_{\mathrm{Fe}} = 40\,\mathrm{nA}$ and $p(\mathrm{O_2}) = 4 \cdot 10^{-6}\,\mathrm{mbar}$, one observes that $F_{\mathrm{Fe}}/F_{\mathrm{O_2}}$ is about 0.01. Next, the dissociation efficiency of $\mathrm{O_2}$ molecules at the surface has to be considered. A rough estimate of the fraction of dissociated oxygen is 14 % regarding the cracking pattern of $\mathrm{O_2}$ in UHV [70]. Then, $F_{\mathrm{Fe}}/F_{\mathrm{O_2}}$ rises to about 0.066.

It has to be noted at this point that the amount of deposited material or the actual growth rate is not only determined by the impingement fluxes, but also by the substrate temperature owing to the strong temperature dependence of the sticking coefficients and other atomistic processes relevant for growth (cf. Sec. 3.1.2).

3.1.2 Atomistic processes on surfaces and epitaxy of magnetite

The formation of a thin film is a result of two steps, viz. nucleation and growth of the nuclei. Thereby occurring atomistic processes (see Fig. 3.2) can be described by the theoretical concept of growth kinetics. Processes such as adsorption, surface diffusion, and chemical binding shall be visualized here only shortly since atomistic parameters were not extracted during experiments. In many cases kinetic factors rather than thermodynamic arguments determine the morphology of a thin film.

Atoms or molecules from an evaporation source or the background gas in the chamber arrive on the surface with a certain flux F ($\mathrm{cm^{-2}s^{-1}}$) (see Sec. 3.1.1). The adsorbed single atoms diffuse on the surface until they undergo one of the following processes: re-evaporation, nucleation of a cluster, binding to an existing cluster, interdiffusion into the substrate, or capture at special defect sites such as vacancies, steps, ledges, kinks, or dislocations. Process rates and consequentially atom concentrations in a certain stage depend on this flux F and, most importantly, on the substrate temperature T_g, because all of the above processes are thermally activated. A defined activation energy is associated with each of these processes (see E_a, E_d, and E_j in Fig. 3.2). The defect sites of a real surface are often of great importance as they influence adsorption, diffusion, and binding and can effectively lower the energetic barrier for the formation of nuclei of critical size.

Growth of iron oxide proceeds via a 'reactive MBE' process, which means that impinging $\mathrm{O_2}$ molecules chemisorb on the growing surface, dissociate, and react with available

[1] Vapor pressure data for selected elements, Veeco company, 2009

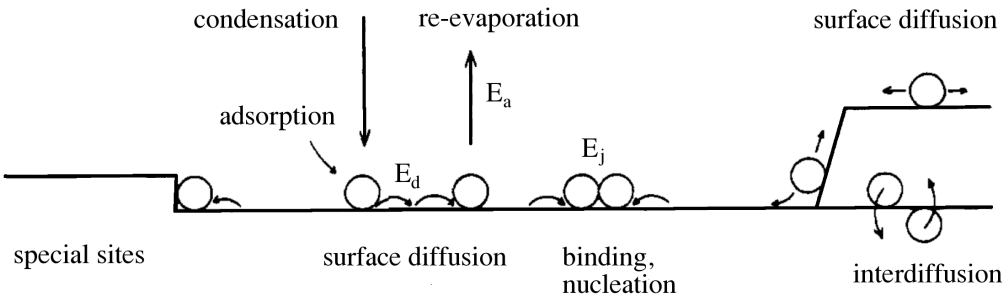

Figure 3.2: *Atomistic processes on surfaces which are relevant for the nucleation and growth of a thin film. Adopted from Ref. [71].*

Fe atoms. The oxidation state of the iron oxide is a function of the Fe/O_2 flux ratio, the growth temperature, and the used substrate. A lower substrate temperature, T_g, effectively increases the amount of chemisorbed O_2 more strongly than the amount of Fe [72]. Critical nuclei during Fe_3O_4 growth are pairs of iron and oxygen, and iron is more mobile than oxygen [73].

The substrate has a strong influence on the film composition, which is an effect called composition-pulling. Under the same experimental conditions monocrystalline Fe_3O_4 is stabilized on lattice-matching MgO whereas on Al_2O_3 the film consists of different phases such as Fe or FeO inclusions [74]. Films with a thickness larger than 10 nm were found to be 'rather stable' against oxidation in air [72], which is a very important point when experiments are performed *ex situ*.

3.1.3 Growth modes

The growth of epitaxial thin films generally proceeds in one of the following three modes according to the observed film morphology (see Fig. 3.3). In layer-by-layer or Frank-van der Merwe mode the interatomic interaction between film and substrate atoms is more strongly attractive than the interactions between film atoms forcing the deposit material to form closed layers on the substrate (see Fig. 3.3(a)). Given that the binding strength between layers decreases monotonically with the number of layers and approaches the bulk value of the film material in the limit of a thick film, they will be deposited in a layer-by-layer fashion. Here, the surface energy term of the substrate, δ_{sub}, is the dominating term in the energy balance. For island or Volmer-Weber mode the opposite is true: the surface energy of the film, δ_{film}, and the interface energy between film and substrate, σ, are larger than δ_{sub}. Therefore, it is energetically more favorable for the atoms to nucleate on the top of existing islands than on uncovered areas of the substrate (see Fig. 3.3(c)). Finally, in the case of layer plus island or Stranski-Krastanov mode a transition from the layer to island mode takes place at a certain coverage, since the energy balance changes with film thickness (see Fig. 3.3(b)).

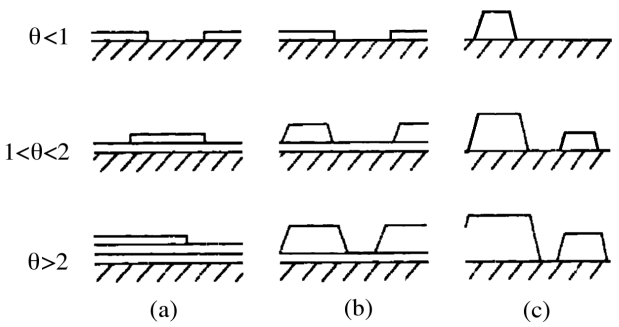

Figure 3.3: *Growth modes in thin film epitaxy for three ranges of the monolayer coverage θ. (a) Layer-by-layer or Frank-van der Merwe mode. (b) Layer plus island or Stranski-Krastanov mode. (c) Island or Volmer-Weber mode. Taken from Ref. [71].*

3.1.4 Thermodynamics of epitaxy

At the beginning of this section about thermodynamics of growth it has to be clarified that a thin film structure can be either thermodynamically stable, i.e., in thermodynamic equilibrium, or metastable, i.e., kinetically stabilized. Kinetic stabilization of a thin film structure occurs if kinetic barriers hinder the transition to the stable equilibrium state, which is determined by thermodynamics. Three growth regimes, classified according to their growth temperature T_g, are relevant in this respect: If T_g is low enough to hinder sufficient surface diffusion, growth results will generally be amorphous or polycrystalline. If the surface diffusion is fair but bulk diffusion is low, the growth result will be oriented and well crystallized, but phase transformation and interdiffusion across the interface will be limited. And of course, if T_g is large and the bulk and surface diffusion rates are high, the thermodynamically most stable, possibly mixed phase will form.

The concept of 'thermodynamic epitaxial stabilization' describes the fact that a thin film can lower its energy by adopting a crystal structure different from its equilibrium bulk one. The associated energy gain is related to the considerably lower energy of a coherent interface compared to an incoherent or semicoherent one (see Fig. 3.4 and Tab. 3.1). Epitaxial or pseudomorphic growth is on hand if the lattice is commensurate across the interface.

Table 3.1: *Ranges of solid-solid interface energies σ^{ss} for three types of planar interfaces. Taken from Ref. [76].*

interface	interface energy σ^{ss} (mJ/m^2)
coherent	5-200
semicoherent	200-800
incoherent	800-2500

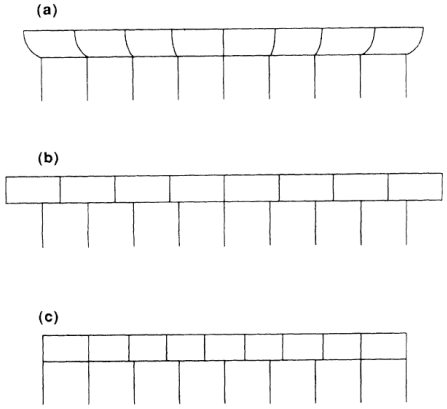

Figure 3.4: *Schematic structure of a single domain film. (a) Strained commensurate film with coherent interface. (b) Unstrained incommensurate film with incoherent interface. (c) Strained incommensurate film with misfit dislocations and semicoherent interface. Taken from Ref. [75].*

Let us consider a model taken from Ref. [77] to see how an epitaxially growing phase E is stabilized opposite to an incoherent phase B possessing the bulk crystal structure. The Gibbs energy of the growing nucleus of the film material can be divided into four energy terms,

$$G = \gamma \cdot V + \sigma \cdot S + \delta \cdot A + G^{stress}, \tag{3.6}$$

namely, the volume energy depending on the volume of the nucleus V and the specific Gibbs energy of the material γ, the interface energy term depending on the specific interface energy σ and the interface area S, the surface area term with the specific surface energy δ and the surface area A, and the stress energy term. The volume term will always be negative, the other three positive. The nucleus shall be modeled as cuboid with side d and height h, which sits on a flat substrate. Film and substrate both shall exhibit a square lattice at the interface with lattice constants a_f and a_s, respectively, and shall have equal density. Therefore, the lattice mismatch is given by $\epsilon = (a_f - a_s)/a_s$. We can write for the coherent phase E assuming homogeneous strain

$$G_E = \gamma_E d^2 h + \sigma_E^c d^2 + \delta_E(d^2 + 4dh) + h\frac{\mu}{1-\nu}\epsilon^2 d^2, \tag{3.7}$$

and for the incoherent phase B

$$G_B = \gamma_B d^2 h + \sigma_B^{ic} d^2 + \delta_B(d^2 + 4dh), \tag{3.8}$$

where σ^c and σ^{ic} denote specific interface energies with the substrate of the coherent and incoherent phase, and μ and ν are shear modulus and Poisson's ratio for the coherent phase, respectively. The phase B does not exhibit the strain contribution, but it has a distinctly higher specific interface energy than phase E. Since phase B possesses the

equilibrium crystal structure, γ_B is more negative than γ_E. For simplicity, we furthermore assume equal interface energies with the vapor phase $\sigma_v^B = \sigma_v^E$, thereby ignoring the contribution of edges and surfaces of film islands. Also, the case of a semicoherent phase is ignored for the moment.

The energy difference between the two phases per thin film area $\Delta g_{E-B} = (G_E - G_B)/d^2$ then is

$$\Delta g_{E-B} = h\left[(\gamma_E - \gamma_B) + \frac{\mu}{1-\nu}\epsilon^2\right] + \sigma_E^c - \sigma_B^{ic}. \tag{3.9}$$

This equation describes the epitaxial stabilization as function of the thickness h. The first term is positive and increases linearly with h, the remaining terms add up to a negative constant. Above a certain critical thickness, h_c, the first term overcompensates the negative constant, Δg_{E-B} becomes positive and the incoherent phase is energetically favorable. The value of h_c depends linearly on the volume and interface energy differences, but its dependence on ϵ is quadratic. A typical value of h_c is of the order of a few nanometers and much larger values are only possible for a very small ϵ.

We now release the restriction of homogeneous strain and allow strain relaxation through misfit dislocations. This introduces a term for inhomogeneous strain and also changes the magnitude of the homogeneous strain. We set the Burgers vector of the edge dislocations to a_f and obtain for the energy difference

$$\begin{aligned}\Delta g_{E-B} = h\left[(\gamma_E - \gamma_B) + \frac{\mu}{1-\nu}\left(\epsilon - \frac{a_f}{l}\right)^2\right] + (\sigma_E^c - \sigma_B^{ic}) \\ + \frac{1}{l}\left[E_{core} + \frac{\mu}{1-\nu}K a_f^2 \exp\left(-\frac{4\pi h}{l}\right)\right],\end{aligned} \tag{3.10}$$

where l is the distance between neighboring misfit dislocations, E_{core} their core energy, and K a numerical factor. For a complete relaxation $l = a_f/\epsilon$ and the term describing the homogeneous strain vanishes. If additionally $h \gg l$, the exponential term disappears as well, and the last term can be added to σ_E^c resulting in the energy of the semicoherent interface σ_E^{sc}, and Eq. (3.10) simplifies to

$$\Delta g_{E-B} = h(\gamma_E - \gamma_B) + (\sigma_E^{sc} - \sigma_B^{ic}). \tag{3.11}$$

This is similar to Eq. (3.9), though the difference of the interface energies has decreased and the strain energy term has vanished. Again, an epitaxial layer can be thermodynamically stabilized below a critical thickness, demonstrating that lattice strain is not a necessary condition for this stabilization mechanism.

In an intermediate range of film thicknesses a third mechanism, viz. the formation of periodic domain structures, can be the energetically most favorable. Here, the energy gain due to a decrease of homogeneous strain in the film is larger than the energy increase by the formation of domain walls and the relatively small inhomogeneous strain in the substrate. Thereby, domains can be commensurate or incommensurate [75]. In case of

a complete relaxation through this mechanism, the energy balance can be written

$$\Delta g_{E-B} = h(\gamma_E - \gamma_B) + K\epsilon^2\sqrt{h} + (\sigma_E^c - \sigma_B^{ic}), \tag{3.12}$$

showing that the term associated with the multiple-domain microstructure increases only with $\sqrt{h}$ and therefore induces a total energy minimum for intermediate thicknesses.

In the last considered case the occurrence of randomly oriented crystallites in the incoherent phase, i.e., polycrystalline films, is allowed, although this is not the equilibrium state, but a metastable state. This introduces terms for the incoherent grain boundary energy between crystallites and/or the surface energy for separated islands. We model the grains as cuboids with a mean grain size r, and therefore obtain the number of grains $N = d^2/r^2$ with $r \ll d$ and the mean grain boundary energy

$$E_{gb} = 2hrN\sigma_B^{gb} = \frac{2h\sigma_B^{gb}}{r} \text{ for compact polycrystalline growth,} \tag{3.13a}$$

$$E_{gb} = \frac{4h\delta_B}{r} \text{ for island-like polycrystalline growth,} \tag{3.13b}$$

and the complete energy balance

$$\Delta g_{E-B} = h(\gamma_E - \gamma_B) - E_{gb} + (\sigma_E^c - \sigma_B^{ic}). \tag{3.14}$$

If on the other hand the coherent phase grows in island-like mode, a term $E_{gb} = \frac{4h\delta_E}{r}$ has to be added to Eq. (3.14). Since the grain boundary term of the incoherent phase in Eq. (3.14) increases rapidly with increasing film thickness h, large values for the critical thickness of the coherent phase can be obtained in the case of a very small grain size r. A crucial parameter is also the dependence of the grain size on film thickness, $r(h)$. In MBE the kinetic contribution due to polycrystalline growth, E_{gb}, usually will not be zero, and, as a result, the experimentally determined critical thickness will exceed the theoretical value.

It has been reported that magnetite thin films can be grown fully coherent with the substrate MgO up to a thickness of 600 nm by magnetron sputtering [78] and up to 700 nm by MBE [17]. This anomalous strain relaxation behavior is due to anti-phase boundaries (APB) (cf. Sec. 2.2), which provide a strain accommodation mechanism compensating the tensile strain due to the lattice mismatch. Stress accommodation in the film depend on the nature and density of these APBs.

Furthermore, strain relaxation cannot only be accomplished by misfit dislocations or polycrystalline growth but also by surface roughening, the formation of an reactive interface (see Sec. 3.1.5), or a combination of these mechanisms. Since the creation of misfit dislocations is connected with an energy barrier with values usually much larger than the thermal energy provided at the growth temperature, misfit dislocations actually have to be annealed into the crystal [17, 69, 79].

Table 3.2: *Lattice mismatch, ϵ, and critical thickness of structural relaxation, h_c, for epitaxy of Fe_3O_4 on different substrates. The critical thickness was calculated with the theoretical model of Fischer, Kühne, and Richter [80].*

substrate	MgO(001)	FeO(001)	GaAs(001)	InAs(001)	ZnO(001)
lattice mismatch ϵ (%)	−0.32	−2.3	5.02	−1.63	−8.64
critical thickness h_c (Å)	983	105	41	156	21

Table 3.2 lists epitaxial mismatch and critical thickness for strain relaxation via misfit dislocations in the case of epitaxy of Fe_3O_4 on different substrates. The critical thickness was calculated with the theoretical model of Fischer, Kühne, and Richter which takes into account the elastic interaction between straight misfit dislocations [80].

3.1.5 Thermodynamic stability of magnetite in contact with semiconductors

In Sec. 3.1.4 the interface between film and substrate was assumed to be ideal from the compositional point of view: the distribution of atoms of a certain species changes abruptly when crossing the interface. This situation can be termed 'sharp' interface. It will occur if intermixing of the film and substrate atoms is energetically unfavorable. The other case of a non-abrupt interface can exist in two variations. If one material is soluble in the other but not vice versa there will be an interdiffusion region where composition varies. Impurities in this interdiffusion region will be either substitutional or interstitial. However, if both materials are solvable into each other they will form a mixed compound at the interface. This corresponds to a reactive interface where actually two interfaces are formed: one between substrate and compound and the other between compound and film. Of course, the question which interface and to which amount each interface is realized depends strongly on the growth temperature. Temperature also decides if this interface is thermodynamically or rather kinetically stable.

An ideal substrate for epitaxy should be chemically stable in contact with the film material. The direct growth of oxides on semiconductors is often complicated by chemical reactions at the interface or substantial interdiffusion across the interface. In certain cases, an appropriate buffer layer exists which helps to reduce or hinder the interfacial reaction (e.g., a silicide layer on Si [81, 82]). However, generally interface reactions can be expected to hinder epitaxial growth or to influence film or substrate properties in an undesirable manner.

Thermodynamic instability of a specific film/substrate system is a necessary but insufficient criterion to conclude that chemical reactions at an interface will take place. Beyond that, kinetic barriers can exist limiting interdiffusion or chemical reaction. In the following the thermodynamic stability of Fe_3O_4 in contact with GaAs, InAs, and ZnO is tested following the method in Refs. [83, 84]. This is accomplished by cal-

culating the change of the Gibbs energy using tabulated thermodynamic data taken from Ref. [85]. A negative/positive change of Gibbs energy indicates if the respective reaction takes place spontaneously/non-spontaneously and if the interface is thermodynamically unstable/stable. The testing is restricted to solid state reactions and to typical growth temperatures ranging from 300 K to 1000 K in steps of 100 K for which sufficient thermodynamic data are available. The balanced reactions between the oxide and semiconducting substrate are analyzed in Tabs. 3.3 and 3.4.

Fe_3O_4/GaAs

Since thermodynamic data for the phases FeGa and FeAs are not available, reactions involving these phases are ignored. Moreover, the reactions from Fe_3O_4 to Fe_2O_3 are not included since they do not accompany an oxidation of GaAs.

Table 3.3: *Several possible balanced interfacial reactions of Fe_3O_4 with GaAs and respective sign of the change of Gibbs energy, ΔG.*

no.	educts	$\rightarrow$	products	ΔG
	reactions to Fe and binary oxides:			
(1)	8 GaAs + 3 Fe_3O_4	$\rightarrow$	4 Ga_2O_3 + 8 As + 9 Fe;	< 0
(2)	8 GaAs + 3 Fe_3O_4	$\rightarrow$	8 Ga + 4 As_2O_3 + 9 Fe;	> 0
(3)	8 GaAs + 5 Fe_3O_4	$\rightarrow$	8 Ga + 4 As_2O_5 + 15 Fe;	> 0
	reactions to FeO and binary oxides:			
(4)	2 GaAs + 3 Fe_3O_4	$\rightarrow$	1 Ga_2O_3 + 2 As + 9 FeO;	< 0
(5)	2 GaAs + 3 Fe_3O_4	$\rightarrow$	2 Ga + 1 As_2O_3 + 9 FeO;	> 0
(6)	2 GaAs + 5 Fe_3O_4	$\rightarrow$	2 Ga + 1 As_2O_5 + 15 FeO;	> 0
	reactions to $GaAsO_4$:			
(7)	1 GaAs + 1 Fe_3O_4	$\rightarrow$	1 $GaAsO_4$ + 3 Fe;	> 0
(8)	1 GaAs + 4 Fe_3O_4	$\rightarrow$	1 $GaAsO_4$ + 12 FeO;	> 0
	reactions to $FeAsO_4$:			
(9)	1 GaAs + 1 Fe_3O_4	$\rightarrow$	1 Ga + 1 $FeAsO_4$ + 2 Fe;	> 0
(10)	1 GaAs + 3 Fe_3O_4	$\rightarrow$	1 Ga + 1 $FeAsO_4$ + 8 FeO;	> 0
	reactions to $Fe_3As_2O_8$:			
(11)	2 GaAs + 2 Fe_3O_4	$\rightarrow$	2 Ga + 1 $Fe_3As_2O_8$ + 3 Fe;	> 0
(12)	2 GaAs + 5 Fe_3O_4	$\rightarrow$	2 Ga + 1 $Fe_3As_2O_8$ + 12 FeO;	> 0

From Tab. 3.3 it can be extracted that the only spontaneous reactions are those including Ga_2O_3 as a product. Hence, the Fe_3O_4/GaAs interface is thermodynamically unstable, and the formation of Ga sesquioxide (Ga_2O_3) is expected, whereas an oxidation of As at the interface is not. Furthermore, the three tested ternary oxides do not occur in thermodynamic equilibrium. The latter two, $FeAsO_4$ and $Fe_3As_2O_8$, lie above the Fe_3O_4-As tie line in the ternary Fe-O-As phase diagram.

Fe_3O_4/InAs

The case of an InAs substrate can be treated analogously as GaAs by replacing Ga by In in all reaction equations of Tab. 3.3. Since thermodynamic data for ternary oxides of iron, indium and arsenic are not at hand, the remaining equations are skipped here. All of these reactions raise the Gibbs energy with the exception of reaction (4) where ΔG changes from positive values for temperatures of 700 K or lower to negative values for 800 K or higher. Thus, the Fe_3O_4/InAs interface is thermodynamically stable at temperatures lower or equal to 700 K.

Fe_3O_4/ZnO

The situation is quite different for the Fe_3O_4/ZnO interface. Here, thermodynamic data exist only for Fe_2ZnO_4 which is not a higher oxidation state of Zn, but a higher oxidation state of Fe. It is especially interesting to see whether this spinel phase is thermodynamically more stable. As an exception the occurrence of the gas phase O_2 as a product in reaction (2) in Tab. 3.4 is taken into account. Additionally, it is tested if an oxidation to Fe_2O_3 is energetically favorable.

Table 3.4: *Possible balanced interfacial reactions of Fe_3O_4 with ZnO and respective sign of the change of Gibbs energy, ΔG.*

no.	educts		products	ΔG
	reactions to $ZnFe_2O_4$:			
(1)	1 ZnO + 1 Fe_3O_4	$\rightarrow$	1 $ZnFe_2O_4$ + 1 FeO;	> 0
(2)	2 ZnO + 2 Fe_3O_4	$\rightarrow$	2 $ZnFe_2O_4$ + 2 Fe + 1 O_2;	> 0
(3)	1 ZnO + 2 Fe_3O_4	$\rightarrow$	1 Zn + 1 Fe_2O_3;	> 0

All these reactions exhibit a positive change of the Gibbs energy at all tested temperatures indicating that none of them takes place, and the interface is stable in thermodynamic equilibrium.

At this point, it should be stressed that the result of the present thermodynamic investigation decides if the initial layer of magnetite is stable on the corresponding semiconductor. However, during a real experiment the substrate is in contact with a molecular oxygen flux in the early growth stage at a given temperature. This will lead to some kind of substrate-oxygen bonding at the initial growth stage. However, the thickness of this relatively thin oxide overlayer will increase at later growth stages only if the oxide layer is sufficiently permeable for oxygen.

3.2 Photoelectron spectroscopy

Photoelectron spectroscopy (PES) has been used in this work as a main tool to characterize the oxidation state, chemistry, and cleanliness of grown thin films. Its main

advantages over other techniques is the large surface sensitivity (cf. Sec. 3.2.3), its ability to identify chemical environments of elements present in the sample, the possibility for depth profiling, and the quantification of element ratios, i.e., the access to a sample's stoichiometry (cf. Sec. 3.2.4).

3.2.1 Principle

The basic principle of PES is illustrated by the schematic picture in Fig. 3.5. A photon source produces monochromatic photons with energy $h\nu$ and a polarization described by the vector potential $\mathbf{A}$, which are directed onto the sample surface under the angle ψ with respect to the sample normal and excite photoelectrons. The latter leave the sample surface region under the emission angle θ and pass through electron lenses and an electrostatic analyzer to reach a detector system. The photoelectrons can be discriminated according to their kinetic energy E_{kin}, momentum $k_{||}(E_{kin}, \theta)$, and/or spin orientation σ. Energy conservation requires that the following relation for the kinetic energy of photoelectrons, E_{kin}, the binding energy of electrons in the solid, E_B, and the work function of the sample surface, ϕ_0, is valid:

$$E_{kin} = h\nu - E_b - \phi_0. \tag{3.15}$$

PES experiments are performed in UHV due to requirements of a clean sample surface and large mean free paths of photons and electrons.

Figure 3.6 exemplifies how the measured photoelectron spectrum is related to the electronic structure of the investigated material and how information about electronic core levels and valence-band states can be extracted from the spectrum. The PES methods are loosely classified according to the employed photon-energy source into extreme ultraviolet photoelectron spectroscopy (EUPS) with $h\nu = 20$ to 150 eV, x-ray photoelectron spectroscopy (XPS) with, e.g., $h\nu = 1486.6$ eV for Al-$K_{\alpha_{1,2}}$ radiation, and hard x-ray photoelectron spectroscopy (HAXPES) with $h\nu = 3$ to 10 keV at a suitable synchrotron light source. Photon energy linewidths differ from a few meV for discharge lamps, 300 meV for monochromatized Al-K_{α_1}, to up to more than 1 eV for non-monochromatized, characteristic x-ray lines (e.g. Al-$K_{\alpha_{1,2}}$ or Mg-$K_{\alpha_{1,2}}$).

3.2.2 Description of spectral features

A real photoelectron spectrum is not as simple as Eq. (3.15) might suggest since the photoelectron is removed from a solid with a large number of interacting electrons. A starting point for the theoretical description of a photoelectron spectrum is Fermi's golden rule, which treats the light field as a first order perturbation of the system and specifies the transition rate from the initial state $|\Psi_0(N)\rangle$ to the final state $|\Psi_k(N)\rangle$ of

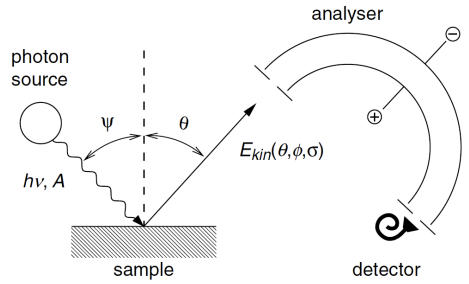

Figure 3.5: *Basic principle of PES. A photoelectron is excited by the light field ($h\nu$, $\mathbf{A}$) and is measured by an analyzer-detector combination with respect to its kinetic energy E_{kin}, momentum $k(E_{kin}, \theta, \phi)$, and spin orientation σ. Taken from Ref. [86].*

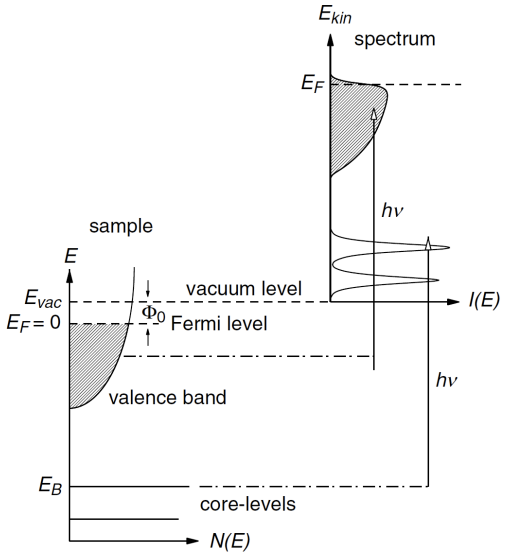

Figure 3.6: *Connection between PES spectrum and DOS of a solid. Taken from Ref. [86].*

the N-electron system (for a review see Refs. [86–88]):

$$\left|\langle\Psi_k(N)|\, H^1\, |\Psi_0(N)\rangle\right|^2 \cdot \delta(E_k(N) - E_0(N) - h\nu). \tag{3.16}$$

The final state consists of the photoelectron with momentum $\hbar k$ and energy $E_k = (\hbar k)^2/(2m)$ and the remaining $(N-1)$-electron system. Neglecting the term proportional to $|\mathbf{A}|^2$, which is relevant only for extremely high photon intensities, and the spin interaction $-\gamma \mathbf{S} \cdot \mathbf{B}$, the perturbation operator H^1 is given as:

$$H^1(t) \;=\; \frac{e}{2m}\left(\mathbf{A}\cdot\mathbf{P} + \mathbf{P}\cdot\mathbf{A}\right). \tag{3.17}$$

With the commutator relation $[\mathbf{P}, \mathbf{A}] = -i\hbar\nabla\cdot\mathbf{A}$ and the dipole approximation ($\mathbf{A}$ is constant over the atoms' dimensions and therefore $\mathbf{P}\cdot\mathbf{A} = -i\hbar\nabla\cdot\mathbf{A} = 0$), it follows:

$$H^1(t) \;=\; \frac{e}{m}\mathbf{A}\cdot\mathbf{P}. \tag{3.18}$$

The resulting photocurrent $I_k(h\nu)$ is a sum over all possible final states:

$$I_k(h\nu) \propto \sum_s \left|\langle\Psi_{k,s}(N)|\, H^1\, |\Psi_0(N)\rangle\right|^2 \cdot \delta(E_{k,s}(N) - E_0(N) - h\nu). \tag{3.19}$$

Here, the index s corresponds to a complete set of quantum numbers which contains all possible final state excitations. For a further analysis of the photocurrent a central simplification is assumed, the so-called 'sudden approximation'. This approximation is satisfied for high kinetic energies of the photoelectron. It is assumed that the photoelectron suddenly leaves the solid and that the reaction of the remaining $(N-1)$-electron system after the photoemission process can be neglected. As a result the photoelectron may be mathematically decoupled from the remaining system in the final state:

$$|\Psi_{k,s}(N)\rangle = c_k^\dagger \, |\Psi_s(N-1)\rangle \,, \tag{3.20}$$

where $c_k^\dagger$ is the creation operator for the photoelectron. Inserting this expression into Eq. (3.19), the photocurrent can be written:

$$I_k(h\nu) \propto \sum_j |M_{kj}|^2 \cdot A_j^<(E_k - h\nu). \tag{3.21}$$

The first factor $|M_{kj}|$ is the transition matrix element and the second factor corresponds to the one-electron spectral function:

$$A_j^<(h\nu) = \sum_s |\langle \Psi_s(N-1)| \, c_j \, |\Psi_0(N)\rangle|^2 \cdot \delta(h\nu - [E_s(N-1) - E_0(N)]). \tag{3.22}$$

Here, the δ-functions fixes the energy position at which a single transition appears in the spectrum. The other term is the sum of probabilities that the remaining $(N-1)$-electron system is left in the excited states s after the photoemission process. There will be a peak in the spectrum for each non-vanishing summand of the spectral function with a non-zero matrix element. For the easiest case of an uncorrelated electron system $c_j \, |\Psi_0(N)\rangle$ is an eigenstate of the $(N-1)$-particle system and the spectral function corresponds to a single δ-function. In the case of a core-level spectrum the energy position of the δ-function corresponds to the position of the main line. If the investigated system is, however, correlated, several of the summands in the spectral function are non-zero and the spectrum is a combination of the main line and additional satellite lines.

3.2.3 Surface sensitivity of electrons

One of the major advantages but also obstacles of PES is its inherent surface sensitivity. Since the photoelectrons interact strongly with the solid while traveling through it, their mean free path before experiencing an inelastic collision is only of the order of a few ångströms. As a result, this effects that the signal of electrons from deep layers is damped and the mean free path of the detected photoelectrons is limited to some nanometers. Tanuma, Powell, and Penn have studied the inelastic mean free path (IMFP) of electrons in various classes of materials in several publications and give the following so-called

'TPP-2M' predictive equation [89]:

$$\lambda = \frac{E}{E_p^2\{\beta \ln(\gamma E) - (C/E) + (D/E^2)\}} \quad [\text{Å}]\,, \tag{3.23}$$

where E is the kinetic energy of the electron. The plasmon energy, E_p, and the other parameters β, γ, C, and D are directly related to the material parameters density, atomic or molecular weight, number of valence electrons per atom or molecule, and band-gap energy.

Figure 3.7 shows the dependence of the IMFP on the electron kinetic energy in materials relevant for this work. Some typical values for the kinetic energy and the respective IMFPs are marked therein. It is clear from Fig. 3.7 that the IMFP is material-dependent and especially that the values in elemental Fe and GaAs differ by some percent from the ones in the listed oxides. On the other hand, the difference of the IMFP within the group of oxides is small, i.e., at most a few percent. To guarantee consistency within all quantified PES results, the IMFP of magnetite is employed in this work for all calculations as a compromise.

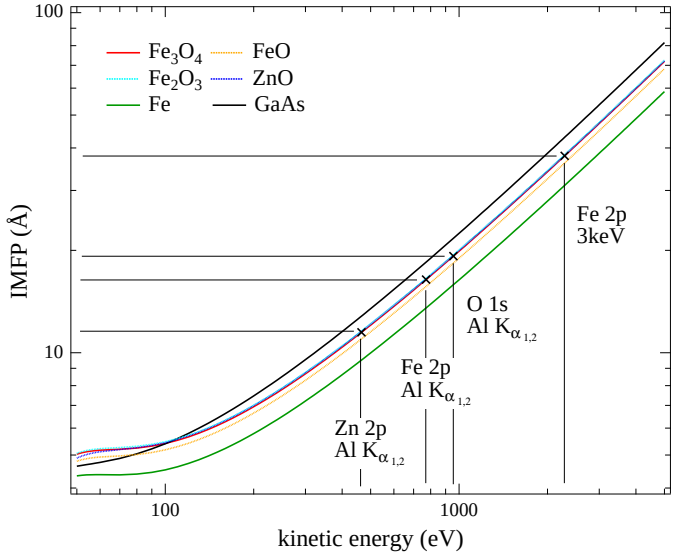

Figure 3.7: *Comparison of the IMFP of electrons in different materials calculated with Eq. (3.23) from Tanuma et al. [89].*

In the experiment one is interested in the variation of a sample's stoichiometry along its depth, a so-called depth profile. For that purpose, one evaluates the stoichiometry (see Sec. 3.2.4) for several mean escape depths of the electron, i.e., IMFPs projected along the sample normal:

$$\lambda_{eff} = \lambda(E)\cos\theta. \tag{3.24}$$

One sees that there are two possibilities to increase the electron mean escape depth: either increase of the electron kinetic energy or decrease of the electron emission angle θ. The term $3\lambda_{eff}$ is also called information depth since about 95 % of the signal originate from a layer with this thickness.

3.2.4 Electron spectroscopy for chemical analysis

Electron spectroscopy for chemical analysis (ESCA) is often used as a synonym for XPS since it indicates its ample use to identify a sample's stoichiometry. The basis for quantification of XPS is that the photoelectron intensity, i.e., the area of the background-subtracted photoelectron line, of an element's core level is a measure for the element's concentration within the analyzed sample volume. Assuming a homogeneous probed sample volume the photoelectron intensity, I, of a core level at kinetic energy, E_{kin}, can be expressed in the following formula:

$$I = NF_{h\nu}\sigma\lambda(E)T(E)\cos\theta. \tag{3.25}$$

Here, N is the atomic concentration of the element, F_{hv} the photon flux, σ the photoelectron cross section, $\lambda(E)$ the IMFP of the photoelectron (cf. Eq. (3.24)), $T(E)$ the transmission function of the analyzer, and θ the electron emission angle. The photoelectron cross sections can be extracted from the tabulated data from Yeh and Lindau [90] or Trzhaskovskaya *et al.* [91]. In these reports the atomic subshell photoionization cross sections and asymmetry parameters were calculated for a set of elements assuming free atoms. Furthermore, the transmission function of the employed analyzer EA125 from Omicron Nanotechnology was determined by Ruffieux *et al.* [92] and can be written as:

$$T(E) = E^x, \tag{3.26}$$

where the exponent x is approximately -1. Since the photon flux is not known, it is not possible to determine absolute but only relative atomic concentrations of elements A and B using the following relation:

$$R_{A/B} = \frac{N_A}{N_B} = \frac{I_A S_B}{I_B S_A} = \frac{I_A \sigma_B \lambda(E_B) T(E_B)}{I_B \sigma_A \lambda(E_A) T(E_A)}. \tag{3.27}$$

The sensitivity factor, S_A, differs for each core level of the respective element A. Note that the dependence on θ and $F_{h\nu}$ is canceled out if the measurement is performed under identical conditions, and that the errors of IMFP and analyzer transmission function are minimized if photoelectrons of similar kinetic energy are compared. This means that the largest error in $R_{A/B}$ stems from the error of the cross section, $\Delta\sigma$. Since the calculation of the cross section does not take into account the bonding properties in the solid, its error usually will be large and is estimated to be up to 20 %. From the determination of several ratios of elements, R, the chemical composition of a sample can be simply

derived. Because of the large error of the photoionization cross section and the relatively small information depth of the method, absolute values of chemical composition often deviate from expected numbers. For this reason, only the relative change, i.e., the alteration of chemical composition between different preparation steps or information depths, respectively, should be compared. Another method to determine precisely the ratio of Fe and O atomic concentrations from the comparison of experimental spectra with spectra from reference compounds is described in Sec. 3.2.5.

Determination of overlayer thickness

In addition to the stoichiometry analysis, XPS offers the possibility for an *in situ* determination of the film thickness of thin film samples. In doing so the basic assumption is that the corrected photoelectron intensity of a substrate element, N_{sub}, is exponentially attenuated by an epitaxially grown film of thickness t_{film} when compared to the one of a film element, N_{film}:

$$R_{film/sub} = \frac{N_{film}}{N_{sub}} = \frac{I_{film} S_{sub}}{I_{sub} S_{film}} \approx \frac{D_{film} \lambda_{film}}{D_{sub} \lambda_{sub}} \frac{1 - \exp[-t_{film}/(\lambda_{film} \cos\theta)]}{\exp[-t_{film}/(\lambda_{film} \cos\theta)]}, \tag{3.28}$$

where D_{film} and D_{sub} are the atomic densities of the elements in film and substrate, respectively, given in mol/cm^3 (cf. Refs. [93, 94]). Assuming equal IMFPs in substrate and film, the equation can be rearranged as follows to yield the film thickness t_{film}:

$$t_{film} = \lambda_{film} \cos\theta \ln\left(\frac{N_{film} D_{sub}}{N_{sub} D_{film}} + 1\right). \tag{3.29}$$

For the case of two homogeneous layers stacked on top of the substrate surface (e.g. a film and an interface layer) their thicknesses can be determined with the following formulae under the same assumptions as above:

$$t_{int} = \lambda_{film} \cos\theta \ln\left(\frac{N_{int} D_{sub}}{N_{sub} D_{int}} + 1\right), \tag{3.30a}$$

$$t_{film} = \lambda_{film} \cos\theta \ln\left(\frac{N_{film} D_{sub}}{N_{sub} D_{film}} \exp[-t_{int}/\lambda_{int}] + 1\right). \tag{3.30b}$$

3.2.5 Charge-transfer satellites and stoichiometry in the Fe 2p spectrum

Core-level spectroscopy of transition-metal compounds is a prominent example for the occurrence of satellite lines due to excitations of the remaining $(N-1)$-electron system (cf. Sec. 3.2.2). The Fe 2p core level, which exhibits the most intense XPS spectrum of Fe, is considered in the following.

Fe $2p$ spectra for different iron compounds are displayed in Fig. 3.8. In addition to the spin-orbit splitting into $2p_{3/2}$ and $2p_{1/2}$ lines and the chemical shift of the main lines caused by the different chemical environment of the Fe ions, so-called charge-transfer (CT) satellites are clearly visible as indicated by vertical lines.

In principle, the spectrum consists of several final-state excitations due to correlation among the Fe $3d$ electrons and hybridization and charge transfer between Fe $3d$ and O $2p$ states. The designation CT originates from the charge transfer between the transition metal's $3d$ orbital and a ligand's shell L. The multiplet splitting corresponds to different configurations of the $2p$ and $3d$ electrons in the excited final state with each of them having an own energy. However, the energy difference between multiplet states is smaller than the experimental energy resolution in the case of the Fe $2p$ core level, which gives rise to the broadness of both main and satellite line.

In the ground state, the ligand shell L is completely filled and the electronic configuration of Fe^{2+} and Fe^{3+} is $3d^6$ and $3d^5$, respectively. According to configuration interaction theory the two most intense final states of the photoemission process are the 'poorly-screened' state $3d^nL$ and the 'well-screened' state with charge transfer from L to $3d$, namely $3d^{n+1}L^{-1}$. The latter state is normally assigned to the main line. Its binding energy varies strongly for different ligands (here O and S) due to their different CT energies [87]. Because of stronger screening of the core hole this $3d^{n+1}L^{-1}$ state has the lower binding energy. The binding-energy difference between charge-transfer satellite and main peak is roughly $Q - \Delta$ with the core potential $Q \approx 8\,\mathrm{eV}$ and the p-d charge-transfer energy $\Delta \approx 2\,\mathrm{eV}$ and $4\,\mathrm{eV}$ for Fe^{3+} and Fe^{2+}, respectively [87, 95].

Qualitatively, it is often easier to obtain the Fe oxidation state from the occurrence of the charge-transfer satellites than by measuring the relatively small chemical shifts of the main-line positions. In case of Fe_2O_3 the Fe^{3+} charge-transfer satellite is visible at 719 eV, and for FeO the Fe^{2+} satellite appears at 716 eV. Table 3.5 lists these characteristic positions of main peaks and CT satellites of the Fe $2p$ spectrum of the iron compounds which are displayed in Fig. 3.8.

For the mixed valence state of Fe_3O_4, both CT satellites add up in such a way that the main line broadens and the spectral region between the main lines is smooth and structureless. When performing epitaxy, all iron-oxide phases can possibly be grown, and consequently Fe/O ratios ranging from 0.66 to 1.00 can be obtained. Therefore, it is a formidable task to grow and measure the exact composition. In this thesis the stoichiometry is determined by decomposing background-corrected experimental spectra of thin films into experimental spectra taken from reference compounds (see Fig. 3.8). For this procedure it is assumed that the spectrum of a non-stoichiometric sample is the superposition of reference spectra. The respective linear combination of reference spectra which yields the smallest difference to the analyzed spectrum in the sense of the smallest root-mean-square deviation is then taken to calculate the actual stoichiometry. To illustrate this method, the spectra for the reference compounds (Fe/O ratios of 0.66, 0.75, 1.00) and some intermediate, calculated spectra (Fe/O ratios 0.69, 0.72, 0.90, 0.95) are displayed in Fig. 3.8(b).

This method possibly exhibits a small error due to the usage of hematite instead of maghemite as a reference compound since an overoxidized epitaxial film is more likely maghemite- than hematite-like. Fujii *et al.* [95] investigated the Fe 2*p* spectrum of hematite and maghemite by means of XPS and cluster calculations and found that a small difference exists between the spectra of both compounds due to the spectral weight from Fe^{3+}_{tet} ions, which show more covalent character of their oxygen bonds compared to octahedral sites. The main-line position differs by 0.2 eV with hematite possessing the higher binding energy at 710.9 eV, and also the intensity of the CT satellite is decreased for maghemite. Earlier studies, however, did not report this difference in the spectra [96, 97].

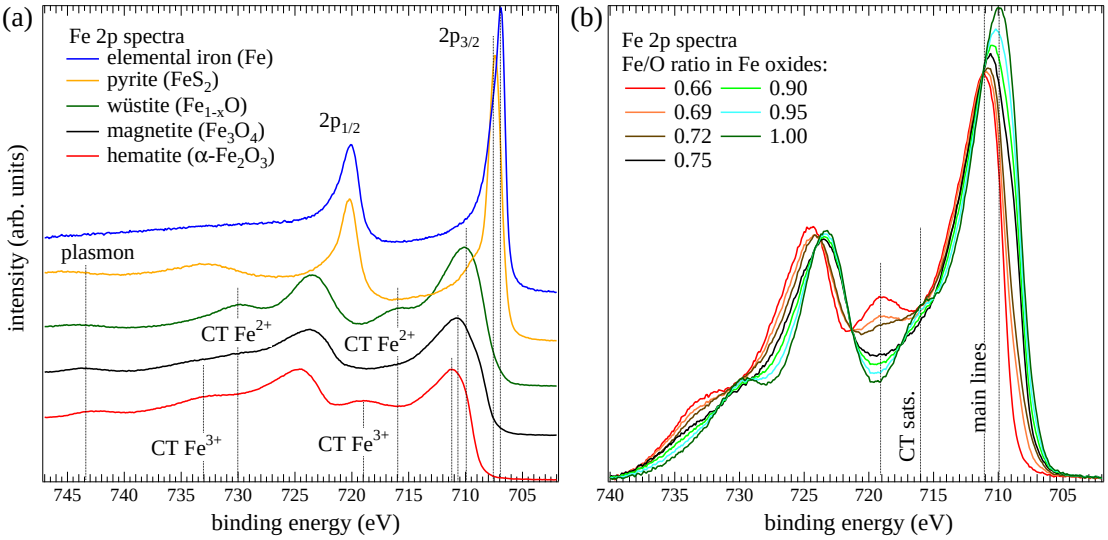

Figure 3.8: *(a) Fe 2p spectra of elemental iron (Fe), pyrite (FeS_2), wüstite ($Fe_{1-x}O$), magnetite (Fe_3O_4), and hematite (α-Fe_2O_3). (b) Background-corrected Fe 2p spectra of iron oxides with various Fe/O ratios.*

Table 3.5: *Characteristic peak positions in the Fe 2p spectrum for different iron compounds read off from spectra including background. Cf. Refs. [97–99].*

compound	Fe $2p_{3/2}$ main line	Fe $2p_{1/2}$ main line	Fe $2p_{3/2}$ CT sat.
Fe	706.9	720.1	no
FeS_2	707.4	720.2	709.4
FeO	710.0	723.5	716.0 (Fe^{2+})
Fe_3O_4	710.7	723.8	both Fe^{2+} and Fe^{3+}
α-Fe_2O_3	711.2	724.5	719.0 (Fe^{3+})

3.2.6 Valence-band and oxygen spectra of different iron oxides

There are two more spectral levels which are important for the investigation of iron oxides, viz. the valence band (VB) and the O 1*s* level. Figures 3.9(a) and (b) display the VB and O 1*s* spectra of different iron oxides, respectively.

The XPS VB spectra shown in Fig. 3.9(a) are dominated by the contribution of Fe 3*d* states because of their larger photoionization cross section compared to O 2*p* states in the x-ray regime (here Al-K_α radiation). The O 2*p* emission is known to exhibit a single broad maximum between 2 and 8 eV binding energy and to be almost identical for all iron oxides [100]. All spectral features are in good agreement with the XPS study of the VB from Fujii *et al.* [95]. The VB consists of a main band from 0-10 eV and a satellite band from 10-17 eV which is due to charge transfer as explained above. Peaks at about 0.8 and 3.8 eV and spectral weight at the Fermi level, E_F, are the spectral signal coming from Fe^{2+}_{oct} sites, which are the only sites present in wüstite. Peaks observed at 2.7, 4.9, and 7.2 eV are representative for the Fe^{3+}_{oct} sites present in hematite. The hematite spectrum clearly shows an insulating gap. As was shown by Fujii *et al.* [95] simulated and experimental VB spectra from Fe^{3+}_{tet} (present amongst others in maghemite) and Fe^{3+}_{oct} (in hematite) are very similar for the main-band region with the biggest difference being that less spectral weight is seen in the satellite-band region for hematite. Therefore, in a local picture the VB spectrum of magnetite should be approximately a 2:1 superposition of the hematite and the wüstite spectrum. Indeed, all the spectral features can be consistently assigned to different Fe sites as indicated in Fig. 3.9(a). Thus, the lineshape of the VB can qualitatively be analyzed to judge the Fe stoichiometry. Especially, the spectral weight near to E_F from Fe^{2+}_{oct} sites is very sensitive to the surface preparation (cf. Ref. [101]).

The O 1*s* main peak is located at a binding energy of 530.1 ± 0.2 eV for all three shown iron oxides (cf. Fig. 3.9(b)), which is in perfect agreement with other XPS studies [95, 96, 102]. Therefore, it is used as an energy reference in this thesis in order to compensate for possible charging effects where necessary. The line shape is clearly asymmetric without significant change between the three compounds. This asymmetry on the high binding-energy side can be fitted by an additional, broader peak at a binding energy of about 531.3 eV (see Fig. 3.9(b)). Similar asymmetries of the O 1*s* peak are reported in the literature and different explanations for it were offered, such as residual hydroxylation [103], non-stoichiometric O-content of the surface, an intrinsic shake-up satellite [104], or CO-bonding [105]. Since this asymmetry is the same for all three compounds it is obviously not an intrinsic property of the magnetite surface like Chambers and Joyce suggested [104]. Also, the presence of CO-bonding can be excluded for the shown spectra, since the surfaces were obtained by filing crystalline material and showed no remaining carbon as proved by the absence of any discernible C 1*s* signal. Therefore, this peak is attributed to OH-groups on the surface. As is later discussed this asymmetry is more pronounced for surfaces previously exposed to atmospheric conditions. It therefore reflects the amount of contamination with dissociated water. The contribution of this

OH-signal to the O 1s spectrum tampers the ratio of spectral weights Fe 2p/O 1s, especially for *ex situ* prepared surfaces. For this reason, the Fe/O stoichiometry was evaluated by the comparison of Fe 2p spectra as explained in Sec. 3.2.5, if possible.

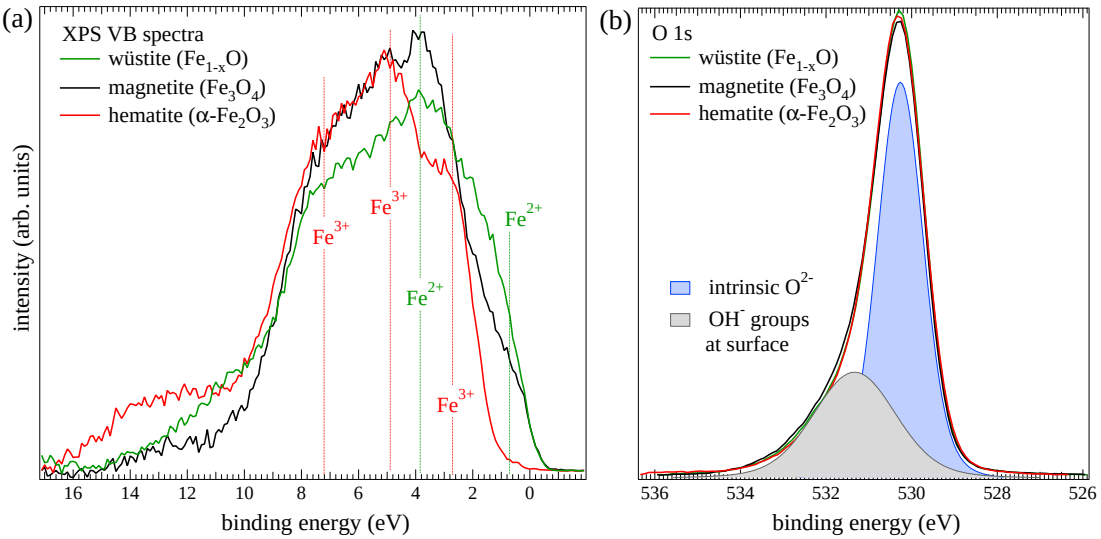

Figure 3.9: *(a) XPS VB spectra of of wüstite ($Fe_{1-x}O$), magnetite (Fe_3O_4), and hematite (α-Fe_2O_3). (b) O 1s spectra of the same compounds.*

3.3 Magnetic circular dichroism in x-ray absorption spectroscopy

3.3.1 Principle

X-rays are absorbed in matter according to the Beer-Lambert-law given in Eq. (3.31). The x-ray intensity, $I(x)$, is exponentially damped with increasing penetration depth, x, inside the material:

$$I(x) = I_0 \cdot exp(-\mu x), \tag{3.31}$$

where $\mu(E)$ is the energy-dependent x-ray absorption coefficient and I_0 is the incoming photon intensity. The absorption coefficient is approximately equal to the coefficient of photoelectric absorption in the relevant photon-energy region. Although x-ray absorption spectroscopy (XAS) and XPS therefore are closely related, they exhibit several differences. In a simplifying picture one can say that PES probes occupied states while XAS detects the unoccupied states right above the Fermi level.

The energy-dependent absorption coefficient, $\mu(E)$, shows an overall decrease with increasing photon energy. Only at specific absorption edges, which correspond to binding energies of electrons in certain shells, does the absorption increase sharply because the

energy becomes large enough to excite respective electrons into states above the Fermi level (see Fig. 3.10). The choice of an absorption edge allows to be element-specific. With XAS one can investigate the fine structure at these absorption edges in detail.

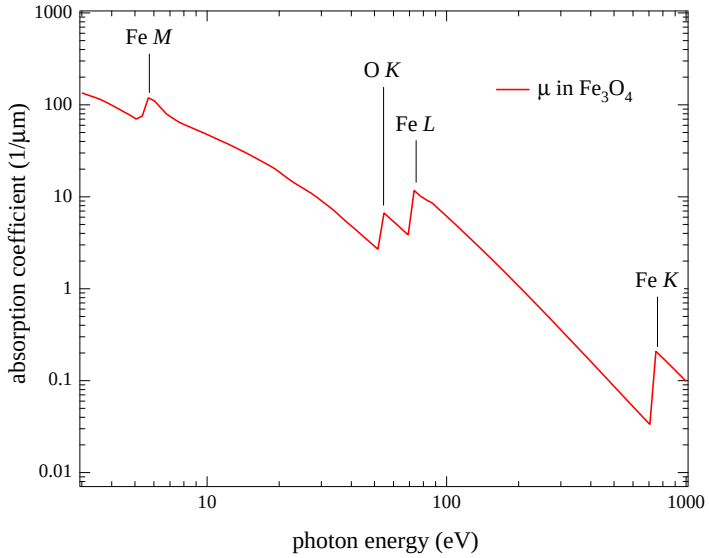

Figure 3.10: *X-ray absorption coefficient in Fe_3O_4, $\mu(E)$, with its important absorption edges which is tabulated in Ref. [106].*

If one wants to theoretically describe the resonant absorption process in a correct way, it is necessary to calculate μ with Fermi's Golden rule using initial and final states of the whole N-electron system, which is difficult without making major simplifications. Here, we only deal with a single-electron treatment and ignore the response of the remaining electron system to the absorption process. For the understanding of the basic concept of x-ray magnetic circular dichroism (XMCD), which is relevant for the scope of this thesis, it is sufficient to restrict oneself to the so-called two-step model at the L-edge of a transition metal (see Fig. 3.11). The first step of this model describes the excitation of a spin-polarized photoelectron from a spin-orbit split core level by circularly polarized light. In the second step, this electron is 'detected' by the spin-split final states. During the excitation the angular momentum of the photon is transferred to the photoelectron and its azimuthal quantum number, l, is changed. In the considered case of the L-edge $\Delta l = +1$ for the transition into $3d$ states. The magnetic quantum number, Δm_l, is changed according to the helicity of the absorbed photon. This is expressed in the following selection rules for transition between states $\|l, m_l, s, m_s\rangle$ which are valid within the dipole approximation:

$$\Delta l = \pm 1; \Delta m_l = 0, \pm 1; \Delta s = 0; \Delta m_s = 0. \tag{3.32}$$

A detailed view of the electronic levels and the possible transitions induced by right-

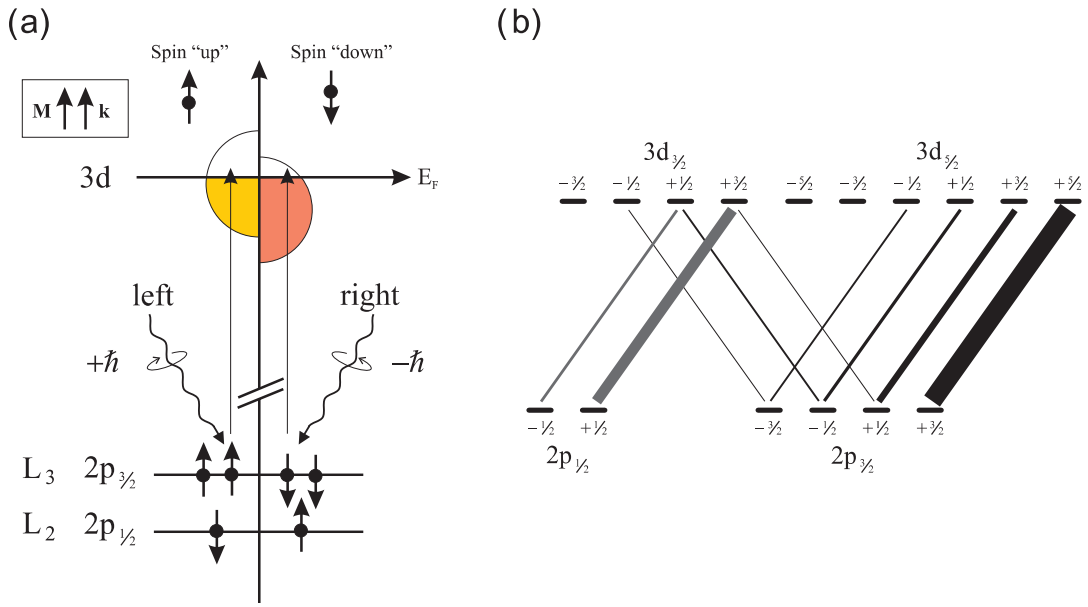

Figure 3.11: *Schematic description of the XMCD effect at the L-edge of a transition metal in the two-step model taking into account only 3d final states. (a) Excitation of a spin-polarized photoelectron from the spin-orbit split 2p initial state by circularly polarized light. The spin-split unoccupied 3d final states act as a spin filter for this photoelectron. (b) Detailed view of involved electronic levels and their corresponding quantum numbers of the total angular momentum, j and m_j. The latter obey the dipole selection rules $\Delta j = +1$ and $\Delta m_j = +1$. The line thickness indicates the transition probability. Taken from Ref. [107].*

handed circularly polarized light is given in Fig. 3.11(b) and Fig. 3.12. The initial states are sorted according to their total angular momentum and corresponding magnetic quantum number. Their associated quantum numbers m_l and m_s are additionally listed in Fig. 3.12. The transition probabilities to the final states is visualized by the thickness of the arrows and specified in percentages separately for the L_3- and L_2-edge. Theses probabilities can be calculated from angular matrix elements [109]. For the $3d$ final states the $m_s = -1/2$ and $m_s = +1/2$ states are framed by a rectangle and an ellipse, respectively. It can be seen that the selection rules $\Delta m_l = +1$ and $\Delta m_s = 0$ are obeyed. Summing up probabilities, it follows that right-handed circularly polarized light preferentially (62.5 %) excites majority-spin electrons at the L_3-edge and preferentially (75 %) minority-spin electrons at the L_2-edge of a transition metal. Spin and orbital polarizations of both absorption edges are given at the lower margin of Fig. 3.12. Upon changing the light-polarization to left-handed circular, both polarizations simply reverse their sign. Note that if there were no spin-orbit splitting of the $2p$ state, the resulting spin polarization would be canceled out.

The distinction between majority-spin and minority-spin electrons, however, is only possible inside a magnetized material. Here, the discrepancy between absorption spectra

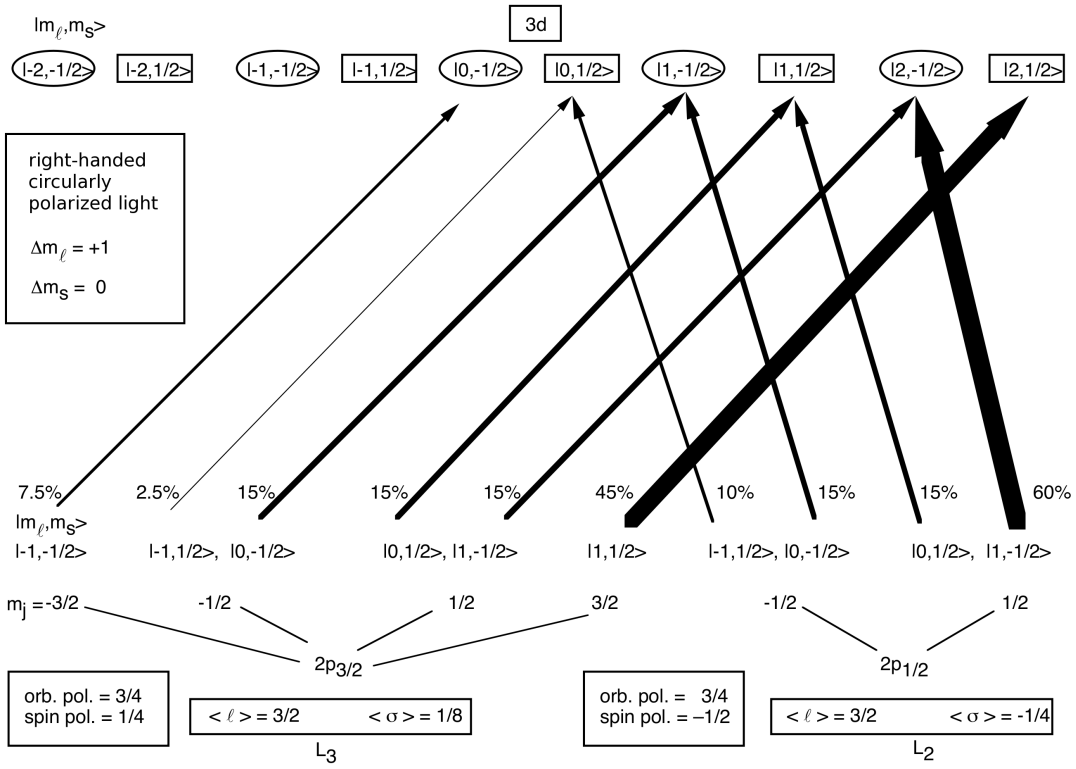

Figure 3.12: *Possible 2p→3d transitions, which can be excited by right-handed circularly polarized light, and their corresponding probabilities. The transitions are listed according to their quantum numbers m_l and m_s. The resulting spin and orbital polarizations are indicated. Adopted from Ref. [108].*

taken with parallel (μ_+) and antiparallel (μ_-) alignment of light helicity and magnetic field direction is a measure for the difference in majority- and minority-spin bands of the final states and hence of the net magnetization. In the experimental setup used here magnetic field and light helicity were always collinear[1]. The magnetic field was reversed to switch between parallel and antiparallel alignment. The so-called sum rules deduced by Thole *et al.* [111] and Carra *et al.* [112] quantify the spectral discrepancy between both alignments and allow the determination of spin (m_{spin}) and orbital magnetic moment (m_{orb}) in units of μ_B/atom by means of an energy integration over XMCD and XAS spectra:

$$m_{orb} = -\frac{4q}{3r}(10 - n_{3d}), \tag{3.33}$$

$$m_{spin} = -\frac{6p - 4q}{r}(10 - n_{3d})\left(1 + \frac{7\langle T_z\rangle}{2\langle S_z\rangle}\right)^{-1}, \tag{3.34}$$

[1]All XMCD measurements were performed using the "superconducting 3 T UHV magnet"-endstation of Prof. Dr. K. Fauth at beamline PM-3 at BESSY II in Berlin. Cf. Ref. [110].

where p, q and r are the following integrals over the XAS and XMCD spectra:

$$p = \int_{L_3} \mathrm{XMCD} = \int_{L_3} (\mu_+ - \mu_-) dE, \tag{3.35}$$

$$q = \int_{L_3+L_2} \mathrm{XMCD} = \int_{L_3+L_2} (\mu_+ - \mu_-) dE, \tag{3.36}$$

$$r = \int_{L_3+L_2} \mathrm{XAS} = \int_{L_3+L_2} (\mu_+ + \mu_-) dE. \tag{3.37}$$

The quantity $(10-n_{3d})$ is the number of $3d$ holes in the VB of the material. In accordance with Goering *et al.* [113] and Huang *et al.* [114] n_{3d} was assumed to be 4.5 per Fe atom in our analysis.

Furthermore, $\langle S_z \rangle$ is the expectation value of the spin operator along the z axis in units of $\hbar$, which is simply $-m_{spin}/2$ with the spin moment given in units of μ_B. The term $\langle T_z \rangle$ is the expectation value of the magnetic dipole operator, which measures the asphericity of the spin-density distribution. The ratio $7\langle T_z \rangle / 2\langle S_z \rangle$ is very often ignored in the literature. It is exactly zero for an octahedral coordination and vanishing spin-orbit coupling. A short discussion of the error introduced by this neglect is given in Sec. 4.5.3. All experimental results of the sum-rule analysis in the following chapters are given as an effective spin moment $m^*_{spin} = -\frac{6p-4q}{r}(10 - n_{3d}) = m_{spin} + 7\langle T_z \rangle$, which is equal to the real spin moment for vanishing $\langle T_z \rangle$.

The necessary steps for the sum-rule analysis of experimental spectra shall be shortly visualized here on the basis of Fe L-edge spectra of Fe_3O_4. Experimental raw data are normalized to the incoming photon intensity and matched outside the resonance to tabulated values of the absorption cross section of Fe_3O_4 given by Henke *et al.* [106]. This is shown in Fig. 3.13(a). It allows for a conversion of the intensity scale into absolute units of the absorption coefficient. Before actual sum-rule analysis, a step function with two smooth steps at the positions of the L_3- and L_2-edges has to be subtracted to cancel the contribution of the unoccupied Fe $4s$ states to the XAS spectrum. A step function is a reasonable approximation if the Fe $4s$ DOS is assumed to be flat (see Fig. 3.13(b)).

Figure 3.14 shows an example of desaturated (for an explanation of saturation effect see Sec. 3.3.2) Fe L-edge XAS and XMCD spectra of Fe_3O_4. It is clearly seen that the XMCD is non-zero only at a small energy interval close to the resonance. The exact energy window, where the integral is evaluated, affects the result of the sum rules. In particular, the orbital moment is strongly influenced while the spin moment is largely unaffected and changes only by approximately 1 % for different integration ranges. While Goering *et al.* [113] obtained a nearly quenched orbital moment of less than $0.02\,\mu_B$ with a long integration range, which is approximately equal to the range employed in the current work (see labels in Fig. 3.14), Huang *et al.* [114] implemented a considerably shorter integration range until 740 eV and reported on large orbital moments of about $0.66\,\mu_B$. Goering *et al.* argue that magnetic extended fine-structure oscillations of

the L_3-edge are superimposed to the L_2-edge signal, the contribution of which is only canceled for the long integration range extending to 764.5 eV.

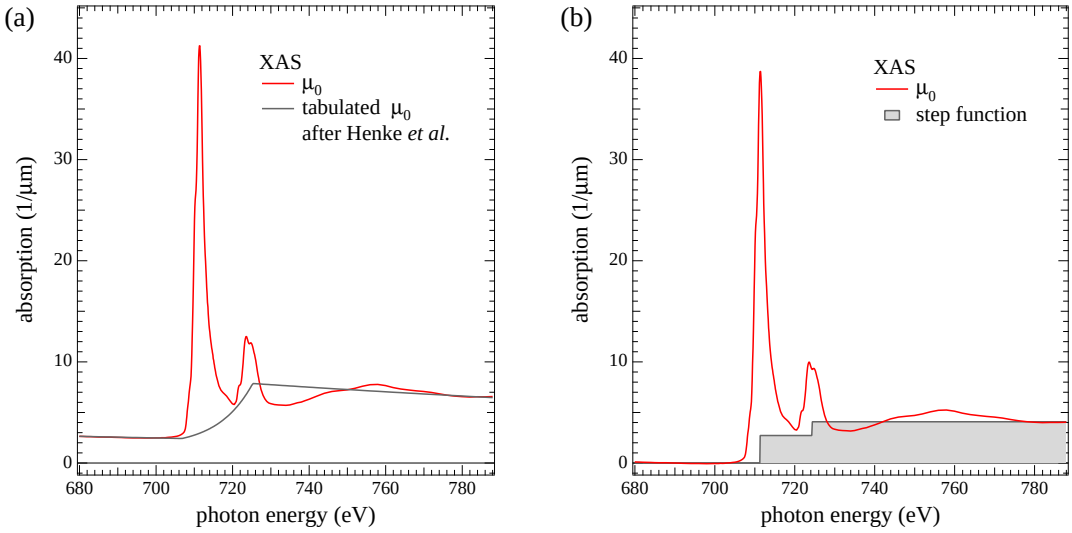

Figure 3.13: *Data handling of XAS Fe L-edge spectra. (a) Fit of an experimental XAS spectrum to the absorption coefficient tabulated by Henke et al. [106]. (b) Subtraction of a step function from the experimental spectrum in order to remove the contribution of the unoccupied Fe 4s states.*

3.3.2 Electron yield, saturation effects, and probing depth

There are several methods to measure an XAS spectrum, $\mu(E)$. The transmission method measures the transmitted photon intensity behind the sample by means of a photon detector. This method is direct and 'bulk-sensitive' but only useful for a sufficiently thin sample with a thickness smaller than $2/\mu_{max}$. In contrast, fluorescence yield and electron yield methods detect $\mu(E)$ indirectly via measurement of the radiative and electronic decay of excited electrons in the sample, respectively. Both suffer from saturation effects which are due to the absorption of x-ray intensity inside the material. Since the absorption strongly depends on E, photons with different energy are unequally absorbed at various depths inside the sample. As a consequence absorption peaks in the spectra are more and more reduced for larger depth of origin of the signal.

In total electron yield (TEY), one measures the sample drain current, $Y_e(E)$ which is proportional to the number of electrons which leave the sample as a result of the absorption process. This current is related to $\mu(E)$ by the following equation [115]:

$$Y_e(E) = Cf\mu = \left(\frac{I_0 G \lambda_e}{\cos\psi}\right) \cdot \left(\frac{1}{1+\lambda_e/(\lambda_x \cos\psi)}\right) \mu, \tag{3.38}$$

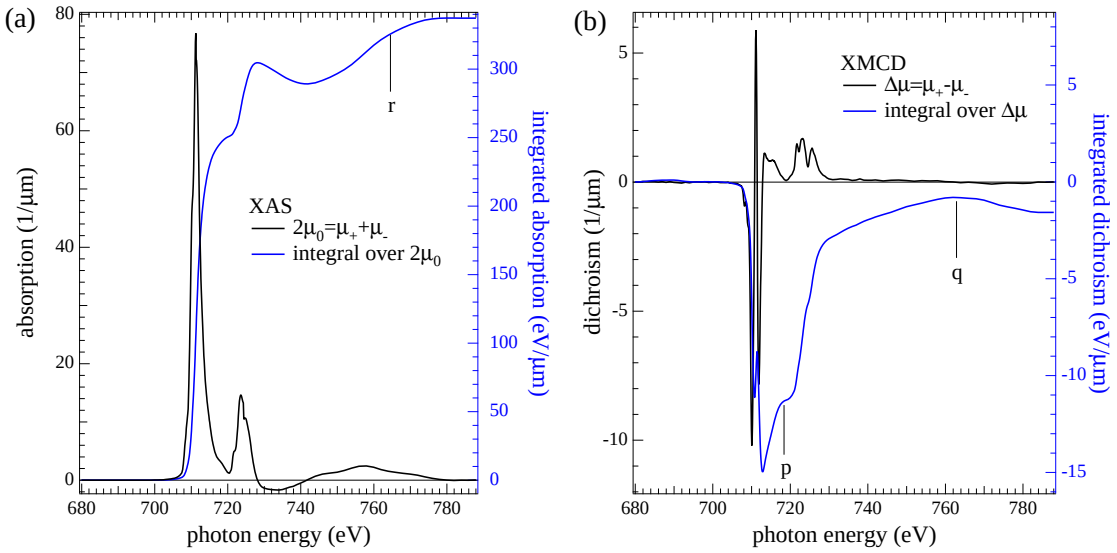

Figure 3.14: *(a) XAS and (b) XMCD Fe L-edge spectra of Fe_3O_4 and appropriate integrals used for sum-rule analysis. Integral values p, q, and r are indicated for typically employed integration ranges.*

where I_0 is again the incoming photon intensity, G is the electron gain function, ψ is the x-ray incidence angle with respect to the sample normal, λ_x is the x-ray penetration length, and λ_e is the electron escape depth in the material. The electron gain function G is proportional to the photon energy and describes the average number of electrons produced in a cascade process started by a single Auger electron after filling of the core hole.

The x-ray penetration length is simply the inverse of the linear absorption coefficient, $\lambda_x = 1/\mu$, and as such energy-dependent. Note that the electron escape depth, λ_e, is not the same as the IMFP described in Sec. 3.2.3, because elastically scattered electrons also contribute to the probing depth of XAS. The term $(\lambda_x \cos\psi)$ is the x-ray penetration depth, i.e., the penetration length projected along the surface normal. By changing the incidence angle, ψ, one changes the surface sensitivity of the measurements and at the same time the magnetization direction inside the sample for our used experimental setup.

The first factor C is simply a proportional constant which increases for enlarging λ_e and ψ, i.e., for more grazing incidence. The second term f describes the saturation effects in TEY mode. It critically depends on the ratio of electron escape depth to x-ray penetration depth. If this ratio is small, there is no saturation effect. On the other hand, if it is large, the electron yield signal is completely saturated and not proportional to μ anymore. The ratio, where the present data were taken, is intermediate, and so the raw data had to be desaturated. Since the electron escape depth is not exactly known

and can in principle differ for various samples, the desaturation was done by an iterative selection of values for λ_e until spectra taken under different ψ matched with each other.

3.3.3 X-ray magnetic circular dichroism of Fe *L*-edge

This section describes some of the information which can be extracted by performing XMCD at the Fe *L*-edge of magnetite. Figures 3.15(a) and (b) show XAS and XMCD

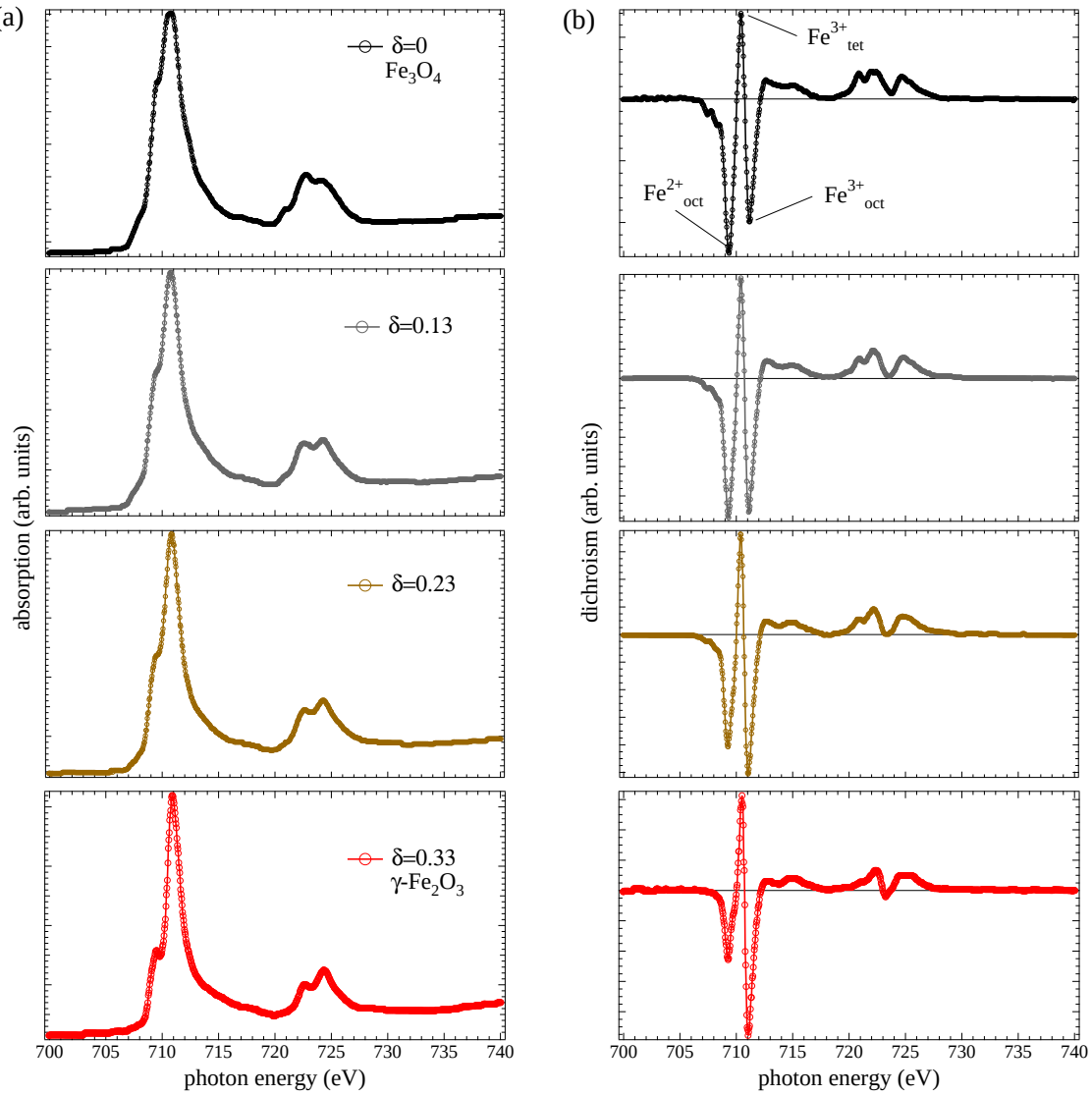

Figure 3.15: *(a) XMCD and (b) XAS Fe L-edge spectra of $Fe_{3-\delta}O_4$ for various off-stoichiometry parameters δ measured by Pellegrin et al. Adopted from Ref. [116].*

spectra of $Fe_{3-\delta}O_4$ measured by Pellegrin *et al.*, respectively. Strong spectral changes are visible between the four indicated stoichiometries. The assignment of the Fe valencies

and sites to the three single peaks at the L_3-edge of the experimental XCMD spectrum of stoichiometric Fe_3O_4 (see labels in Fig. 3.15(b)) can be found in various reports [116, 117]. It was first proposed by Kuiper *et al.* based on their calculations of atomic multiplet spectra [117]. Their calculations model a single Fe ion in an appropriate crystal field. They could achieve satisfactory agreement between calculated and experimental spectra by permitting relative energy shifts and broadening of the three single spectra.

The intensity of the Fe^{2+}_{oct} peak decreases strongly with increasing δ (see Fig. 3.15(b)). However, there is still some intensity of this peak in the γ-Fe_2O_3 spectrum which demonstrates that some spectral weight at this position is caused by other sites and valencies. Similarly to the decrease of the Fe^{2+}_{oct} peak, the Fe^{3+}_{oct} peak intensity enlarges as is expected due to the higher oxidation state. On the other hand, the Fe^{3+}_{tet} peak is almost constant since the occupation of these sites does not vary with the off-stoichiometry (cf. Tab. 2.1).

The strong spectral differences can be used to extract the stoichiometry from experimental spectra by comparing them quantitatively with the data from Pellegrin *et al.* [116]. This was done by fitting the experimental spectrum by a linear combination of the reference spectra with different δ and calculating the off-stoichiometry parameter δ from the amplitudes of the fit components.

The peak structure of the XCMD Fe L_3-edge spectrum can be employed to measure valence- and site-specific magnetization curves. This is implemented by measuring the sample drain current at the fixed photon energy position of the relevant peak and varying the magnetic field. The on-resonance data are normalized by data taken at a pre-edge position to remove the non-MCD related signal.

4 Magnetite thin films on ZnO

The upcoming chapter deals with the Fe_3O_4/ZnO structure which is largely unexplored in literature. Semiconducting, translucent ZnO is employed in a variety of industrial applications, e.g., as blue light-emitting diode [118]. Despite its large band gap of about 3.2 eV it is an n-type semiconductor due to intrinsic and extrinsic defects, such as Zn antisites, Zn interstitials, O vacancies, or H impurities [119]. Therefore, it exhibits a sufficiently high conductivity to observe no charging effects in electron diffraction or spectroscopy even at room or lower temperatures, which is an asset for doing surface science. Moreover, there exists much know-how in using ZnO as a substrate for epitaxy of GaN in the literature. Both facts facilitate the application of ZnO as a substrate to the work at hand. It is a handy material which combines the technological options of a semiconductor with the chemical resistance towards oxygen common to oxidic materials. Moreover, spin coherence was verified in ZnO up to room temperature [120].

At first, some basic physical properties of ZnO shall be summarized. ZnO can be considered as the ionic limit of the tetrahedrally coordinated semiconductors which exhibit the hexagonal wurtzite structure (space group $P63mc$). In the ionic picture, Zn^{2+} and O^{2-} are tetrahedrally coordinated by each other in this structure. O planes with an in-plane lattice parameter of 3.25 Å are stacked hexagonally closed-packed in c-axis direction (lattice constant of 5.21 Å) and sandwich Zn planes non-symmetrically, i.e., the distances between a Zn plane and its upper and lower adjacent O plane are not equal. Therefore, the crystal structure has no inversion centre and the space group is called polar. This asymmetry is the reason why the two ends of a ZnO crystal along the c axis are not equivalent. When cleaving a ZnO crystal along this axis, one cleavage surface will always be O- and the other one Zn-terminated. The two terminations are expected to exhibit different physical and chemical properties.

Different mechanisms for the cancelation of the polarity of ZnO surfaces were suggested in literature. Scanning tunneling microscope (STM) images of the Zn-terminated surface showed a characteristic topography consisting of triangular islands with inner holes or triangular pits separated by single-layer steps from the rest of the terrace [121]. In a later STM study, Dulub *et al.* observed that the shape of these islands is size-dependent, and interpreted the introduction of O-step edges and the associated decrease of the Zn-atom concentration at the surface as a mechanism to cancel the polarity [122]. Recent studies by Valtiner *et al.* propose the formation of a hydroxide phase at the Zn-terminated surface in a humid atmosphere to cancel the polarity [123, 124]. For the O-terminated surface, stabilization through adsorption of H or through formation of a (1×3) reconstruction consisting of rows of O vacancies have been put forward [125, 126].

4.1 Substrate preparation and growth procedure

Commercial substrates, which are mechanically polished in 'epitaxial-ready' quality, were purchased from different vendors for the use as templates. ZnO crystals grown by the hydro-thermal method from MaTecK GmbH, CrysTec GmbH, or Coating & Crystal Technology Inc. were found to exhibit good crystallinity as signaled by an x-ray diffraction (XRD) rocking curve of down to 0.01° full width at half maximum (FWHM) for CrysTec crystals. However, hydrothermal crystals contain impurities such as alkali, alkaline-earth, or transition metals in the low ppm regime according to an impurity analysis provided by MaTecK GmbH. It has to be paid attention to the fact that such impurities can diffuse to and enrich at the surface during prolonged annealing [127]. In contrast, crystals from high-purity melt growth provided by Cermet Inc. [128] are believed to contain a lower impurity concentration especially of alkali metals, but were found to be of inferior crystal quality in XRD rocking curves and are considerably more expensive.

Before actual growth the ZnO substrates were cleaned *in situ* by cycles of sputtering with Ar^+ ions of 1 keV energy and annealing at 700 to 800°C in an oxygen partial pressure of typically $p(O_2) = 5 \cdot 10^{-6}$ mbar. Low-energy electron diffraction (LEED) or RHEED analysis of substrates prepared in this way yielded sharp, unreconstructed patterns indicating good surface crystallinity. Some substrates exhibited reconstructed surfaces if they were extensively annealed without an intermediate sputtering cycle [129]. It is conjectured that these reconstructions are related to the surface segregation of the above mentioned impurities.

Fe and O_2 were co-deposited onto ZnO at temperatures ranging from 400 to 530°C (see Tab. A.1). Such growth temperatures are somewhat larger than the typical values used for deposition onto MgO to promote sufficient surface diffusion and a good resulting crystallinity of the film. For ZnO the problem of interdiffusion of Zn across the interface is less severe than in the case of Mg in Fe_3O_4/MgO interfaces.

Some growths were performed with a constant Fe/O_2 flux ratio (see Eq. (3.5)) while for other samples this ratio was adjusted during growth to avoid an Fe^{2+}-rich interface layer as explained in Sec. 4.4. This is marked in Tab. A.1 in the appendix. The *oxide* growth rate was set to 2.33 ± 0.05 Å/min as estimated from x-ray reflectivity (XRR) results of relatively thick films. As was explained in Sec. 3.1.1, this overall growth rate is not equal to the impinging Fe flux listed in Tab. A.1.

4.2 Structural characterization

4.2.1 Surface structure

Figure 4.1(a) shows a typical LEED pattern obtained from an Fe_3O_4/ZnO thin film. The schematic LEED pattern in Fig. 4.1(b) explains the different contributions of the

sublattices. The blue unit cell and lattice points correspond to the O sublattice. This blue sublattice would also be visible for a ZnO or FeO surface (ignoring the lattice mismatch). The red sublattice forms a (2×2) superstructure in relation to the blue one. It shows the additional periodicity due to the Fe sublattice which exists only for the surface of a spinel such as magnetite or maghemite. Sharp diffraction spots and low background intensity prove the good surface crystallinity of the present samples.

A quantitative comparison of LEED patterns obtained from grown films and substrates allows for the determination of the lattice constant. The lattice constant of the O sublattice typically is 3.0 ± 0.01 Å thus indicating that the lattice is almost but not completely relaxed. For pseudomorphic growth the lattice constant would be the one for ZnO, namely 3.25 Å, and for relaxed growth it would be equal to the O-O distance in bulk magnetite, viz. 2.97 Å. The actual growth mode will be further discussed below on the basis of the RHEED results. The lattice constant of the complete Fe_3O_4 unit cell is two times the lattice constant of the O sublattice, i.e., about 6.0 Å.

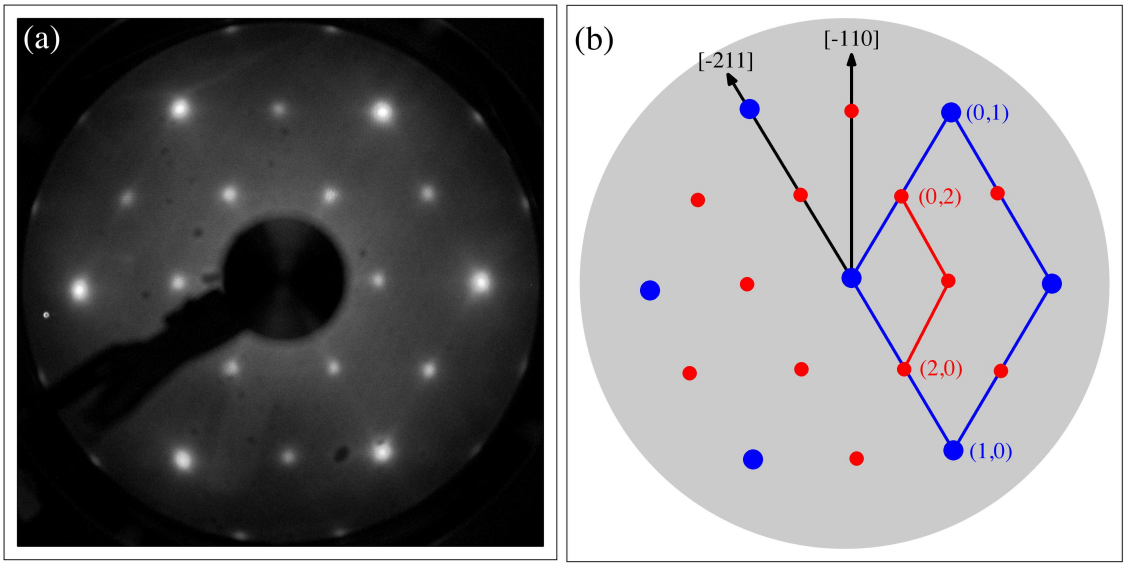

Figure 4.1: *(a) LEED pattern of a 16 nm thick Fe_3O_4/ZnO film (sample no. 1, see Tab. A.1). Electron energy $E = 56.9$ eV. (b) Reciprocal unit cells and diffraction spots are labeled according to the O sublattice common to ZnO and Fe_3O_4 (blue) and the superstructure due to the Fe sublattice (red). The crystal directions of Fe_3O_4 are indicated (black).*

Figure 4.2 shows an integrated RHEED-image profile as a function of film thickness and growth time. The intensity has been normalized and plotted as a color-coded two-dimensional map to highlight the position of reciprocal lattice points. After an increase of the specular spot intensity in the first 2 Å of growth ('half an oscillation') it decreases continuously for the rest of the growth time. The lack of oscillatory or constant intensity as a function of time indicates the absence of layer-by-layer or step-flow growth, respectively, and suggests surface roughening due to island-like growth. The diffraction

intensity of the {1,0} spots shifts to larger reciprocal lattice vectors after growth start. Also, after about 10 Å of growth additional {2,0} spots appear which gain intensity with growth time. This behavior is clarified by the exemplary k-profiles at $t = 0$ sec and $t = 240$ sec.

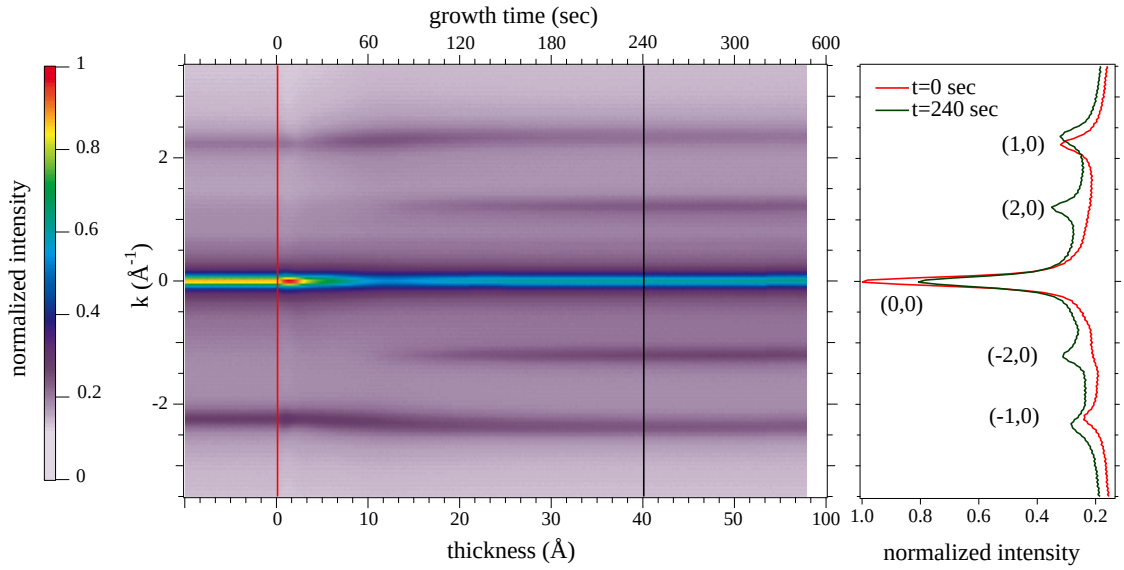

Figure 4.2: *Integrated RHEED-image profile as a function of time of an Fe_3O_4/ZnO growth measured with the incoming electron beam along the in-plane ZnO$[\bar{1}10]$ $\|Fe_3O_4[\bar{2}11]$ direction (sample no. 2).*

Measurements of the exact position of diffraction spots were used to determine the relaxation behavior of the growing film and its lattice constant. From Fig. 4.3(a) it can be derived that the initial layers of the film are wetting layers, which grow pseudomorphic, i.e., fully strained, on the substrate. At a thickness of 3 Å the growth mode undergoes a Stranski-Krastanov transition to island-like growth and the lattice starts to relax showing a large decrease of the lattice constant. At the theoretically predicted critical film thickness of 21 Å (see Tab. 3.2) this decrease is nearly finished and the lattice constant saturates. This final value of the lattice constant varies somewhat with the particular growth and ranges from 2.97 Å to 3.10 Å indicating incomplete relaxation in most cases. Since XRD results (see Sec. 4.2.3) demonstrate negligible strain at room temperature, there is a discrepancy which probably is related to the higher measurement temperature, at which RHEED patterns were taken, and thermal mismatch.

Figure 4.3(b) shows the evolution of the specular spot FWHM with film thickness. For the first few layers a superposition of substrate and film spots effects a spot broadening since the information depth of the high-energy electron beam is larger than the film thickness. At about 12 Å the FWHM starts to decrease along with the decrease of the strain relaxation. The FWHM is presumably dominated by the strain broadening contribution ω_ϵ, which is proportional to the lattice strain ϵ [81]. The broadening ω_L due

to finite grain size of the islands, L, is considerably smaller. On the basis of atomic force microscopy (AFM) results (see Sec. 4.2.2) the broadening ω_L is estimated to be about $0.001\,\text{Å}^{-1}$ according to $\omega_L = 57.32\lambda/L$ with $L = 300\,\text{Å}$ and $\lambda(E = 15\,\text{keV}) = 0.099\,\text{Å}$ [81, 130]. The specular spot FWHM of the grown film is $0.21\,\text{Å}^{-1}$, which corresponds to 1.19°, and thus is comparable to a literature report on oxide growth [81] and only sparsely larger than the value of ZnO substrate, indicating good surface crystallinity.

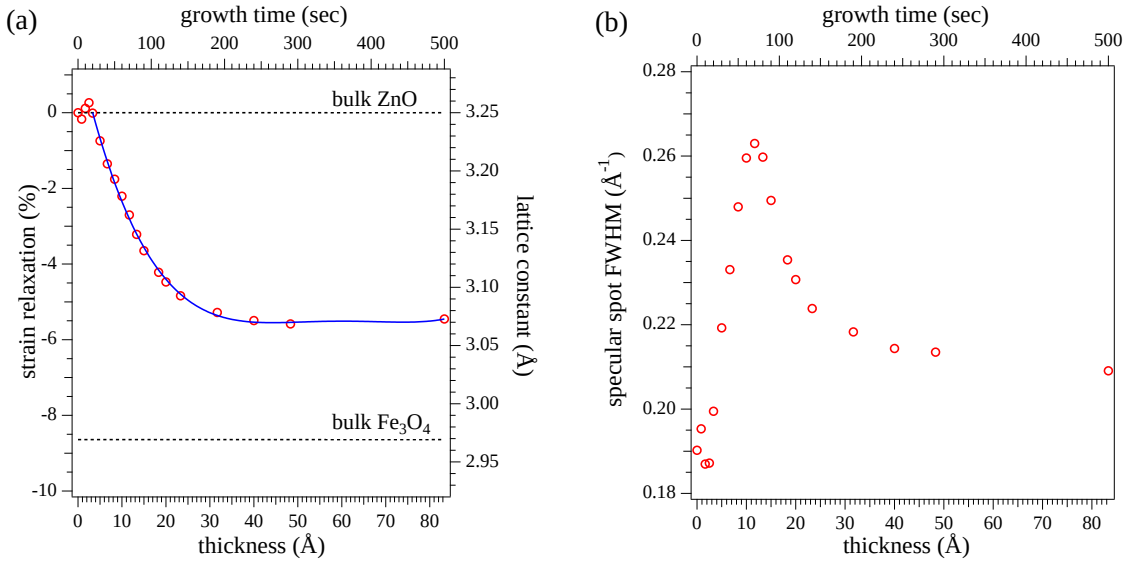

Figure 4.3: *Real-time RHEED characterization of an Fe_3O_4/ZnO film during growth (sample no. 2). (a) Relaxation of in-plane misfit strain as a function of growth time and film thickness. The blue line is a guide to the eye. (b) Peak width of the specular spot as a function of growth time and film thickness.*

The different stages of growth are also apparent in the bare RHEED images displayed in Fig. 4.4. The RHEED pattern of the ZnO surface (a) is intense and streaky although it displays some intensity modulation along the streak due to overlapping Kikuchi reflections. Pattern (b) stems from the initially grown FeO-like layer. It is streaky and Kikuchi lines are much less intense. Its rod spacing corresponds to a nearly pseudomorphic layer and with the corresponding lattice constant, which therefore is larger than that of the magnetite O sublattice. Pattern (c) exhibits the $\times 2$ reconstruction typical for a spinel type surface and is still streaky. In contrast, the pattern (d) shows spotty features distributed along the streak direction, especially for {2,0} spots. The transition from (c) to (d) in Fig. 4.4 occurs at thicknesses ranging from about 0 to 20 nm after the onset of the {2,0} spot intensity.

4.2.2 Surface morphology

In the following, an investigation of the surface morphology of thin films, which were grown in the MBE chamber in Vancouver and at a relatively high temperature of about

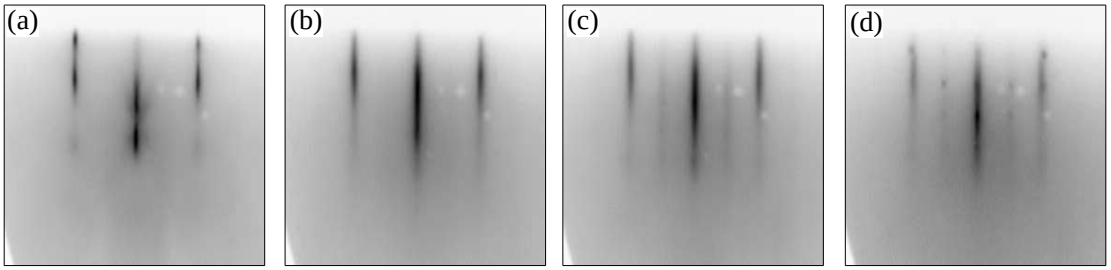

Figure 4.4: *RHEED patterns of an Fe_3O_4/ZnO film (sample no. 3) at different stages of growth taken along ZnO[$\bar{1}$10] ‖Fe_3O_4[$\bar{2}$11]. (a) Smooth ZnO substrate. (b) Smooth FeO-like initial layer. (c) Smooth Fe_3O_4 film. (d) Rough Fe_3O_4 film after transition to island-like growth.*

490°C, is presented (see sample nos. 4 and 5 in Tab. A.1). Figure 4.5 shows the surface topography of an Fe_3O_4/ZnO film (sample no. 4) as probed by atomic force microscopy (AFM) in tapping mode. Both images suggest that the Fe_3O_4 film is growing in island-like mode. The topography can be well described by consisting of islands with a typical width, w, of 100 to 300 nm and a height, h, of up to 3 nm. Islands exhibit one or more atomically flat terraces and mainly hexagonal and more rarely trigonal shapes. Alignment and shape of the islands suggest that the majority of growing material nucleates on present island tops and not between existing islands (cf. Fig. 3.3(b)). However, the island heights are considerably smaller than the film thickness, which demonstrates that the island coalescence has already begun at this point. Step heights between adjacent terraces of one island are typically about 1 nm suggesting that they consist of four atomic steps with a single height difference of 2.4 Å. In some cases these steps bunch preferably at island edges. Most of island edges are well aligned to each other presumably along a high symmetry crystal direction. Comparable film morphologies and island geometries have been found for Fe_3O_4/Pt(111) growth by Weiss and Ritter [18]. There, island edges were assigned to ($\bar{1}$11) and (2$\bar{1}\bar{1}$) crystal faces, which form contact angles of 70.5° and 90° to the substrate surface.

The overall root-mean-square (rms) surface roughness is about 1 nm, which is quite small. A 25 nm thick film (sample no. 5) possessed an increased surface roughness of about 10 nm indicating that the island-like growth mode is still at work for higher film thicknesses (see Fig. 4.6(a)).

The Fe_3O_4(111) surface features a three-fold rotational symmetry whereas the LEED pattern in Fig. 4.1 shows six-fold rotational symmetry with equal intensity of all diffraction spots. This implies the presence of two domains (rotational twinning). Another indication for simultaneous growth of two crystal domains is the occurrence of triangular islands which are rotated against each other by 180° as seen in the scanning electron microscope (SEM) image of a thick film (sample no. 6) in Fig. 4.6(b). A sketch of the close-packed O planes of such islands which are related to each other by twinning is given in Fig. 4.7(a). AFM images of thinner films in Figs. 4.5 and 4.6(a) prove the

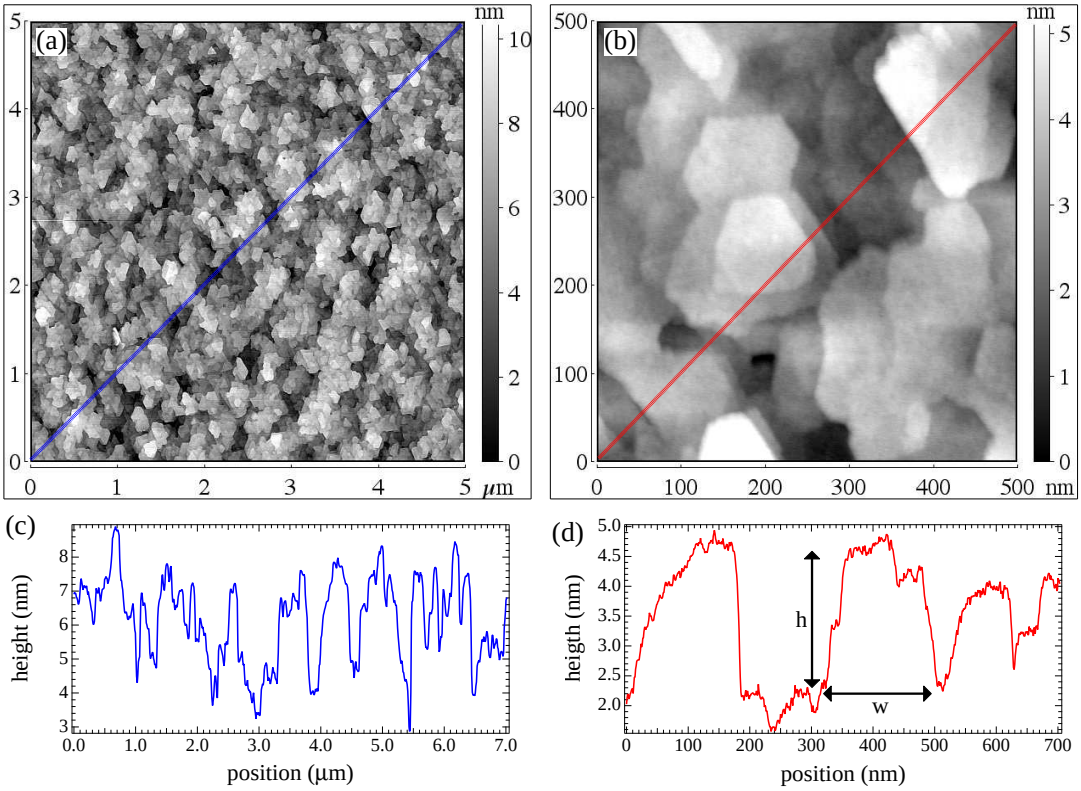

Figure 4.5: *AFM scans of a 12 nm thick Fe_3O_4/ZnO film surface (sample no. 4). (a) 25 μm^2 area. (b) 0.25 μm^2 area. The rms surface roughness of the shown area is 1.08 nm. (c) and (d) show line profiles marked in AFM scans. Image analysis was done using the software Image SXM [131].*

existence of islands with mostly hexagonal shapes and hence cannot definitively rule out or confirm this mechanism.

The occurrence of two domains, however, is likely since they only differ in the stacking sequence of their O planes. This different stacking sequence has only a minor effect on the interface energy and therefore on the nucleation probability of growing layers. Thus, both rotational variants should in principle be present in equal amounts. This rotational twinning has also been found for Fe_3O_4 growth on Pt and α-Al_2O_3 [132, 133] and many other systems with fcc-type lattices. In Sec. 4.3 the boundaries between these twins are investigated by transmission electron microscopy (TEM).

XRD and TEM results (see Sec. 4.3 and 4.2.3) indicate that films which are more than 40 nm thick have quite smooth surfaces suggesting that the islands are ultimately coalesced at large film thicknesses. The critical film thickness of island coalescence is known to be dependent on the growth temperature being higher for increased temperature [132]. The films investigated by XRD and TEM were grown in the MBE chamber in Würzburg and at slightly lower temperature of about 400°C compared to films investi-

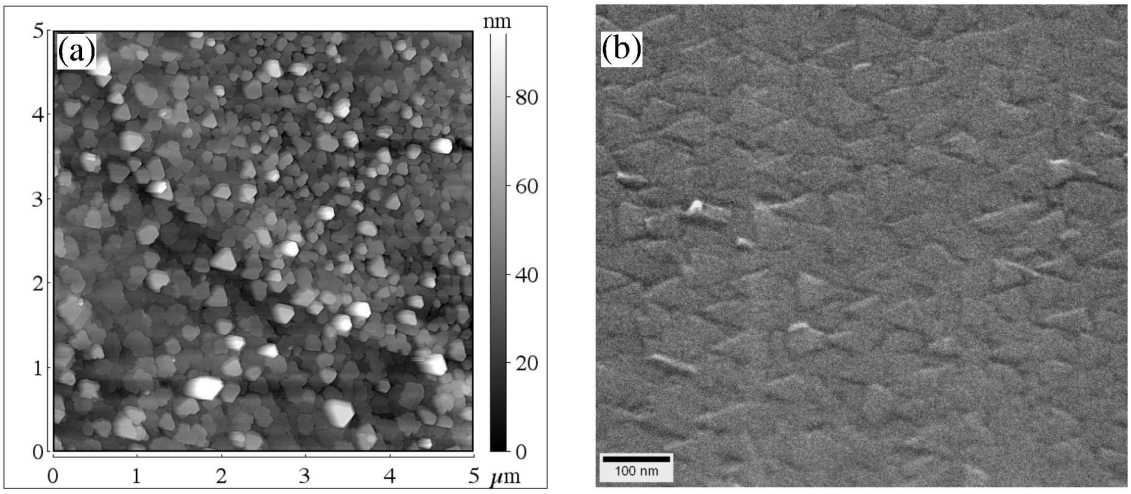

Figure 4.6: *(a) AFM image of a 25 nm thick Fe_3O_4/ZnO film surface (sample no. 5) with a 25 μm^2 scan area. Image analysis was done using the software Image SXM [131]. (b) Tilted-view SEM image of a 62 nm thick Fe_3O_4/ZnO film surface (sample no. 6). Two variants of triangular islands which are related to each other by a 180° in-plane rotation are demonstrated.*

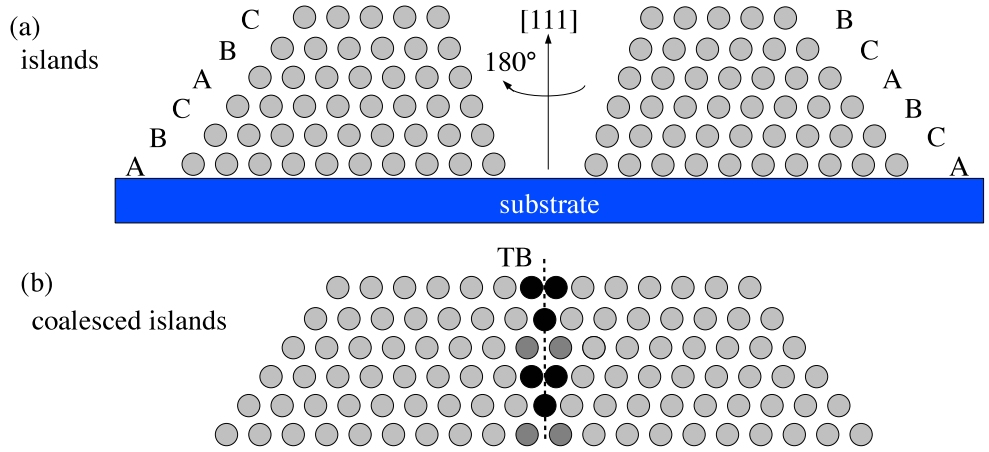

Figure 4.7: *Sketch of rotational twinning in an fcc-based structure. (a) Two islands which are rotational variants of each other form on the substrate. The islands exhibit an inverted fcc stacking sequence and can be converted into each other by rotation about 180°. Adopted from [133]. (b) Formation of a twin boundary due to coalescence of the two islands.*

gated by AFM, and probably therefore have smoother surfaces. The existence of mostly hexagonal island shapes for low and triangular shapes for high film thickness could be attributed to two different island edges which grow with different growth rates. This would ultimately lead to the disappearance of the fast growing island edges and result in triangular island possessing only the more slowly growing edges.

4.2.3 Characterization by x-ray reflectivity and diffraction

While electron diffraction on the surface of a growing film, which was demonstrated in Sec. 4.2.1, allows to determine the structural quality and lattice constant of the surface, x-ray diffraction with Cu-K_{α_1} radiation ($\lambda = 1.541\,\text{Å}$) is more suited to probe the overall 'volume' of a thin film and facilitates a very precise measurement of both the in-plane and out-of-plane lattice constant. The disadvantage of x-ray techniques is that a minimum film thickness of about 20 nm is required for a reasonable signal to noise ratio of the detected intensity. For this reason, the following section deals with x-ray diffraction and reflectivity of two sufficiently thick samples. All shown data about structure and strain state of Fe_3O_4/ZnO films refer to such thicker samples and do not necessarily describe the state of very thin samples. However, all ZnO-based samples quoted in this thesis have thicknesses larger than the theoretical thickness for lattice relaxation (see Tab. 3.2) and thus should be fairly comparable.

First, specular x-ray reflectivity (XRR) measurements on Fe_3O_4/ZnO films are presented. Details of the XRR technique can be found in Refs. [134, 135]. In a few words, XRR is based on the reflection of radiation at the surface and at the interface of a film/substrate structure for very low incidence angles (with respect to the surface) corresponding to small scattering vectors. According to the Fresnel-laws of optics the reflectivity of the specular radiation decreases with a very steep slope upon increase of the incidence angle. Additionally, the interference of waves reflected at surface and interface gives rise to an oscillatory intensity modulation with a period inversely proportional to the film thickness t [135]:

$$t = \frac{\lambda(m-n)}{2(\sin\theta_m - \sin\theta_n)}, \tag{4.1}$$

where m and n are the indices of the oscillation maxima at the angle positions θ_m and θ_n. Slope of the intensity decrease and damping of the the oscillation amplitude are primarily related to the surface and interface roughness, respectively. The connection between these factors, however, is complex so that it is necessary to simulate the reflectivity curve in order to extract the mentioned parameters. The here shown curves were simulated with the software "ReMagX" developed at the Max Planck Institute for Metals Research [136]. Tabulated data of the index of refraction of Fe_3O_4 and ZnO were used as fixed input parameters for the simulation [106]. Thickness, surface roughness, and interface roughness are fit parameters which were varied in order to optimize the simulated curves. Figure 4.8 shows the reflected intensity together with simulated curves

and model parameters as a function of the specular scattering vector $q_z = (2\pi/\lambda)\sin\theta$. The displayed experimental curves were corrected for low illumination of the sample at small incidence angle θ. At scattering vectors below the critical vector of external reflection, q_{crit}, the x-rays are totally reflected and the intensity is nearly constant for small q_z. For increasing scattering vector a large drop of the intensity occurs which is due to the Fresnel reflectivity $R = (2q_z/q_{crit})^{-4}$. Therefore, it is necessary to measure the intensity over several orders of magnitude to detect a sufficient number of oscillations.

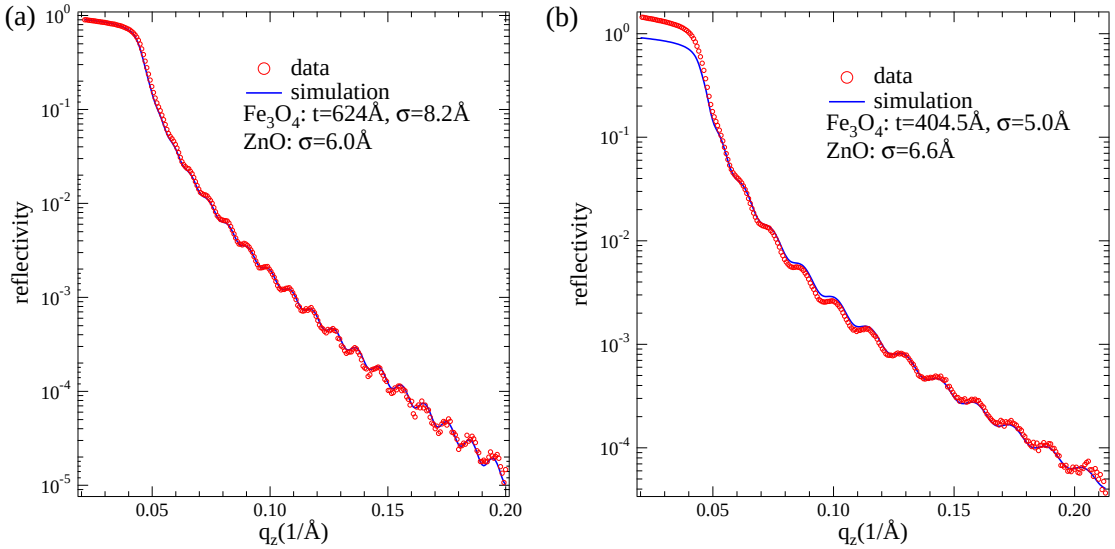

Figure 4.8: *XRR scans of Fe_3O_4/ZnO films. (a) Sample no. 6. (b) Sample no. 7. The experimental data were simulated with the software "ReMagX" [136] in order to obtain the indicated fit parameters film thickness t, surface roughness $\sigma_{Fe_3O_4}$, and interface roughness σ_{ZnO}.*

The surface roughness of the two samples obtained from the fits is markedly smaller than the values obtained from the AFM measurements. Since the roughness determined by both methods is based on very different probing methods, the observed discrepancy is not surprising. As already discussed in Sec. 4.2.2, a true sample-related difference in the surface roughness can be attributed to the lower growth temperature and larger film thickness of the samples investigated by XRR. The coalescence of the growing islands effects a strong reduction of the surface roughness. In contrast, the surface roughness of ZnO (interface roughness) is solely related to the pre-growth treatment of the substrates and should be very similar for all samples.

Note that the optical properties of different iron oxides are very similar in the x-ray regime. Therefore, an additional FeO interface layer or Fe_2O_3 surface layer would produce only tiny differences in the present, off-resonant reflectivity curves. The introduction of such layers into the simulation of the reflectivity did not improve the result significantly so that XRR cannot give a definite answer wheter such layers are present.

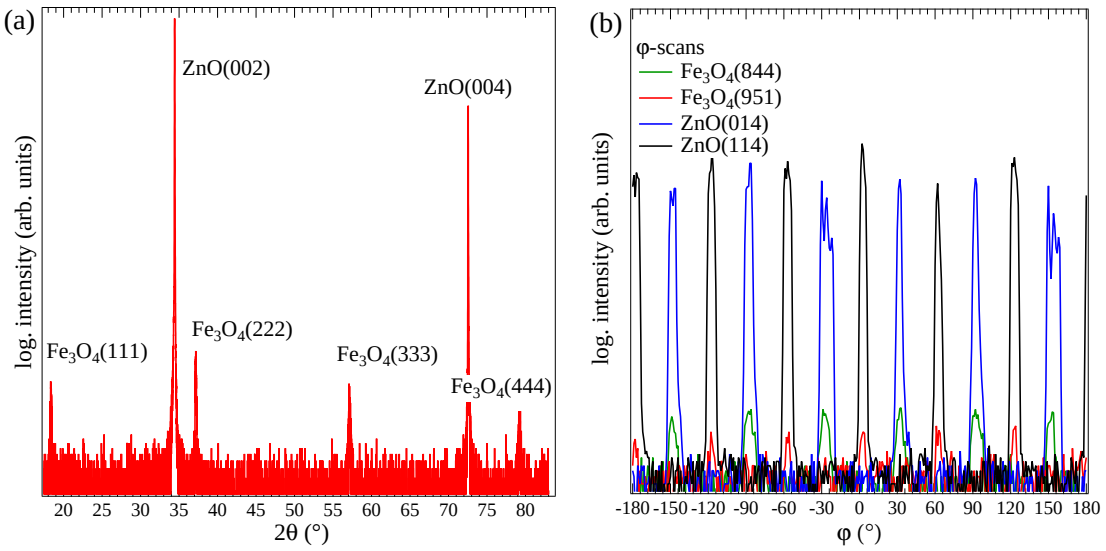

Figure 4.9: *XRD characterization of a 62 nm thick Fe_3O_4/ZnO film (sample no. 6). (a) Symmetric survey scan of out-of-plane peaks. (b) φ-scan of peaks with additional in-plane character indicating monocrystalline epitaxy.*

The XRD ω-2θ survey scan of a 62 nm thick film in Fig. 4.9(a) shows that only {111} planes are present parallel to the film plane of the Fe_3O_4/ZnO(001) structure, since only crystal planes normal to the sample surface contribute to diffraction in a symmetrical scan. This is a necessary but not a sufficient condition for monocrystalline epitaxy. If the film were polycrystalline, it would be textured along the {111} planes, though. However, φ-scans of Fe_3O_4(844) and (951) together with ZnO(014) and (114) reflections corroborate the monocrystalline nature of the films, since peak maxima are only observed for well-defined angles. In the case of a textured film with random in-plane orientation of the crystallites the intensity would be smeared out over a certain range of φ in such scans. Significant rotational in-plane mismatch—also called lattice twist—can be excluded as in-plane film and substrate peaks appear at identical angles φ. It can further be concluded that the in-plane epitaxial relationship $Fe_3O_4[2\bar{1}\bar{1}]$ ||ZnO[100] and $Fe_3O_4[1\bar{1}0]$ ||ZnO[110] is valid[1]. This is the same epitaxial relationship as found by Nielsen *et al.* for Fe_3O_4/ZnO films grown by pulsed laser deposition (PLD) [137]. They suggested that the parallelism of these close-packed directions is the reason for epitaxial growth of Fe_3O_4 on ZnO and on Al_2O_3 despite the large lattice mismatch.

The determination of the 2θ value of these {111} peaks yields the precise out-of-plane lattice constant of the film material. As can be inferred from Tab. 4.1 the macro strain in out-of-plane direction, $\epsilon_\perp$, is about $-0.32\,\%$, i.e., the out-of-plane lattice parameter

[1]Note that according to the definition of crystallographic directions in crystals with hexagonal symmetry the direction [100] is equivalent to $[\bar{1}10]$, i.e., they can be converted into each other through rotation by a multiple of 60°. Cf. Ref. [119].

is only marginally reduced compared to the bulk value of magnetite. This very small macro strain indicates that the atomic structure is almost completely relaxed. Moreover, the vertical coherence length, L_c, is accessible by measuring the linewidth, $\Delta(2\theta)$, and calculating the shape factor $L_c = 0.9\lambda/(\Delta(2\theta)\cos\theta_{peak})$ [138]. For a typical linewidth of 0.3° the inferred coherence length is comparable to or even larger than the film thickness, indicating the absence of a sub-grain structure in out-of-plane direction.

Since the linewidth is obviously not caused by the size of crystallites, it can be taken as a measure for the amount of micro strain present in the samples. With $\Delta(2\theta) = -2\tan\theta \cdot \Delta d/d$ [138] the variation in Bragg plane spacing, $\Delta d/d$, is in the range from 0.1 to 3.1 % for the linewidths given in Tab. 4.1.

The rocking curve of the Fe_3O_4(222) reflection shown in Fig. 4.10(b) exhibits a line broadening of $\Delta\omega = 0.23°$ (FWHM). Rocking curves of the symmetric and asymmetric peaks typically have a FWHM ranging from $\Delta\omega = 0.18$ to 0.56° (see Tab. 4.1). The rocking curve width is a measure for the distribution of tilted mosaic grains in the sample (mosaic spread). The mechanism mainly responsible for the broadening along ω is diffuse scattering due to micro strains located at defects such as dislocations or APBs [139, 140]. The dislocation density can be estimated according to a simple model from Gay *et al.* [141] using the following formula: $D_{dis} \approx \Delta\omega^2_{strain}/9b^2$. Taking into account a Burgers vector of 5.96 Å and assuming that the broadening $\Delta\omega$ is dominated by the strain contribution $\Delta\omega_{strain}$ and is exclusively caused by dislocations, the dislocation density is in the range from $4 \cdot 10^8\,\mathrm{cm}^{-2}$ to $3 \cdot 10^9\,\mathrm{cm}^{-2}$. For comparison, dislocation densities in chemical vapor deposition grown Si of high quality range from 10^3 to $10^8\,\mathrm{cm}^{-2}$ [142]. The broadening of film peaks in both symmetric and asymmetric scans indicates the presence of screw as well as edge dislocations in the film [143].

Compared to the rocking curve width of 0.5° obtained on an Fe_3O_4 single crystal grown by the floating zone technique, the mosaic spread in the shown epitaxial film is of the same size or slightly smaller. The rocking curve width is also similar to the one for a system with comparable lattice mismatch of 7.8 %, namely MgO on $SrTiO_3$-buffered Si, which is $\Delta\omega = 0.3°$ [81]. However, it is different than in PLD-grown Fe_3O_4/ZnO films, which show a FWHM of 0.04° for out-of-plane peaks and 0.9° for an in-plane peak [137]. There, the mosaic spread in out-of-plane direction is significantly smaller, whereas the in-plane mosaic spread is larger.

Measurements of asymmetric reflections give additional information on the structure since both in-plane and out-of-plane lattice vector components can be inferred from the position of a single reflection. The reciprocal space map shown in Fig. 4.10(a) is a two-dimensional projection of the Fe_3O_4(844) Bragg peak onto a plane with the in-plane coordinate $q_\parallel$ and the out-of-plane coordinate $q_\perp$. From the average of six (844) peaks, measured at different φ, the in-plane and out-of-plane macro strains are calculated to be $+0.60 \pm 0.06$ % and -0.05 ± 0.02 %, respectively (see last two lines of Tab. 4.1). This in-plane macro strain is in accordance with the one inferred from LEED measurements, which is $\epsilon_\parallel = +0.4 \pm 0.2$ %. The out-of-plane macro strain, $\epsilon_\perp$, is smaller than the one obtained from symmetric scans. However, care has to be taken as the absolute values of

Table 4.1: *XRD results obtained on a 62 nm thick Fe_3O_4/ZnO film (sample no. 6). Macro strain in out-of-plane ($\epsilon_\perp$) and in-plane direction ($\epsilon_\parallel$). FWHM of rocking curves and 2θ-scans.*

reflection	$\epsilon_\perp$ (%)	$\epsilon_\parallel$ (%)	$\Delta\omega$ (°)	$\Delta(2\theta)$ (°)
111	−0.35	—	0.56	0.16
222	−0.30	—	0.23	0.16
333	−0.32	—	0.33	0.28
444	−0.31	—	0.32	0.30
844	−0.04	0.6	0.18	0.75
951	−0.05	0.6	0.33	0.44

scattering vectors of asymmetric scans can be misleading if tilt or curvature is present in the film [144]. For this reason, the value inferred from symmetric scans, i.e., on average −0.32 %, seems to be more reliable.

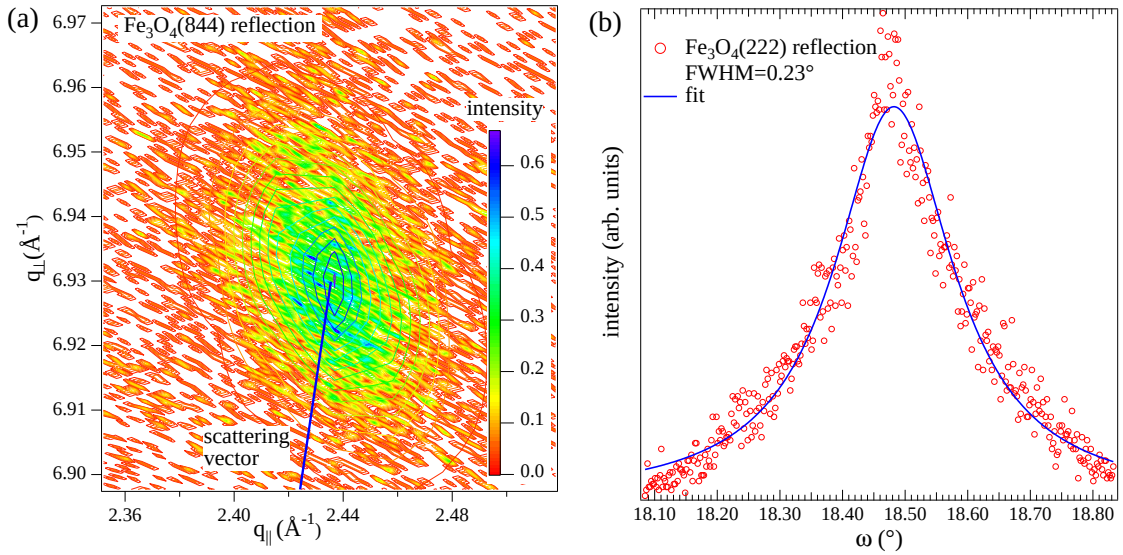

Figure 4.10: *XRD characterization of a 62 nm thick Fe_3O_4/ZnO film (sample no. 6). (a) Reciprocal space map of the asymmetric Fe_3O_4(844) reflection. The direction of the scattering vector is indicated. (b) Rocking curve scan of the symmetric Fe_3O_4(222) reflection.*

The broadening of asymmetric reflections (see Fig. 4.10(a)) is mainly along the scattering vector, i.e., along 2θ, and stems from variations of the lattice constant due to compositional gradients or micro strain present in the film volume as discussed above [145]. On the contrary, broadening along ω is due to wafer curvature or dislocation-induced tilt or twist of mosaic blocks [146]. As has been explained, the twist is small. Furthermore, the tilt was estimated from ω-2θ-scans of film and substrate peaks at four polar angles φ to be of the order of a few arcseconds only [147]. The exact shape of the reflection, which is only suggested by the orientation of the elliptical Gaussian fit

in Fig. 4.10(a), depends on the lateral coherence length, i.e., crystallite or mosaic block size and tilt angle of the mosaics, and can only be reconciled by scattering simulations [139], which goes beyond the scope of the present study.

In summary, XRD demonstrates that the film is almost completely relaxed, particularly with regard to the large lattice mismatch to ZnO. Strictly speaking, the lattice is rhombohedrally distorted and not cubic anymore. Experimentally determined broadenings of Bragg reflections were discussed in detail. Possible relaxation mechanisms are dislocations and APBs.

4.3 Microstructure

In the following, the investigation of the microstructure of a thick Fe_3O_4/ZnO film (sample no. 6) is presented[1]. Figures 4.11(a) and (b) show a transmission electron microscope (TEM) micrograph and the corresponding electron diffraction pattern of the Fe_3O_4/ZnO structure, respectively. The ZnO substrate, two structural domains of Fe_3O_4, and the Pt capping layer can be distinguished in the TEM image. It can be clearly seen that two domains with different orientation (see lines in Fig. 4.11(a)) exist in the analyzed part of the Fe_3O_4 film. The domain boundary, which is visible in the central part of the image, has an extent of some nanometers. The changing width of the domain boundary could be solely due to a varying thickness of the TEM lamella perpendicular to the interface.

The diffraction pattern in Fig. 4.11(b) is composed of a ring-like structure resulting from diffraction at the Pt capping layer and diffraction spots, which are lined up in form of rows running along the Fe_3O_4[111] direction. The parallelism of the spot rows corresponding to the ZnO lattice (brighter spots) and those resulting from the Fe_3O_4 lattice (less intense spots with a larger spot density) demonstrates that the $Fe_3O_4(111)$ plane is parallel to the ZnO$(00\bar{1})$ plane without measurable tilt in accordance with the XRD results. This is in line with the fact that the O sublattices of Fe_3O_4 and ZnO are aligned across the interface.

The separation of the rows in $Fe_3O_4[11\bar{2}]$ direction corresponds to the in-plane lattice constants, i.e., 3.25 Å for ZnO and 5.94 Å for relaxed Fe_3O_4. The separation of every third spot within single rows along Fe_3O_4 [111], corresponds to the repeat unit length of 4.84 Å along this direction. Both in-plane and out-of-plane lattice constants derived from the electron diffraction pattern are equal to the relaxed lattice constant of magnetite within ±0.05 Å. The two additional spots along the [111] direction are a consequence of the superposition of the diffraction patterns from two differently oriented domains and double diffraction events. Both domains are present in approximately equal portions giving rise to similar diffraction intensities.

[1] The scanning transmission electron microscopy (STEM) and electron diffraction measurements were performed by Dr. M. Kamp at the Chair for Applied Physics of the University of Würzburg.

The atomic structure of two such domains is displayed in the scanning transmission electron microscopy (STEM) images of Fig. 4.12. As the STEM signal in high-angle annular dark field (HAADF) scales with the atomic number ($\approx Z^2$) STEM depicts the position of Fe and Zn cations, but does not detect O atoms. On first glance the imaged Fe lattice resembles a honeycomb pattern with additional protrusions in the middle of each comb. The hexagons are, however, asymmetric and are differently oriented in both domains. An atomic model of Fe positions together with respective crystal directions is indicated in Fig. 4.12(a).

Convergent beam electron diffraction (CBED) patterns which correspond to the STEM images are shown as insets in Fig. 4.12. Both patterns are related to each other by a rotation of 180° about the vertical axis, i.e., the [111] direction. This is equivalent to inverting the direction of the incoming electron beam from Fe_3O_4 $[1\bar{1}0]$ to $[\bar{1}10]$. This in-plane rotation by 180° was also observed as rotated trigonal islands in the AFM and SEM images of Fig. 4.6. It is a result of rotational twinning between several out of all islands similar to the $Fe_3O_4(111)/Pt(111)$ structure [18, 148]. The two twinned domains exhibit a different stacking sequence along [111], i.e., (ABC) and (CBA). When those islands finally coalesce at a later growth stage, they form a twin boundary (TB). Across the TB every third fcc layer (here labeled A) is coherent, but the layers B and C are interchanged according to the simple atomic model in Fig. 4.7. Thus, the formed boundary should be considered as incoherent. The boundary area between twinned variants is not necessarily a high symmetry plane as can be seen in the the TEM micrograph of Fig. 4.11(a).

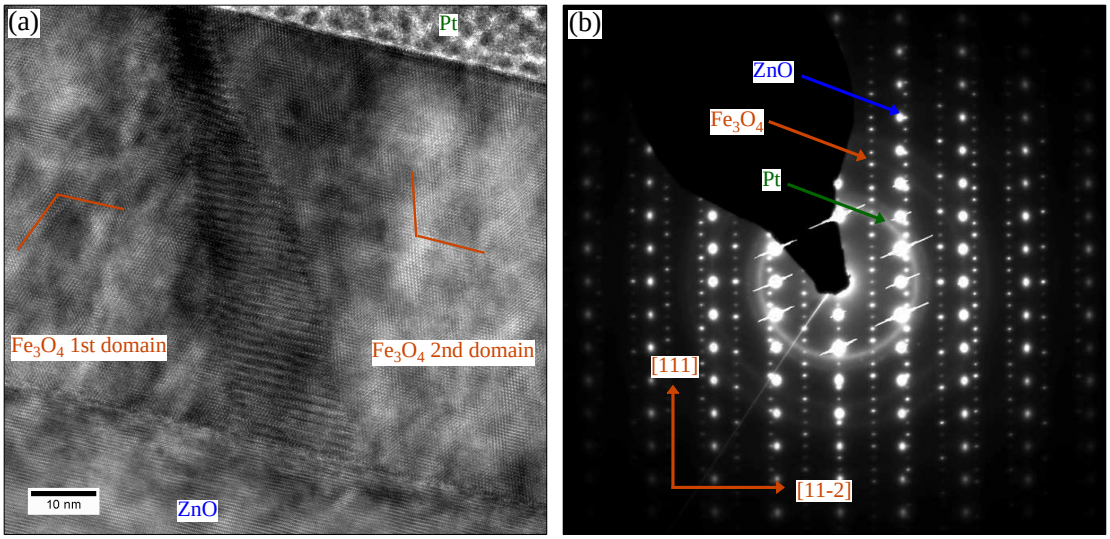

Figure 4.11: *TEM image and diffraction pattern of Fe_3O_4/ZnO (sample no. 6). (a) TEM image. (b) Corresponding electron diffraction pattern observed from $Fe_3O_4[1\bar{1}0]$. The x and y axes point along $Fe_3O_4[11\bar{2}]$ and $Fe_3O_4[111]$, respectively.*

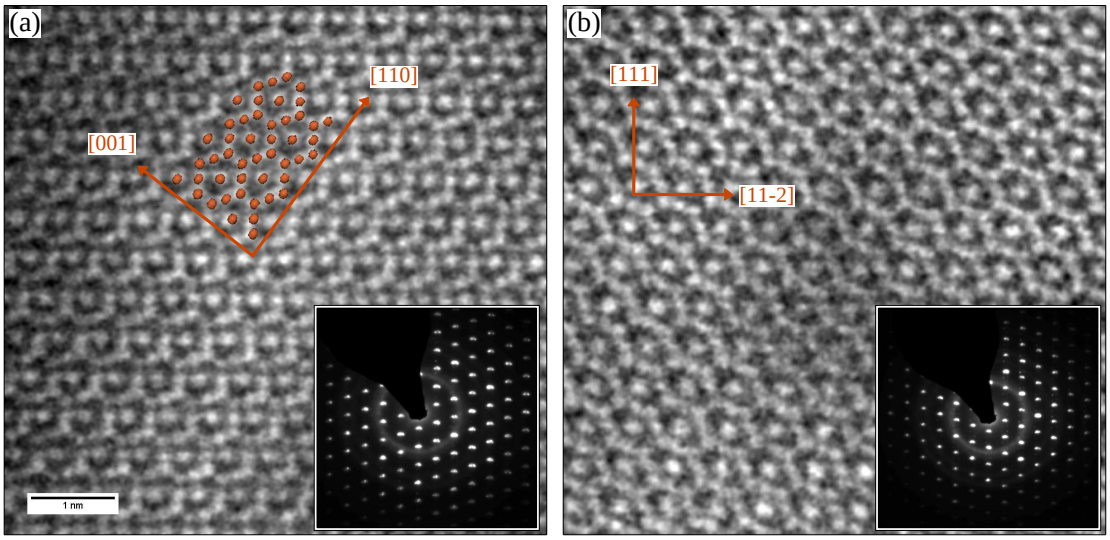

Figure 4.12: *STEM images and electron diffraction patterns of two Fe_3O_4 domains on ZnO (sample no. 6). The indicated crystal directions are valid for both domains. (a) First domain with electron beam along $Fe_3O_4[1\bar{1}0]$. The Fe sublattice is shown as orange dots. (b) Second domain with electron beam along $Fe_3O_4[\bar{1}10]$.*

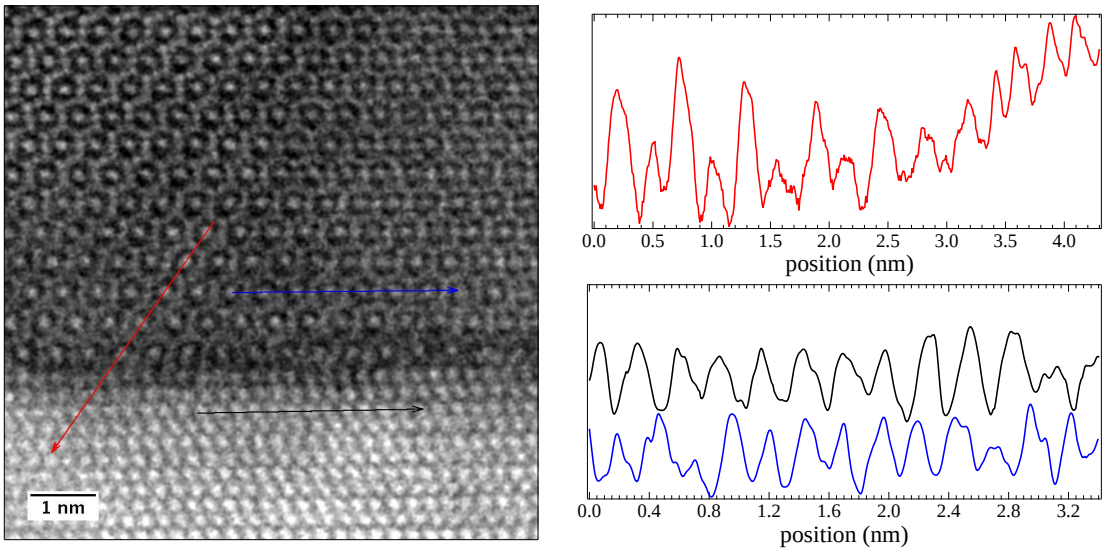

Figure 4.13: *Cross-sectional STEM analysis from Fe_3O_4 $[1\bar{1}0]$. (a) STEM image of Fe_3O_4/ZnO interface (sample no. 6). (b) Profile of HAADF signal along red arrow, i.e., along Fe_3O_4 $[\bar{1}\bar{1}0]$ across the interface. (c) Profiles along blue and black arrow, i.e., inside Fe_3O_4 and inside ZnO along a direction parallel to the interface, viz., Fe_3O_4 $[11\bar{2}]$.*

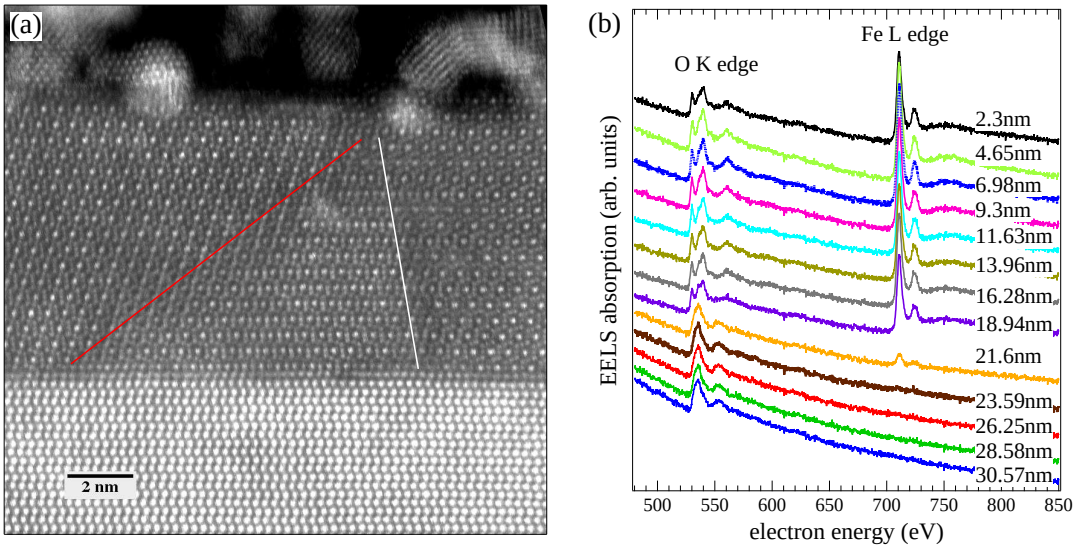

Figure 4.14: *Cross-sectional STEM image from Fe_3O_4 [1$\bar{1}$0]. (a) STEM image of an Fe_3O_4/ZnO thin film (sample no. 8). The position of a TB and an APB is marked by a white and red line, respectively. (b) EELS spectra taken at different positions across the interface.*

Figure 4.13(a) shows a STEM image of the Fe_3O_4/ZnO interface with the incoming electron beam along Fe_3O_4 [1$\bar{1}$0]. The Zn lattice clearly exhibits the hexagonal AB-stacking sequence. Parts of STEM image are slightly distorted, which is due to drift during the scanning process of the electron beam. On a small scale of a few nanometers, both lattices are highly ordered without obvious defects. The interface-near (about 1 nm) layers of Fe_3O_4 display a slightly different contrast than the 'bulk' of the film. The ZnO surface is fairly flat. However, the Fe atoms making up the edges of the honeycomb lattice appear not so well resolved in the interfacial region. In contrast, Fe atoms with octahedral environment are clearly resolved so that the atomic structure locally resembles to wüstite. As is displayed in the line-profile in Fig. 4.13(b) there is clearly periodic atomic contrast across the interface. It has to be kept in mind that intensity variations at the interface can be caused by step edges along the electron beam direction, and thus the HAADF contrast of the interface region appears to be different, although the interface is sharp on a single terrace. Another possibility is that atomic diffusion across the interface takes place, which blurs the HAADF contrast at the interface.

In a STEM and electron energy-loss spectroscopy (EELS) investigation[2] of a 14 nm thick film (sample no. 8), an Fe_3O_4 domain which is bounded by an APB and a TB was identified (see Fig. 4.14(a)). The white line indicates the position of the TB where the orientation of the Fe sublattice changes by the in-plane rotation about 180° as explained

[2]The STEM and EELS measurements were performed in the group of Dr. Jo Verbeeck at the Institute for Electron Microscopy for Materials Research of the University of Antwerp.

above. The red line marks the position of the APB where the Fe sublattice shifts by $^1/_4\,[110]$, i.e., 2.97 Å, across the APB. The shift vector lies in the boundary plane (110). This is the same APB shift vector as found for epitaxy of magnetite on MgO, by e.g. Hibma *et al.* [43]. For this particular domain the APB and TB pass over into each other, i.e. they form a microstructural network. Such microstructural network of boundaries are for example known for $La_{2-x}(Sr,Ba)_xCuO_4$ [149].

For the same sample a line profile of the EELS absorption across the interface was generated (see Fig. 4.14(b)). The intensity of the Fe L-edge absorption alters abruptly when going from the position of ZnO to the one of magnetite. Also the O K-edge is changing significantly for different positions of the electron beam. This can be seen by the occurrence of the characteristic pre-edge peak at about 530 eV in Fe_3O_4 (position 2.3 to 18.94 nm) which is not present for spectra of the ZnO region (positions 23.59 to 30.57 nm). One single spectrum at the position of 21.6 nm (at the very interface) is a superposition of the ZnO spectrum with small amounts of Fe. These spatially resolved EELS data confirm that the interface is chemically sharp and that interfacial reactions do not occur.

Figure 4.15 displays the Fe_3O_4 lattice in a cross section from the $Fe_3O_4[11\bar{2}]$ direction. Image (a) shows an atomic structure consisting of horizontal lines where an Fe_{oct} layer and a mixed Fe_{tet}-Fe_{oct}-Fe_{tet} layer alternate in [111] direction. The inset shows the positions of the Fe atoms (orange). Layers consisting of solely Fe_{oct} appear brighter since their atomic density is larger along the $Fe_3O_4[11\bar{2}]$ direction.

Part (b) illustrates an APB which runs in vertical direction in the central part of the image and exhibits lower HAADF intensity. As is indicated by the yellow line the Fe sublattice shift by $^1/_2\,[111]$ when crossing this boundary. However, it cannot be ruled out that there is an additional component of the phase shift vector along the electron-beam direction $[2\bar{1}\bar{1}]$. The atomic arrangement is sketched in Fig. 4.16, which illustrates how the nucleation of two islands with a different initial Fe layer brings about the formation of an APB for coalesced islands. The APB can be considered as a stacking fault of the Fe sublattice.

Most of APBs imaged in $Fe_3O_4\,[11\bar{2}]$ direction were found to be aligned perpendicular to the interface such as the one in Fig. 4.15(b). Therefore, these detected APBs lie in or close to the $\{1\bar{1}0\}$ family of planes. Both, APBs running continuously from the interface to the surface of the film, and APBs ending inside the film were observed. The latter have to be bound by a partial dislocation at their ending line [150].

Finally, it has to be addressed, whether the phase shift vector of $^1/_2\,[111]$ observed from the $Fe_3O_4\,[11\bar{2}]$ direction is in accordance with earlier observations of APBs in magnetite. As Hibma *et al.* [43] have pointed out neighboring APD in Fe_3O_4 are related by a phase shift out of the $^1/_2\langle 100\rangle$ or $^1/_4\langle 110\rangle$ family of vectors or a combination thereof. The here observed phase shift component is not equal to the projection of $^1/_2\langle 100\rangle$ or $^1/_4\langle 110\rangle$ onto the [111] direction, viz. $^1/_6\,[111]$. However, it is identical to the sum of the three phase shift vectors $^1/_4\,[110]$, $^1/_4\,[101]$ and $^1/_4\,[011]$. For this reason, the here obtained results could be APBs which actually belong to the same type of APBs as

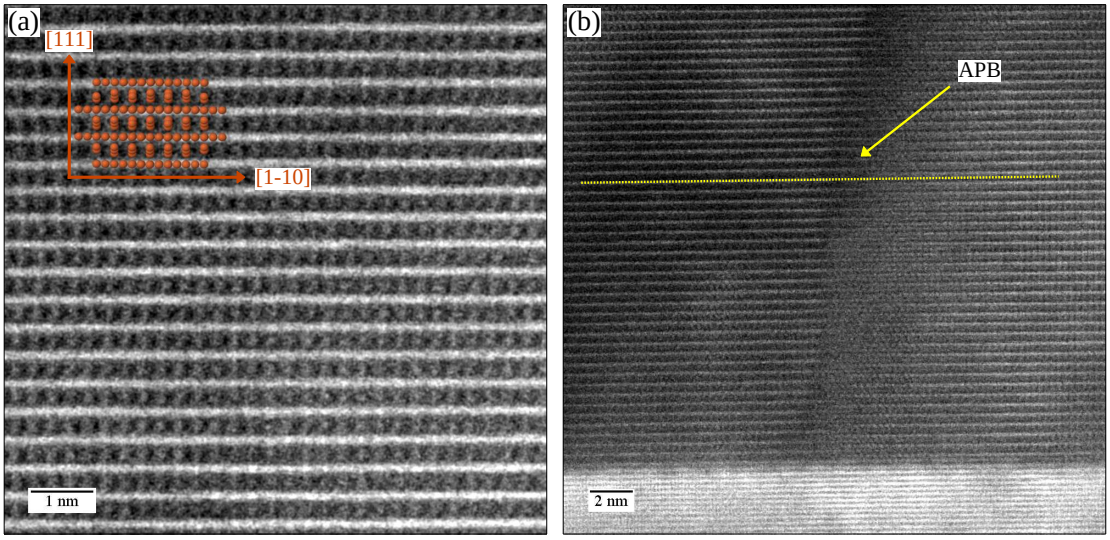

Figure 4.15: *Cross-sectional STEM images from Fe_3O_4 [11$\bar{2}$] (sample no. 6). (a) High-magnification STEM image of Fe_3O_4 film lattice. The atomic model of the Fe lattice indicates that horizontal closed lines correspond to the Fe_{oct} layer and vertical lines to the mixed Fe_{tet}-Fe_{oct}-Fe_{tet} layer. Crystal directions are indicated. (b) Lower magnification STEM image of the Fe_3O_4/ZnO interface and film with an APB running in vertical direction. The dashed yellow line is a guide to the eye, exemplifying that the Fe sublattice shifts by $^1/_2$[111], i.e., 2.42 Å, across the APB.*

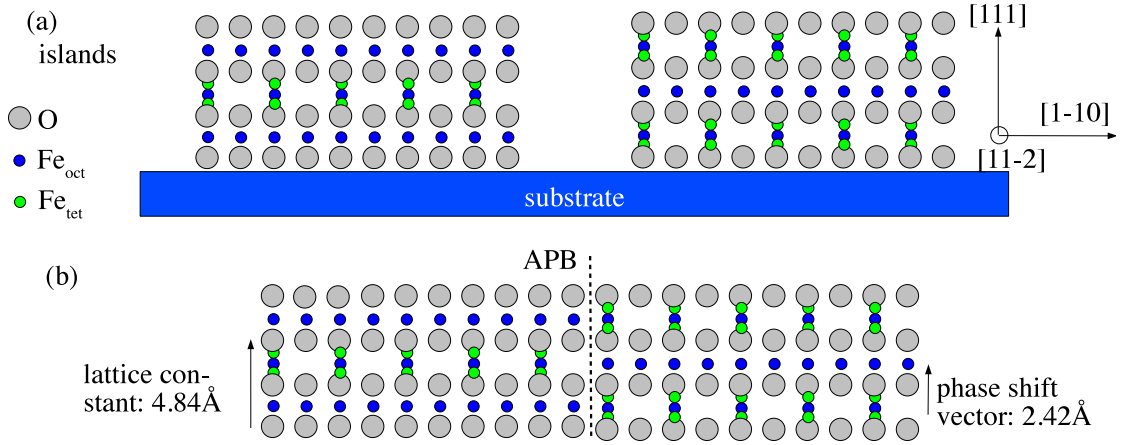

Figure 4.16: *Sketch of the atomic arrangement at an APB as observed from Fe_3O_4 [11$\bar{2}$]. (a) Nucleation of islands with different initial Fe layer. (b) Formation of an APB upon coalescence of the islands.*

already found in (001)-oriented films (cf. e.g. Refs. [42–44]). It can be speculated that the observed phase vector is dictated by steps of the ZnO surface due to the necessity to have a continuous O sublattice across the interface. In contrast, a phase shift of 1.86 Å along [111] was detected by Roddatis *et al.* for the system $Fe_3O_4(111)/Pt(111)$ [148]. Such a phase shift, however, implicates that the O sublattice is incoherent at the boundary.

Recapitulatory, the atomic structure of the grown film is highly ordered on a small scale as in Fig. 4.12, but shows large-scale defects, namely TBs or APBs. Both boundaries form at the site where growing islands coalesce. There are not enough data available to clarify if or how the occurrence of both defects is connected. Here, large-scale TEM observations from various directions would be very helpful. Presumably, the two phenomena—APB and TB formation—can be thought of as independent. This means that when two islands coalesce either no boundary, or a TB, or an APB, or both types of boundaries are formed. The resulting APB density or the according APD size could not exactly be determined by, e.g., dark-field imaging. However, one is able to note that the domain size ranges from about 15 nm (see Fig. 4.14) to more than 50 nm (see Fig. 4.11).

4.4 Electronic and chemical structure studied by (hard) x-ray photoelectron spectroscopy

The upcoming section deals with the chemical analysis of Fe_3O_4/ZnO films by means of PES. HAXPES measurements of an Fe_3O_4/ZnO film were performed using the HIKE endstation (high kinetic energy) at beamline KMC-1 at BESSY II in Berlin[3]. For details on the experimental setup Refs. [151, 152] can be consulted.

Figure 4.17(a) shows *ex situ* HAXPES Fe 2*p* spectra of a 21 nm thick Fe_3O_4/ZnO film (sample no. 9) grown with a constant Fe/O_2 flux ratio at 530°C. As already explained in Sec. 3.2.5, the overall lineshape of the three spectra and in particular the one taken with 3 keV is distinctive for magnetite. Both main peaks are broad and the binding-energy region between those is smooth and relatively structureless. However, the inset in Fig. 4.17(a) shows a small increase of the Fe^{2+} spectral weight (as a shoulder of the main peak and also for the CT satellite) with higher information depth of the spectra. This is interpreted as an Fe^{2+}-rich interface-near layer. It is believed that this interface layer is due to the growth procedure with a constant Fe/O_2 flux ratio. The formation of such an Fe^{2+}-rich interface-near layer can be hindered by modifying the growth procedure applying an effectively higher oxidation potential for the first growing layers. This can be accomplished by lowering the Fe/O_2 flux ratio by a factor of about two for the first few nanometers of growth [153, 154]. It is a clear evidence that the immediate proximity of the ZnO substrate enlarges the stability field of wüstite while narrowing the one for

[3]Measurements were performed by A. Müller and A. Ruff.

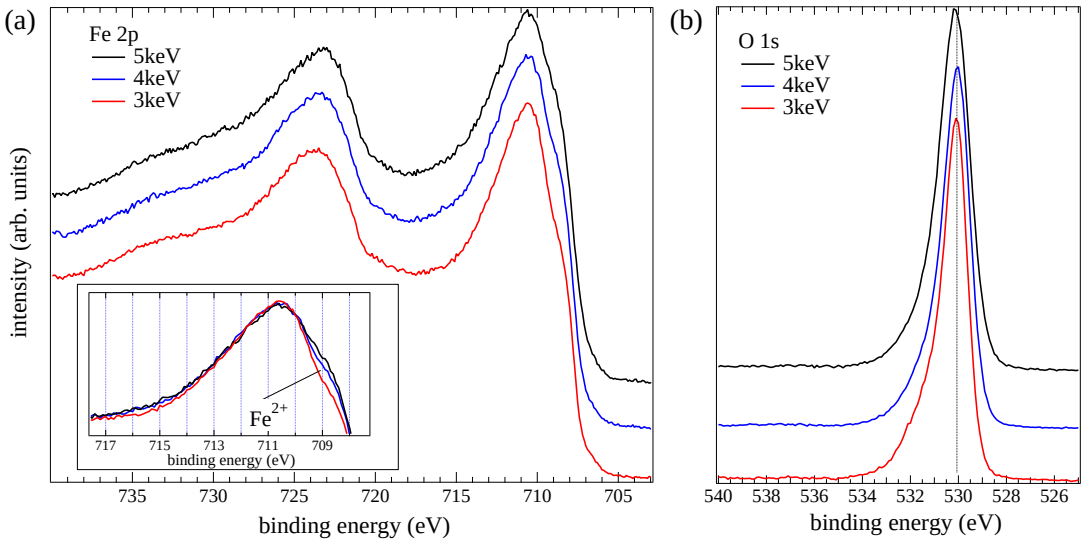

Figure 4.17: *(a) HAXPES Fe 2p spectra of a 21 nm thick Fe_3O_4/ZnO film (sample no. 9) at various photon energies. The Fe oxidation state points towards the presence of an Fe^{2+}-rich interface layer. (b) O 1s spectra taken under the same conditions.*

magnetite. This effect is caused by the lower interface energy of wüstite in contact with ZnO due to the closer lattice match.

Table 4.2: *Relative chemical composition (in %) inferred from spectral intensities of different core levels taken on an Fe_3O_4/ZnO film (sample no. 9). Corresponding spectra are shown in Figs. 4.17 and 4.18(a).*

$h\nu$, θ	O 1s		Fe 2p	Zn 2$p_{3/2}$	C 1s
	O^{2-}	OH^-			
5 keV, 5°	57.4	9.0	21.3	3.0	9.2
4 keV, 5°	54.6	10.8	21.6	2.4	10.6
3 keV, 5°	48.6	12.7	22.4	2.1	14.2

The formation of such interface layers with deviating stoichiometry *during* growth is a known phenomenon in literature, e.g., for Fe_3O_4/Pt [18], Fe_3O_4/α-Fe_2O_3 [99], or Co_3O_4/α-Fe_2O_3 [155] structures. Interestingly, the presence of such interface phases *after* growth was not confirmed in cross-sectional TEM studies of the former two sample systems [47, 148]. It is therefore conceivable that a growing film homogenizes during further growth due to diffusion processes. As our HAXPES results show, in the present case the off-stoichiometry exists even *after* film growth.

In summary, the HAXPES Fe 2p spectra give evidence that the stoichiometry of Fe_3O_4/ZnO films grown with a constant Fe/O_2 flux ratio is changing towards the inter-

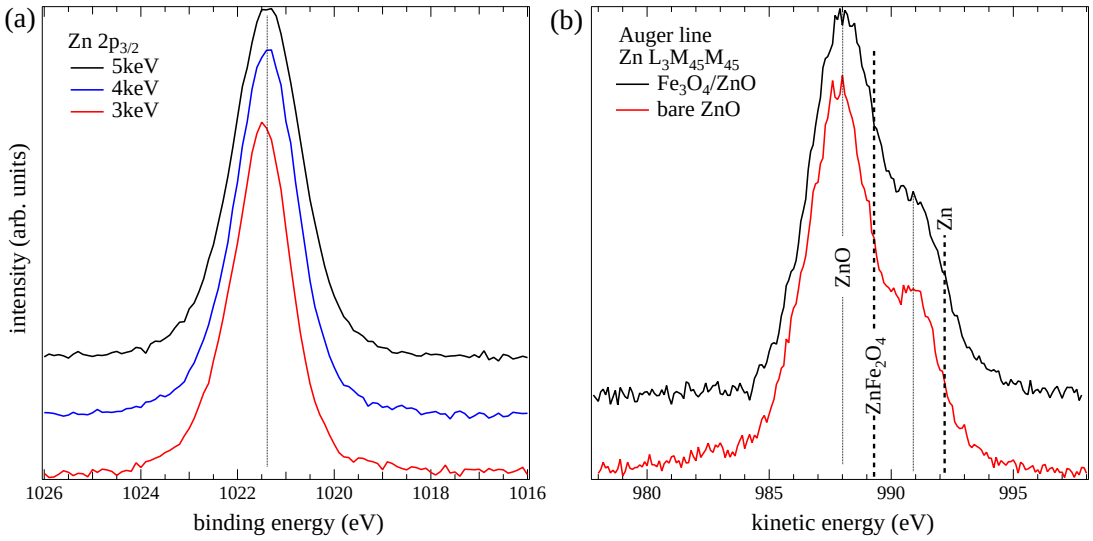

Figure 4.18: *(a) HAXPES Zn $2p_{3/2}$ spectra of a 21 nm thick Fe_3O_4/ZnO film (sample no. 9) at various photon energies. (b) Auger Zn $L_3M_{45}M_{45}$ XPS spectra of a 16 nm thick Fe_3O_4/ZnO film (sample no. 1) and a bare ZnO substrate. The typical chemical environment for Zn in ZnO is confirmed.*

face. Structural data and a discussion of the interface of fully stoichiometric magnetite grown by means of variation of the Fe/O_2 flux ratio during growth are given in Sec. 4.3.

O 1*s* spectra in Fig. 4.17(b) exhibit an asymmetric lineshape indicative of OH-groups residing at the surface. Together with the C 1*s* level they represent a measure of the contamination due to exposure to ambient conditions. The spectral weight of these OH-groups obviously declines with increasing information depth (see Tab. 4.2). The main-peak position is constantly at the expected binding energy of 530.1 eV. In the present case the energy of all spectra (Fe 2*p*, O 1*s*, and Zn $2p_{3/2}$) was calibrated by measuring the Au $4f_{7/2}$ core level of a gold foil in electrical contact with the sample. This again confirms the fact that the O 1*s* position can be taken to correct for charging effects (cf. Sec. 3.2.6).

Figure 4.18(a) shows Zn $2p_{3/2}$ spectra corresponding to spectra in Fig. 4.17. The common peak position for the three shown spectra is 1021.4 eV, which is in good agreement with the literature value given by Woell *at al.* taking into account their different energy calibration of the O 1*s* peak [125]. However, the Zn $2p_{3/2}$-peak position is generally not very sensitive to the chemical environment so that different components are difficult to distinguish. Metallic Zn exhibits a binding-energy shift of −0.3 or −0.4 eV [125, 156] and the spinel phase $ZnFe_2O_4$ a shift of −0.8 eV [156] relative to ZnO. Since the peak in Fig. 4.18(a) broadens for higher photon energies due to worse energy resolution, there remains some doubt on the assignment of the peak to a single, definite chemical environment. Therefore, the position of the Zn $L_3M_{45}M_{45}$ Auger line excited by Al-K_α radiation was measured additionally for several Fe_3O_4/ZnO films. This line

position is known to vary more strongly for different chemical environments [156]. The Zn $L_3M_{45}M_{45}$ Auger spectrum always consists of a pair of lines, i.e., a main line and a satellite, as indicated in Fig. 4.18(b) by the full vertical lines. The main line positions for elemental Zn and $ZnFe_2O_4$ are also indicated as dashed vertical lines in Fig. 4.18(b). Clearly, the spectrum taken on the thin film (black curve) coincides closely with the one of a bare ZnO substrate (red curve). Additionally, the main line position is in good agreement with the literature value of 988 eV. Both facts argue against a $ZnFe_2O_4$ phase. Moreover, the presence of a $ZnFe_2O_4$ phase should also enhance the Fe^{3+} signal in the Fe $2p$ spectrum in comparison to magnetite, since Fe^{2+} is replaced by Zn^{2+} upon the formation of $ZnFe_2O_4$. This is clearly not seen (cf. Fig. 4.17(a)).

Hence, it can be concluded that Zn is present in the chemical environments of ZnO. This is especially interesting because for the Fe/ZnO interface an interface reaction towards elemental Zn was found [157]. In contrast, the Fe_3O_4/ZnO is stable under the shown growth conditions, which is in agreement with the expectation from thermodynamic data (cf. Sec. 3.1.5).

The film thickness estimated from the Fe $2p$/Zn $2p_{3/2}$ intensity ratio (see Tab. 4.2) using Eq. (3.28) is 12 ± 2 nm. Therefore, it is considerably smaller than the film thickness inferred from the growth rate, which is 21 nm. This indicates that the growth was not perfectly two-dimensional and hence the substrate signal is not as strongly attenuated by the film as expected. A fraction of the Zn signal therefore stems from not-perfectly covered substrate areas. This behavior was generally observed for thicknesses up to about 30 nm indicating the island-like microstructure of the film. In contrast, XPS spectra of a very thick film (62 nm) did not show remaining Zn signal due to complete coalescence of islands.

We now turn to the stoichiometry analysis of an Fe_3O_4/ZnO sample which is shown in Fig. 4.19. The spectra were measured *in situ* immediately after sample growth and under identical conditions as the reference spectra displayed in Sec. 3.2.5. Two experimental spectra with exemplary values of the off-stoichiometry parameter δ are illustrated together with the corresponding fit result using reference spectra. The low intensity of the squared residual spectrum (smaller by about a factor of 5000) indicates the good correspondence between experimental data and the fit.

Results of the stoichiometry analysis of several Fe_3O_4/ZnO samples are additionally given in Tab. 4.3. XPS spectra were taken at two electron emission angles, $\theta = 30$ and 60°, corresponding to information depths of 14 and 8 Å. For comparison, the stoichiometry determined by fitting the XAS Fe L-edge spectra of the same samples with reference spectra is also listed (see Sec. 3.3.3 for reference spectra). Samples for which XPS was measured *in situ* were *ex situ* analyzed by XAS and vice versa. If comparing all values, it becomes clear that δ increases for larger surface sensitivity of the respective measurement. This implies that the 'bulk' of films of different thickness is stoichiometric and that the surface exhibits an off-stoichiometric layer of few ångströms thickness. It will be elucidated by the XCMD measurements presented in the following section how this surface layer affects the magnetic properties of the samples.

4.5 Magnetic properties

4.5.1 X-ray magnetic circular dichroism

Figure 4.20 shows representative XAS and XMCD spectra, taken on an Fe_3O_4/ZnO film. Spectra of various Fe_3O_4/ZnO samples show only marginal differences and mainly vary in the absolute signal of the XAS and XMCD effect, which finally results in somewhat different magnetization values obtained by means of a sum-rule analysis. The same applies for spectra measured under different angles of incidence *after* a successful application of the desaturation procedure (cf. Sec. 3.3.2). Moreover, the spectral characteristics are in good agreement to literature data [113, 116, 117] of magnetite single crystals and thin films (cf. red curve in Fig. 4.20(b)).

Table 4.3: *Results of a sum-rule analysis of 0° and 70° incidence XMCD spectra of Fe_3O_4/ZnO samples with different thickness and off-stoichiometry parameter δ. Measurements were taken in a field of $\mu_0 H = \pm 3\,T$ and at room temperature.*

sample no.		1	7	10	11	12
thickness		16 nm	40 nm	8 nm	4 nm	8 nm
XMCD performed		*ex situ*	*ex situ*	*ex situ*	*ex situ*	*in situ*
δ (λ_{XAS} = 18-25 Å)		0.03	0.03	0.038	—	0.026
δ (λ_{XPS} = 14 Å)		0.047	0.055	0.055	—	0.055
δ (λ_{XPS} = 8 Å)		0.073	0.11	0.092	—	0.11
0°	m^*_{spin} (μ_B/f.u.)	2.88	2.73	2.82	2.55	2.82
	m_{orb} (μ_B/f.u.)	0.06	0.06	0.03	0.03	-0.0072
	m_{orb}/m^*_{spin}	0.021	0.022	0.011	0.012	-0.0026
70°	m^*_{spin} (μ_B/f.u.)	3.10	2.82	2.85	2.61	2.91
	m_{orb} (μ_B/f.u.)	0.06	-0.010	0.03	0.06	0.09
	m_{orb}/m^*_{spin}	0.019	-0.0035	0.011	0.023	0.031

$\Delta\delta = 0.018$, $\Delta m_{spin} = 0.15\,\mu_B$/f.u., $\Delta m_{orb} = 0.06\,\mu_B$/f.u.

No spectral changes aside from a small increase of the XMCD effect were observed upon lowering the temperature below the Verwey-transition temperature. This is in accordance with XMCD measurements of single crystals [158], which were also performed with magnetic fields significantly larger than the technical saturation magnetization and for this reason are expected to show only a small paraprocess in the low-temperature phase (cf. Sec. 2.4). Moreover, the off-stoichiometry parameter δ of the surface layer probed by XAS is larger than its critical value below which a Verwey transition can in principle be observed.

Orbital and spin magnetic moments were extracted by a sum-rule analysis of the spectra. The respective values are given in Tab. 4.3. 'Saturation' moments (at $\mu_0 H = 3\,T$) for samples with various thicknesses range from 2.6 to 3.1 μ_B/f.u. Essentially, there is no systematic trend for the magnetic moment as a function of the film thickness. This

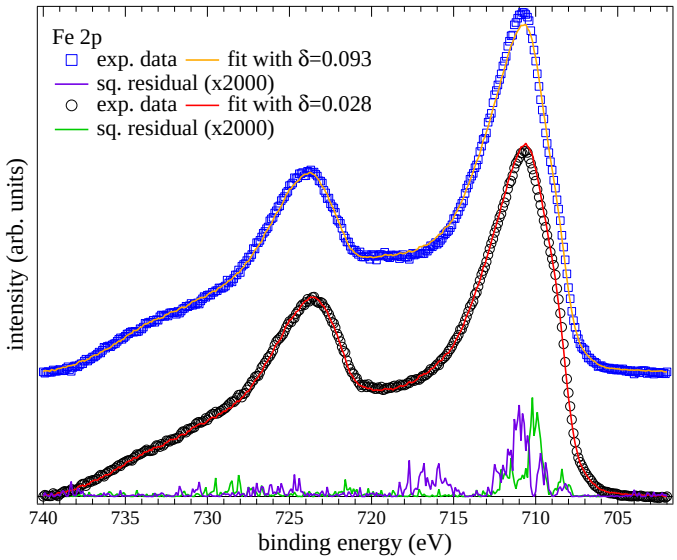

Figure 4.19: *Exemplary Fe 2p spectra measured in situ with Al-K_α radiation at two positions of a stepped Fe_3O_4/ZnO sample (sample no. 1). The experimental data, the corresponding fit with reference data, and the squared residual (multiplied by a factor of 2000) are shown for two values of the off-stoichiometry parameter δ.*

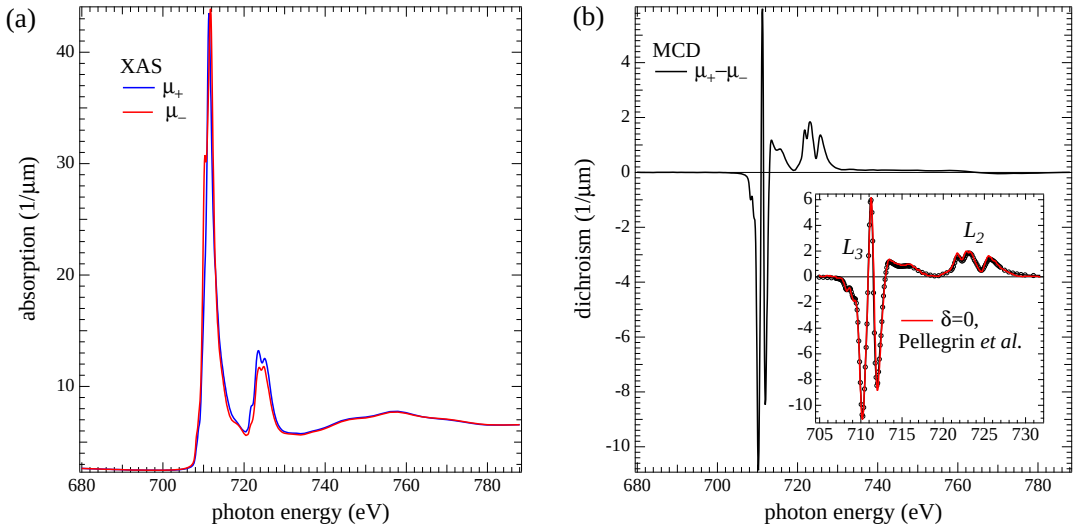

Figure 4.20: *(a) XAS and (b) XMCD Fe L-edge spectrum of a 16 nm thick Fe_3O_4/ZnO film (sample no. 1) taken at 70° incidence with respect to sample normal in a magnetic field of $\mu_0 H = \pm 3$ T and at room temperature. The inset in (b) shows an enlarged region at the resonance (black) and the reference spectrum with $\delta = 0$ (red).*

leads to the conclusion that the surfaces of Fe_3O_4 films of various thicknesses exhibit quite similar magnetic properties.

The orbital magnetic moment is on the order of $0.05\,\mu_B$/f.u. and therefore is almost quenched in comparison with the spin magnetic moment. The two negative values in Tab. 4.3 can be considered as runaway values. As was already discussed in Sec. 3.3.3, sign and size of the orbital moment are very sensitive to the integration range used for the sum-rule analysis. The obtained orbital moment is in the range of values observed by Goering *et al.* [113] and Kallmayer *et al.* [159]. We used an integration range similar to the one used by Goering *et al.* (cf. Sec. 3.3), and thus the results should be fairly comparable.

The off-stoichiometry parameter δ, which was extracted from comparison of unpolarized XAS spectra with literature data as explained in Sec. 3.3.3, ranges from 0.026 to 0.038 (see Tab. 4.3). The electron escape depth, λ_{XAS}, valid for XAS spectra was determined by the desaturation procedure. All stoichiometry values are in good agreement with values obtained by XPS measurements at two take-off angles, which are also listed in Tab. 4.3. It can be seen that δ increases upon decreasing the probing depth λ. This implicates that an off-stoichiometric layer is located at the surface of all films.

However, the reduction of the magnetization to values in the range from 2.55 to $2.88\,\mu_B$ in comparison with the bulk value of $3.83\,\mu_B$ cannot be explained merely by this off-stoichiometry of the surface layer. According to Eq. (2.1) the magnetization would be $3.77\,\mu_B$/f.u. for values of δ as obtained by XAS. These values of δ correspond to the average stoichiometry of the layer probed by XMCD. Even if one takes the somewhat larger δ measured by XPS to calculate the magnetization, the expected magnetization would still be $3.62\,\mu_B$/f.u.

Also, it can be concluded from the experiments that surface contamination and exposure to air do not significantly affect the magnetization and the XAS spectra, since *in situ* and *ex situ* measured samples show similar results of magnetic moments and stoichiometry. The origin of the reduced magnetization will be discussed in detail in Sec. 4.5.3.

Figure 4.21 displays magnetization curves of Fe_3O_4/ZnO films taken by measuring the XMCD signal at the Fe^{2+} resonance at about 710 eV as a function of the applied field. Graphs in (a) and (b) illustrate the magnetization curves at different incidence angles and temperatures, respectively. Altogether, these curves demonstrate ferromagnetic behavior, hysteresis, and an in-plane easy axis. Coercive fields of Fe_3O_4/ZnO samples range from 47 to 67 mT and their remanence magnetization is between 34 and 51 % of the value at $\mu_0 H = 3$ T for the nearly in-plane 70° incidence geometry. For out-of-plane 0° incidence measurements these values are considerably smaller, viz. 24 to 48 mT for the coercive field and 4 to 6 % for the remanence. Both in-plane characteristics are comparable to values for PLD-grown films on ZnO and Al_2O_3 reported by Nielsen *et al.* [137]. On the other hand, Margulies *et al.* found smaller coercive fields of 8.5 to 15 mT for (001)-oriented films and a vanishing coercive field smaller than 0.5 mT for a bulk specimen [40]. It can be conjectured that the larger coercive field of the here presented

(111)-oriented films is linked to a larger density of structural imperfections. Finally, both coercive field and saturation moment slightly enlarge for lower temperature, which is the same behavior as established for single crystals [160].

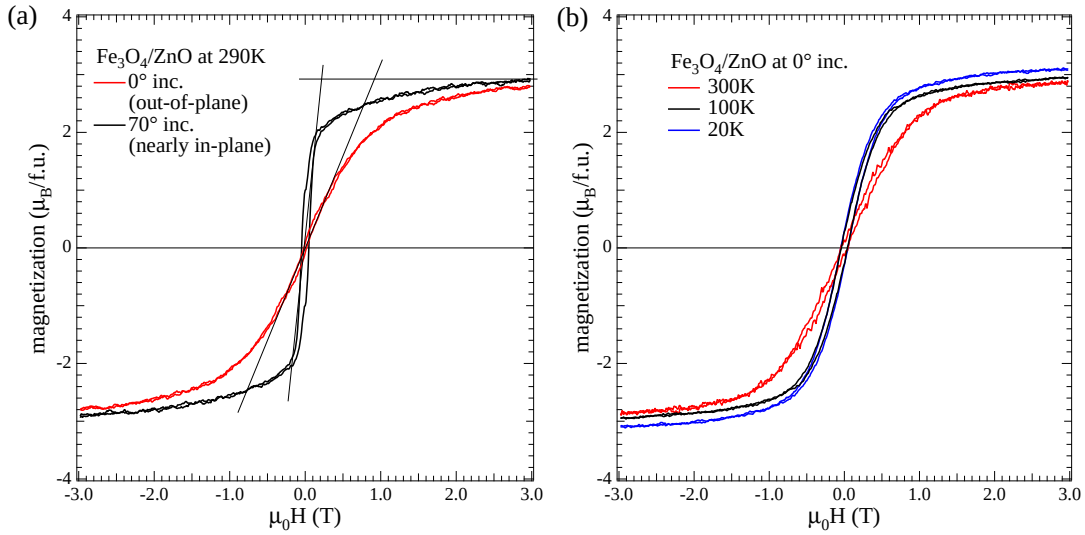

Figure 4.21: *XMCD magnetization curves of Fe_3O_4 films on ZnO. The magnetic moments were determined from a sum-rule analysis of XMCD spectra. (a) Fe_3O_4 film (sample no. 12) at two incidence angles. (b) Fe_3O_4 film at different temperatures (sample no. 10).*

Loops taken at two incidence angles reveal a strong anisotropy between the hard out-of-plane axis and the easier in-plane axis. The anisotropy field, which can be estimated from the intersection of the slope of the magnetization curve for low fields with the saturation magnetization (see Fig. 4.21), varies from approximately 0.6 to 0.9 T for different samples. These values are therefore in some cases larger than the field expected for pure shape anisotropy, which is $\mu_0 M_S = 0.6\,\mathrm{T}$. For this reason, other relevant contributions to the magnetic energy have to exist. As explained in Sec. 4.2, the films are in a strained state (macro strain) due to the incompletely relaxed mismatch. Assuming that the strain is homogeneous and elastic, the associated stress introduces the following, additional magnetoelastic energy, E_{me} [7]:

$$E_{me} = -1.5\lambda_{100}\sigma(\alpha_1^2\gamma_1^2 + \alpha_2^2\gamma_2^2 + \alpha_3^2\gamma_3^2) - 3\lambda_{111}\sigma(\alpha_1\alpha_2\gamma_1\gamma_2 + \alpha_2\alpha_3\gamma_2\gamma_3 + \alpha_3\alpha_1\gamma_3\gamma_1), \quad (4.2)$$

where λ_{100} and λ_{111} are the magnetostriction coefficients (taken from Ref. [161]) and α_i and γ_i are the direction cosines of magnetization and stress, respectively. Table 4.4 lists the magnetocrystalline anisotropy, shape anisotropy, and the magnetoelastic energy for a positive in-plane and negative out-of-plane strain with typical strain values determined from XRD (see Tab. 4.1).

The shape anisotropy energy contributes the largest part to the overall magnetic energy, but magnetoelastic energy also adds a significant amount which—most importantly—

introduces an additional in-plane anisotropy. The magnetocrystalline anisotropy favors an easy axis along the [111] direction, however, its contribution to the overall energy is small in comparison to the others. It can be concluded from the shown exemplary calculated values that the magnetic energy is quite sensitive to the strain state and that the values are in reasonable agreement with the experimental observation of an additional anisotropy field. Since the strain state depends on the exact deposition conditions and the film thickness, it is clear that the magnetic anisotropy can vary for each sample. The magnetoelastic energy is a function of the temperature-dependent magnetostriction coefficients, λ, and therefore itself varies with temperature. This behavior could be responsible for the different initial slope of the magnetization curve at low temperatures (see Fig. 4.21(b)). However, no calculations were made for the monoclinic low-temperature phase since data on the strain state at low temperatures were not available.

Table 4.4: *Magnetic energies of strained Fe_3O_4 on ZnO at 300 K.*

direction	[111] (out-of-plane)	[$\bar{2}$11] (in-plane)	[0$\bar{1}$1] (in-plane)
macro strain (%)	-0.32	$+0.6$	$+0.6$
stress (N/m^2)	$1.3 \cdot 10^8$	$1.72 \cdot 10^9$	$-2.39 \cdot 10^8$
magnetoelastic energy (J/m^3)	$8.33 \cdot 10^4$	$-8.15 \cdot 10^4$	$4.9 \cdot 10^4$
magnetocrystalline energy (J/m^3)	$-3.67 \cdot 10^3$	$-2.75 \cdot 10^3$	$-2.75 \cdot 10^3$
shape anisotropy* (J/m^3)	$1.45 \cdot 10^5$	0	0
sum of magnetic energies (J/m^3)	$2.24 \cdot 10^5$	$-8.43 \cdot 10^4$	$4.63 \cdot 10^4$
anisotropy field (T)	1.29	0 (easy axis)	0.544

*: A saturation magnetization of $3.83\,\mu_B/f.u.$ was used for the calculation

The saturation moments of 0° and 70° incidence measurements, which have been determined from the sum-rule analysis of XMCD spectra, taken at 3 T and cross-checked with the ones taken at 1.5 T, are identical within their error bar. However, it was observed that the 0° incidence curves run systematically below the 70° incidence curves by a few percent for all samples (see also Tab. 4.3) even for fields larger than the calculated anisotropy field. This behavior points towards a slight overestimation of the magnetic moments determined at 70° incidence, possibly due to the desaturation procedure.

4.5.2 Magnetometry

Figure 4.22 shows the in-plane magnetization of an Fe_3O_4/ZnO sample determined by magnetometry with a superconducting quantum interference device (SQUID), along with the XMCD out-of-plane magnetization and the expected bulk saturation value. The magnetization was measured up to high fields of $\mu_0 H = 7\,\mathrm{T}$ to ensure full saturation.

The diamagnetic contribution of the ZnO substrate was removed from the signal by fitting and subtracting a linear slope with $\chi = -2.164 \cdot 10^{-6}$. This value of the susceptibility is in reasonable agreement with the literature value for ZnO, $\chi_{\mathrm{ZnO}} = -2.05 \cdot 10^{-6}$ [162]. The curve in Fig. 4.22(a) indicates slow saturation behavior with a closure of the magnetization loop only at a field of about $\mu_0 H = 0.2\,\mathrm{T}$. The increase of the magnetic moment between $\mu_0 H = 3\,\mathrm{T}$ and $7\,\mathrm{T}$ is merely about $1\,\%$ so that the XMCD derived magnetization can be regarded as the saturation magnetization of the samples.

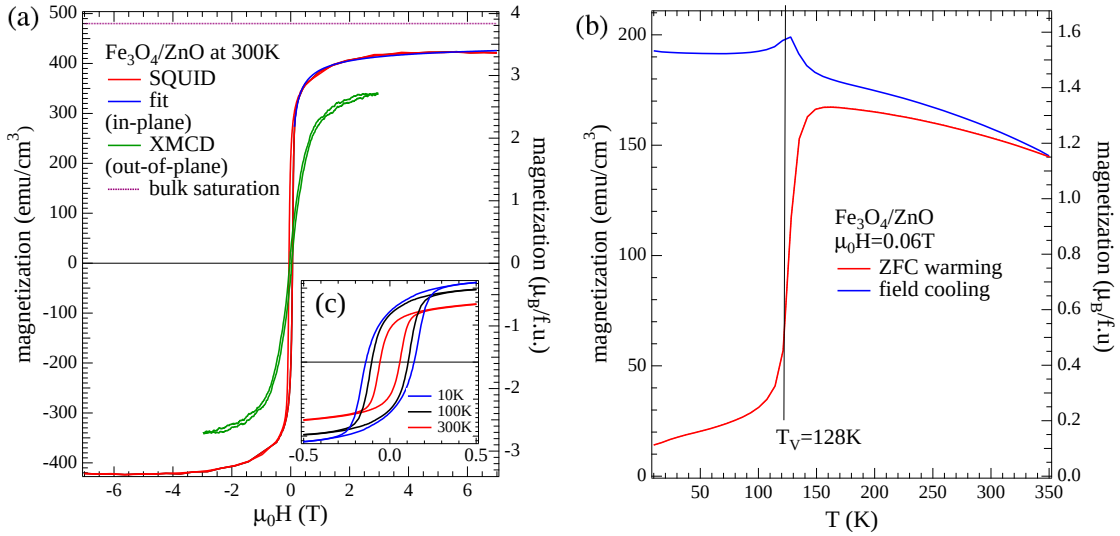

Figure 4.22: *SQUID characterization of an Fe_3O_4/ZnO sample (sample no. 7) with an in-plane applied magnetic field. (a) Hysteresis curve at 300 K up to large fields. For the sake of comparison the XMCD magnetization curve and the bulk saturation magnetization are also shown. (b) $M(T)$-curves measured in $\mu_0 H = 0.06$ T. Warming cycle of a zero-field-cooled sample (ZFC) and field-cooling cycle. (c) The inset shows minor magnetization loops up to 0.5 T at different temperatures.*

According to the inset, the coercive field is about $\mu_0 H = 60\,\mathrm{mT}$, which is in good agreement with values obtained from the XMCD magnetization curves [4]. From minor magnetization loops measured at different temperatures it can be concluded that the coercive field slightly increases at lower temperature (see inset (c) in Fig. 4.22), which also is fully consistent with XMCD $M(H)$-curves and literature.

Both slow saturation behavior and reduced saturation moment compared to the bulk value are in accordance with earlier reports on Fe_3O_4 thin films (see e.g. Refs. [40, 163]). In comparison with measurements of bulk crystals [36] the approach to saturation is markedly slow. It was argued in Sec. 4.5.1 that the anisotropy of the magnetic energy mainly influences the initial slope of the magnetization curves, but it cannot explain the slow approach to saturation at high fields. The essential contribution rather comes from

[4] For a comparison with literature see Sec. 4.5.1.

a reduced magnetization due to APBs. The approach to saturation of the $M(H)$-curve is well described by the law $M = M_S(1 - b/H^{1/2})$ (see Sec. 2.2) with best fit parameters of $M_S = 450\,\mathrm{emu/cm^3}$ and $b = 0.139 \pm 0.002\,\mathrm{T^{1/2}}$ (see fit in Fig. 4.22(a)). These fit parameters are within the typically observed range for films on MgO or Al_2O_3. Bataille *et al.* found a mean APD size of 20 nm [48] in samples which exhibited a comparable value of the fit parameter b. According to the microstructure analysis shown in Sec. 4.3 such an APD size could be at hand in the present sample. Since the fit parameter $M_S = 450\,\mathrm{emu/cm^3}$ is nearly equal to the bulk saturation, the magnetization behavior of the investigated thin film corresponds to a stoichiometric single crystal which exhibits a considerable density of APBs.

The temperature-dependent magnetization measured in an applied field of 0.06 T is shown in Fig. 4.22(b). The zero-field-cooled warming cycle (red curve) exhibits a large jump of the magnetization in the vicinity of the Verwey-transition temperature of $T_V = 128\,\mathrm{K}$ from almost zero magnetization to a sizeable, slowly varying value in the high-temperature phase. This behavior is qualitatively similar to the $M(T)$-curve of the GaAs sample (see Fig. 6.19) and to literature data, however, the magnitude of the magnetization jump is unusually large and also the width of the transition is small (cf. Ref. [64]). The magnetization jump is roughly $1\,\mu_B$/f.u., which is in coincidence with the value predicted by the magneto-electronic model (cf. Fig. 2.5).

In contrast, the field-cooling cycle shows a small peak instead of magnetization jump at the transition temperature. The observed peak at the transition temperature could well be related to the isotropic point, i.e., the temperature of vanishing magnetocrystalline anisotropy constants, which is known to lie slightly above the Verwey-transition temperature [67]. If the direction of the applied magnetic field is not along the easy axis, which is the case in the high-temperature as well as the low-temperature phase, the magnetic moment will be canted away due to the magnetocrystalline anisotropy. At the isotropic point the magnetocrystalline anisotropy vanishes and therefore the sample will be more easily magnetized yielding a peak in the $M(T)$-curve.

The occurrence of this phase transition and the small temperature interval over which the transition takes place evidence good stoichiometric and structural properties of the 40 nm thick film (sample no. 7) [64]. It is established in the literature [67, 160] that the magnitude of the magnetization jump crucially depends on the applied field and is largest for relatively low fields around 0.1 T (see also Sec. 2.2).

4.5.3 Origin of the reduced surface magnetization

In summary, there remains a large discrepancy between the volume magnetization determined by SQUID magnetometry (see Sec. 4.5.2) and the surface magnetization obtained by XMCD (see Sec. 4.5.1). The SQUID data can be regarded as quite precise since the intrinsic error only originates from the uncertainty to determine the correct film volume. This error is estimated to be $\pm 5\,\%$. Taking the fit parameter M_S as the true bulk saturation, i.e., corrected for the reduced magnetization due to APBs at low fields, the

magnetization from SQUID is only by about 6 % lower than the expected bulk value. Hence, it has to be clarified if there are errors inherent to the XMCD technique which can account for the observed deviation.

Firstly, the validity of the XMCD sum rules has to be discussed. The sum rules can be regarded as accurate (within 7 %) for materials such as elemental Fe or Co if experimental artifacts are eliminated [164]. XMCD measurements of Fe_3O_4 single-crystal surfaces [113, 114] showed nearly bulk-like moments, which suggests the validity of the sum rules also for magnetite.

An often raised objection against the sum rues is that the contribution of the magnetic dipole operator, $\langle T_z \rangle$, to the experimentally determined effective spin moment is not exactly known as already explained in Sec. 3.3. Goering *et al.* argue that the contribution of the magnetic dipole operator is negligible at least for a perfect, single-crystal surface of Fe_3O_4 [113]. Crocombette *et al.* have shown by calculations that $7\langle T_z \rangle / \langle S_z \rangle$ can be ignored for d^5 and d^6 configurations in a perfectly octahedral symmetry at room temperature (on the order of $2 \cdot 10^{-3}$ or less) [165]. However, at the very surface of a crystal where the Fe ion is coordinated only by five O ions, the ratio can be larger. For d^5 it is again negligible, but for a d^6 configuration, which is actually relevant for the net magnetization Fe_3O_4, it is as high as +0.25. Because of the positive sign, this would result in an experimentally derived effective spin moment, m^*_{spin} which is *larger* than the actual spin moment (see Sec. 3.3.1). Therefore, it cannot explain the observed *reduced* moment.

Another error could be introduced into the sum rules by ignoring the p to s transitions at the L-edge according to Antonov *et al.* [166]. They compared magnetic moments obtained by a sum-rule analysis of *calculated* XAS and XCMD spectra with moments directly derived from LSDA+U calculations and claim that the sum-rule analysis systematically underestimates the spin magnetic moment of Fe_3O_4 by up to 10 % and the magnitude of the orbital magnetic moment by 50 % [166]. Although the exact comparability of calculated and experimental spectra remains questionable, the work nevertheless gives a preliminary estimate of the aforesaid error. This sum-rule related error could at least partly account for the reduced XMCD derived moments.

Similarly, Crocombette *et al.* [165] showed by means of simulations of XAS spectra that the error introduced into the sum rule due to mixing of L_3- and L_2-edges is about 10 % for the d^6 and 28 % for the d^5 configuration.

Other, yet experimental error sources of the XCMD technique in TEY mode are the sensitivity of the electron yield to the applied magnetic field and the saturation of the absorption signal. The first problem was experimentally minimized by applying a bias voltage to the sample (cf. Refs. [113, 167]). Comparison of magnetic moments derived by a sum-rule analysis in two different magnetic fields of $\mu_0 H = 1.5$ and 3 T with scaled magnetization curves shows that this first error is on the order of a few percent at most.

The saturation correction of spectra, which is another error source, is mainly dependent on the choice of the accurate electron escape depth, λ_e. Indeed, the correction procedure strongly changes the absolute value of the absorption coefficient of the spectra.

However, the sum rule for the spin moment is based on the relative ratio of integrals over these spectra and therefore the influence on the derived spin moment is much smaller. We have tested different saturation corrections and found that the discrepancy in the derived spin moment is smaller than 5 % for reasonable values of λ_e, while the orbital moment can change drastically and even become negative [168]. The latter has, however, only a small absolute contribution to the overall moment, and therefore the saturation effect can account for the reduced surface magnetization only to a small extent.

Altogether, these errors cannot fully account for the reduction of the XMCD-derived magnetic moment. After discussing these extrinsic sources for the observed magnetization reduction, intrinsic, i.e., sample-related, issues will be highlighted in the following.

The analysis of the dependence of the magnetic moment on the off-stoichiometry parameter δ shows that the reduction of the number of Fe_{oct}-site moments, which are ultimately responsible for the net magnetization, does not lead to the observed decrease of the magnetization (see Tab. 4.3 and Eq. (2.1)). This means that another mechanism exists which reduces the magnetization of the sample by 0.7 to 1.3 μ_B/f.u., i.e., after all 19 to 33 % of the bulk value at room temperature, practically independently from its stoichiometry.

Based on this reasoning, other structural defects such as APBs, the presence of the surface, or impurities (e.g. adsorbates on the surface) must exist in the presented samples, and perturb the magnetic exchange interaction between moments and as a consequence their spin order. For a ferrimagnet the spin order sensitively depends on the relative strength of the exchange interactions $J_{\text{oct-tet}}$, $J_{\text{tet-tet}}$, and $J_{\text{oct-oct}}$ (see Sec. 2.2). A change of these interactions at defects can result in a spin decanting of the Fe_{oct} moments and a concurrent decrease of the net magnetization. The spin order is therefore not completely destroyed, but rather changed and the net magnetization is concurrently decreased. Insofar, a magnetic 'dead' layer at the surface [169] or interface [170] of an Fe_3O_4 film would be the most simple, possible model which could describe the lowering of the magnetization. If one takes into account the exponential damping of the XMCD signal with higher depths of origin, the thickness of the magnetic 'dead' surface layer has to be roughly 0.6 nm to induce the observed magnetization decrease of about 1 μ_B/f.u. This corresponds approximately to the surface roughness of the magnetite films. On the other hand, it cannot be concluded from XMCD results if magnetic 'dead' interface layer is present as well, since the technique is not sensitive to the interface even for the thinnest investigated film (see Tab. 4.3). However, an additional magnetically inactive interface layer could in principle be present. SQUID magnetometry for various film thicknesses or polarized neutron reflectivity, which is sensitive to the vertical magnetization profile, would be needed to clarify the existence of such an interface layer.

Nanoparticles exhibit a strongly increased ratio of surface- to bulk-like atoms and therefore are well-suited model systems to investigate surface-related effects on the magnetization. Pérez *et al.* [171] have demonstrated very different properties for magnetite nanoparticles with a diameter of 5.8 and 5.6 nm and a coating consisting of covalently bonding Oleic acid and adsorbed Polyvinyl alcohol, respectively. The former nanoparti-

cles exhibited $m_{spin} = 3.27\,\mu_B$/f.u., but the latter only $m_{spin} = 2.25\,\mu_B$/f.u. as revealed by XMCD *and* magnetometry. This discrepancy together with a threefold increase of the m_{spin}/m_{orb} ratio were ascribed to the lower degree of crystallinity at the surface, the irregular shape and increased density of in-volume defects of the Polyvinyl alcohol-coated nanoparticles. Although the production process and structure of such nanoparticles are distinct from compact thin films, the surface plays a crucial role in the determination of magnetic properties of both systems.

Similarly Goering *et al.* detected with XMCD in TEY mode a magnetization of $m_{spin} = 1.7\,\mu_B$/f.u for a polished surface of an Fe_3O_4 single crystal [158]. The alteration of the electronic structure at the surface of magnetite single crystals is also known from PES investigations from Schrupp *et al.* [101, 172].

Moreover, it has to be noted that reduced XMCD-derived magnetic moment have already been detected for Fe_3O_4 thin films. Kallmayer *et al.* [159] found spin moments of $m_{spin} = 2.22$ to $2.97\,\mu_B$/f.u. and orbital moments of $m_{orb} = 0.006$ to $0.18\,\mu_B$/f.u. for 100 nm thick films on MgO(001) and Al_2O_3(001) substrates at 77 K and 300 K. The saturation magnetization of their samples determined by vibrating sample magnetometry was nearly the bulk value of magnetite. However, they merely concluded that the discrepancy was due to the experimental error of the vibrating sample magnetometry or due to finite polarization of the x-rays. In addition, Orna *et al.* [173] report $m_{spin} = 1.83$ and $3.6\,\mu_B$/f.u. together with m_{orb} smaller than $0.18\,\mu_B$/f.u. for an 8 and accordingly 58 nm thick film on MgO(001) at 300 K. They also observed by magnetometry techniques that the magnetization strongly decreases for decreasing film thickness.

Summing up, it can be concluded that the observed reduction of the surface magnetization cannot fully be explained by intrinsic errors of the XMCD technique. The observed reduction is ascribed to a magnetically inactive surface layer of a few ångströms thickness. This layer is off-stoichiometric but its off-stoichiometry alone does not lead to the reduced magnetization.

5 $Fe_{3-\delta}O_4$ thin films on InAs

InAs, which is among the widespread materials in semiconductor technology, has also been proposed as a promising template for the deposition of magnetite for future spintronic devices. Among others, InAs exhibits a large spin-diffusion length, a high electron mobility, and a tunable spin-orbit coupling strength [174]. There is also some potentiality that magnetite grows epitaxially on InAs(001), because the lattice mismatch is only $-1.6\,\%$ if the (001) faces are rotated by 45° against each other in-plane (see below). However, as was established in Sec. 3.1.5, InAs is thermodynamically unstable in contact with Fe_3O_4 at elevated growth temperatures, which complicates epitaxial growth.

5.1 Substrates and growth procedure

InAs substrates were cut from a Zn-(p-)doped wafer (MaTecK GmbH) and wet-chemically etched with sulphuric acid prior to loading into the UHV growth chamber. As an *in situ* treatment, substrates were annealed at 470 to 510°C prior to actual film growth. As was verified by *in situ* XPS measurements, this substrate treatment results in clean InAs surfaces without its native oxides. The good substrate quality and surface ordering was confirmed by sharp (4×2) LEED patterns. According to the XPS analysis this clean surface status is slightly In-rich, which is the reason why the surface exhibits an In-stabilized (4×2) surface reconstruction.

Fe_3O_4/InAs(001) samples were grown by simultaneous deposition of Fe, arriving from an electron-beam evaporator with a deposition rate of about 3 Å/min, and O_2 from an appropriate molecular oxygen background pressure of typically $1 \cdot 10^{-5}$ mbar for the first 20 min and $5 \cdot 10^{-6}$ mbar for the remaining duration of growth (cf. Tab. A.1). Thicknesses of Fe_3O_4 films estimated from XPS intensities are given in Tab. 5.1. The film thickness determined from a TEM analysis is larger by a factor of 4/3, which already suggests an incomplete coverage of the substrate during growth or interfacial diffusion.

The lattice mismatch between Fe_3O_4(001) and InAs(001) faces is only $-1.6\,\%$ assuming that one Fe_3O_4 unit cell with lattice constant 8.397 Å grows on two InAs surface unit cells with a lattice constant of 4.27 Å (see Fig. 6.2). This corresponds to an in-plane rotation of the Fe_3O_4(001) face against the InAs(001) face by 45°. However, in a PLD-growth study [175] other orientations have been proposed as well.

The absence of unambiguous LEED patterns taken on Fe_3O_4/InAs thin films prepared in the present work suggests that the growth result is rather polycrystalline or textured with random in-plane orientations of the single crystallites, but not epitaxial.

5.2 Microstructure

Figure 5.1(a) depicts a STEM image of an Fe_3O_4/InAs thin film[1]. It is obvious that the interfaces with the InAs substrate and the Pt capping layer are somewhat rougher in comparison with films grown on ZnO. The InAs surface exhibits a roughness of about 1 nm in the imaged area. This roughness results from the substrate treatment with sputtering and annealing and suggests that the surface is not perfectly smooth. On the other hand, the surface roughness of the magnetite film is probably due to the island-like growth.

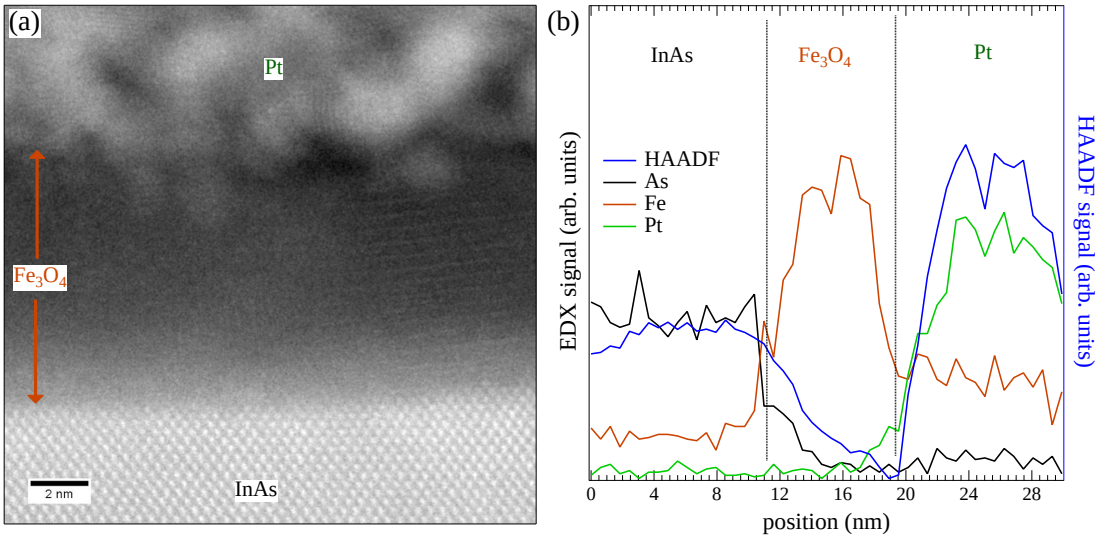

Figure 5.1: *TEM characterization of Fe_3O_4 grown on InAs(001) (sample no. 13). (a) STEM image from InAs$[1\bar{1}0]$. (b) EDX line scans of As, Fe, and Pt.*

While the atomic contrast of the InAs part of the STEM image is clearly visible, there is nearly no atomic contrast discernible in the film area. This indicates that along the width of the TEM lamella differently oriented Fe_3O_4 grains are present. Only in the right part of the imaged film area, some atomic contrast is observable in form of atomic rows which run approximately horizontally. The STEM measurements were performed with the incoming electron beam along an InAs$\langle 110 \rangle$ direction. In summary, the STEM characterization indicates that the grown films are polycrystalline, which is supported by the observation by LEED.

Energy dispersive x-ray spectroscopy (EDX) during STEM imaging was used to estimate the amount of interfacial intermixing. Results are shown in Fig. 5.1(b). The HAADF signal, i.e., the apparent contrast in the STEM image, is illustrated along with

[1]The STEM and energy dispersive x-ray spectroscopy (EDX) measurements were performed by Dr. M. Kamp at the Chair for Applied Physics of the University of Würzburg.

the EDX signal of Pt, Fe, and As, which is proportional to the respective atom concentration. The approximate assignment of the position of the EDX line scan to the InAs, Fe_3O_4, and Pt layer is indicated. Unfortunately, the signal to noise ratio of the scans is too low to allow for unambiguous statements on the atom distribution. However, it *appears* that both interfaces are not atomically sharp, which can, e.g., be seen in the profile of the As and Pt distribution. The height of the As profile runs similarly to the HAADF signal, which suggests that an approximately 2 nm thick layer right at the interface is an As-rich layer. The Fe signal exhibits a large step-like increase within the film area as expected. Note that the Fe signal is not zero outside of the film area, which is a result of scattering of electrons especially in the Pt layer towards the lenses and other parts of the TEM apparatus. Since these parts contain significant amounts of Fe, they produce some background signal in EDX scans.

5.3 Electronic and chemical structure studied by (hard) x-ray photoelectron spectroscopy

This section deals with a detailed study of Fe_3O_4/InAs thin films by means of *in situ* XPS and *ex situ* HAXPES. XPS was performed immediately after growth while HAXPES experiments were carried out after transport to the analysis chamber and without further surface treatment to minimize a change in chemical composition. The shown HAXPES measurements were conducted at beamline BW2 at HASYLAB in Hamburg with the sample at room temperature[2]. All shown spectra have been shifted to correct for charging by setting the O 1*s* binding energy to 530.1 eV as discussed in Sec. 3.2.6.

The Fe oxidation state of the films is assessed by the Fe 2*p* spectra shown in Fig. 5.2 (a). Fe $2p_{3/2}$ and $2p_{1/2}$ main-line peak positions are 710.5 and 724.0 eV, respectively, in excellent agreement with literature values for magnetite (see Sec. 3.2.5). Spectra taken with 1486 eV photons exhibit the structureless line shape between the two main peaks which is characteristic for magnetite, thus suggesting that the film is nearly stoichiometric. A quantitative comparison with reference spectra yields an off-stoichiometry parameter ranging from $\delta = 0.036$ to 0.055. The other spectra in Fig. 5.2 (a), which were taken at 3.5 keV and at different emission angles, are mutually identical, showing that the oxidation state is essentially the same for the corresponding information depths. However, the lineshape has changed significantly with respect to the *in situ* measured XPS spectra. The HAXPES spectra show increased background intensity at binding energies larger than 715 eV and additional spectral weight at the position of the Fe^{3+} charge-transfer satellite at around 720 eV. These variations are tentatively explained as an effect of prolonged exposure to air between experiments or by lateral sample inhomogeneity. It is additionally noted that the small feature at 703 eV just next to the Fe $2p_{3/2}$ main line

[2]Measurements were performed by G. Berner and A. Wetscherek.

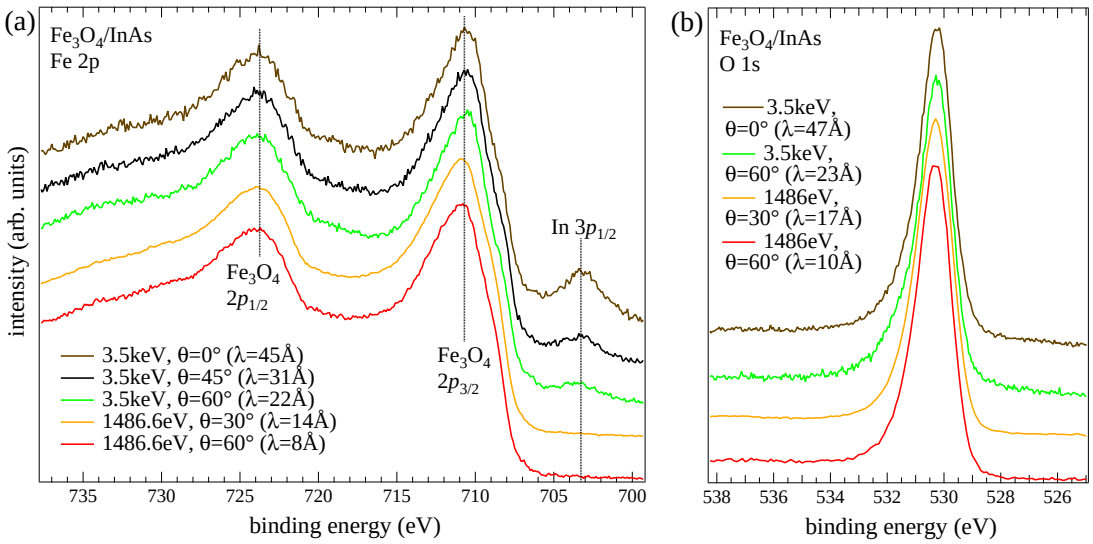

Figure 5.2: *(a) Fe 2p spectra of an Fe_3O_4/InAs film (sample no. 14) at various photon energies and electron emission angles. (b) O 1s spectra taken under the same conditions.*

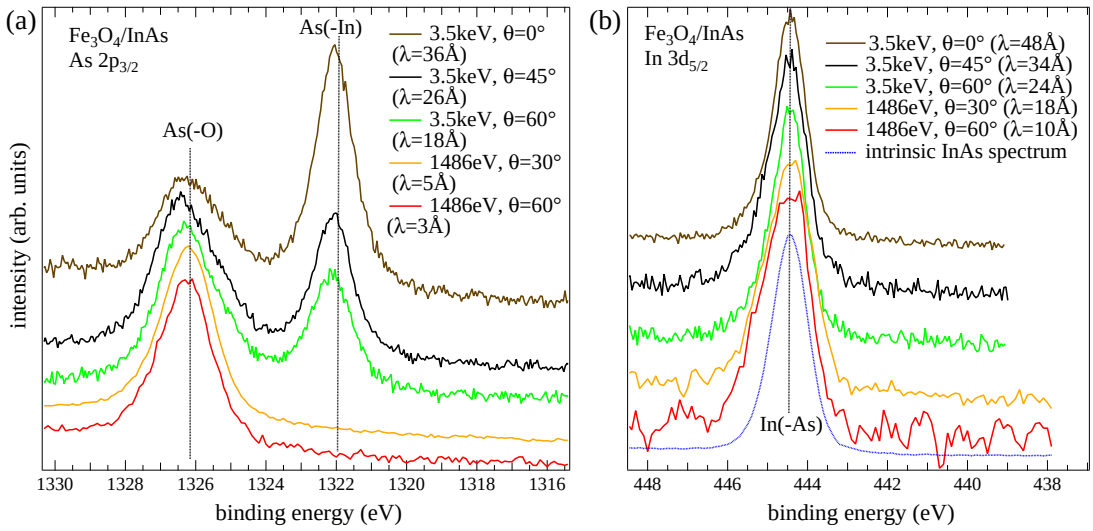

Figure 5.3: *(a) As $2p_{3/2}$ spectra of an Fe_3O_4/InAs film (sample no. 14) at various photon energies and electron emission angles. (b) In $3d_{5/2}$ spectra taken under the same conditions.*

originates from the In $3p_{1/2}$ level. As a signal from the substrate it is perspicuously suppressed for smaller information depth, as one would expect.

When using reactive codeposition of Fe and O_2 with an adjustable Fe/O_2 ratio for different layer thicknesses, various samples with different film thicknesses showed *in situ* XPS spectra similar to the above shown. It is therefore concluded that stoichiometric magnetite throughout the film thickness can be obtained if using the explained growth procedure for deposition on an InAs substrate. The HAXPES measurements rather show a modified oxidation state of the *ex situ* measured sample.

For the sake of completeness, O 1*s* core levels are depicted in Fig. 5.2 (b). The lineshape is slightly asymmetric indicating the presence of OH binding at surface-oxygen sites. Note, however, that the inelastic background is not removed from the shown spectra and thus emphasizes the aforementioned asymmetry. There is practically no difference between spectra taken with different information depths indicating that the extent of hydroxylation was not significantly altered by the exposure to air.

Examination of the substrate core levels As $2p_{3/2}$ and In $3d_{5/2}$ (see Figs. 5.3 (a) and (b), respectively) permits to estimate the degree of substrate oxidation and interdiffusion at the interface, which is present after growth. The main As $2p_{3/2}$ component at a binding energy of 1322.2 eV is readily assigned to the intrinsic signal from the substrate, i.e., to In-As bonding, and not to elemental As. The intensity of this low binding-energy peak is too high in the case of the top three spectra to be a signal of a possible, elemental As interface layer. The second component residing at the higher binding energy of 1326.4 eV can clearly be attributed to the arsenic oxides As_2O_3 and As_2O_5 (cf. Ref. [176]).

While the intrinsic InAs component is damped for measurements with higher surface sensitivity, the arsenic-oxide component increases with higher surface sensitivity (see Tab. 5.1). This increase of the arsenic-oxide component, however, is not very pronounced (less distinct than for the GaAs substrate, cf. Tab. 6.2). This suggests that the arsenic oxides are distributed inside the film, i.e., intermixed with the iron oxide, and are not entirely restricted to a thin layer at the interface or at the surface.

The substrate signal is practically not detectable by means of conventional XPS with Al-K_α radiation on the same sample. As already discussed above, the rather abrupt change between spectra measured with 1486.6 eV and 3.5 keV is possibly influenced by exposure to air between those experiments or by lateral sample inhomogeneity.

The amount of arsenic oxides did not vary significantly when elevating the film growth temperature from 275 to 350°C. In contrast, the In $3d_{5/2}$ signal was considerably stronger at the same nominal Fe_3O_4 film thickness for the higher growth temperature, indicating a larger In-content of the film (see Tab. 5.1). Similarly, an increase of the In_2O_3/As_2O_3 ratio was observed by Laughlin and Wilmsen at rising growth temperature when analyzing the composition of the thermally grown oxide layer on InAs [178]. This effect was attributed to the higher volatility and evaporation of As_2O_3 at larger temperature. In our case, a change of the growth mechanism or the amount of substrate coverage with temperature could contribute to this change as well. Unfortunately, these points

Table 5.1: *Relative chemical composition (in %) of Fe_3O_4/InAs samples calculated from PES spectral intensities of the listed core levels. Growth temperature and the film thickness estimated from the intensities at small coverage are listed for each sample.*

	As 2p or As 3d InAs	As 3d oxide	In 3d or In 4d	O 1s	Fe 2p
sample no. 14*, $T_{growth} = 280°C$, $t_{XPS} = 6.1\,nm$					
3.5 keV, 0°	1.8	1.4	3.2	48.5	34.0
3.5 keV, 60°	1.0	1.7	1.2	44.6	35.1
1486 eV, 30°	0.7	2.1	1.0	55.0	41.3
1486 eV, 60°	0.1	2.0	0.3	56.7	41.2
sample no. 15*, $T_{growth} = 350°C$, $t_{XPS} = 6.1\,nm$					
3.5 keV, 0°	1.1	2.0	8.6	51.4	29.1
3.5 keV, 45°	0.5	1.8	8.1	50.4	29.6
1486 eV, 30°	0.7	2.0	10.2	52.8	34.5
1486 eV, 60°	0.1	2.2	8.3	55.8	34.0
sample no. 16, $T_{growth} = 360°C$, $t_{XPS} = 4.0\,nm$					
3.5 keV, 0°	3.4	2.4	15.7	48.4	5.1
3.5 keV, 45°	1.5	2.8	12.4	54.6	5.8
3.5 keV, 60°	1.1	3.6	11.9	51.7	8.8
1486 eV, 30°	0.6	1.9	10.3	59.0	28.1
1486 eV, 60°	0.2	3.1	20.1	53.4	24.4

*: cf. Ref. [177]

cannot be clarified further since data directly elucidating the growth mechanism are not available.

Now, we turn to the analysis of the In $3d_{5/2}$ level in Fig. 5.3(b). In contrast to the As $2p_{3/2}$ level, the In level consists of one broad, rather symmetric line. Also the form of the In $3d_{5/2}$ level does not change significantly upon variation of the information depth (see Fig. 5.2(b)). The In $3d_{5/2}$ spectrum taken on a clean, filed InAs wafer, which can be considered as the intrinsic spectrum for InAs, is very similar to the spectra taken on the deposited magnetite films apart from a small asymmetric broadening on the high binding-energy side. In fact, the chemical shift of the In $3d_{5/2}$ binding energy between InAs and In_2O_3 is 0 eV according to Hollinger *et al.* [176] and smaller than 0.4 eV as found by own measurements on reference compounds. Because of the too small binding-energy shift and the absence of a clear spectral change at different information depths, the indium-oxide and the intrinsic InAs component cannot unambiguously be separated from each other. The occurrence of an additional third component such as elemental In, e.g., caused by a reduction process, seems highly unlikely and has never been reported in the relevant literature. Since the In/As(-In) ratio (see Tab. 5.1) is changing significantly for different samples and preparation conditions, it is, however, not reasonable to assign

the complete spectral weight to In(-As) bonds. Instead, the change of the In/As(-In) ratio has to be attributed to varying amounts of In_2O_3 together with an undeterminable fraction of In(-As). This assignment is corroborated by the simultaneous increase of the O/Fe ratio and the In-content of sample no. 16 (see Tab. 5.1), which was grown at the highest temperature of 360°C. Thermodynamics in Sec. 3.1.5 predicts the reaction of Fe_3O_4 and InAs to FeO, In_2O_3, and elemental arsenic at temperatures higher than 700 K. The experimental observation seems to support this temperature-dependent instability of the interface. It should be made clear that interfacial intermixing and reactions are reflected in the larger fractions of In and As in the PES signal.

5.4 Magnetic properties

Figure 5.4(a) shows the XMCD spectrum taken on an Fe_3O_4/InAs thin film. For the sake of comparison, a reference spectrum from Pellegrin *et al.* with an off-stoichiometry of 0.23 is also plotted (cf. Fig. 3.15). The reference spectrum was scaled and shifted in energy to match the Fe^{3+}_{tet} peak. As can be seen, the spectra are very similar to each other. Thus, the off-stoichiometry of the grown layer is nearly the same as for the reference spectrum within the probing depth of XAS. This large off-stoichiometry in comparison with the results from the PES analysis is most likely due to a prolonged storage of the sample in air before XMCD measurements.

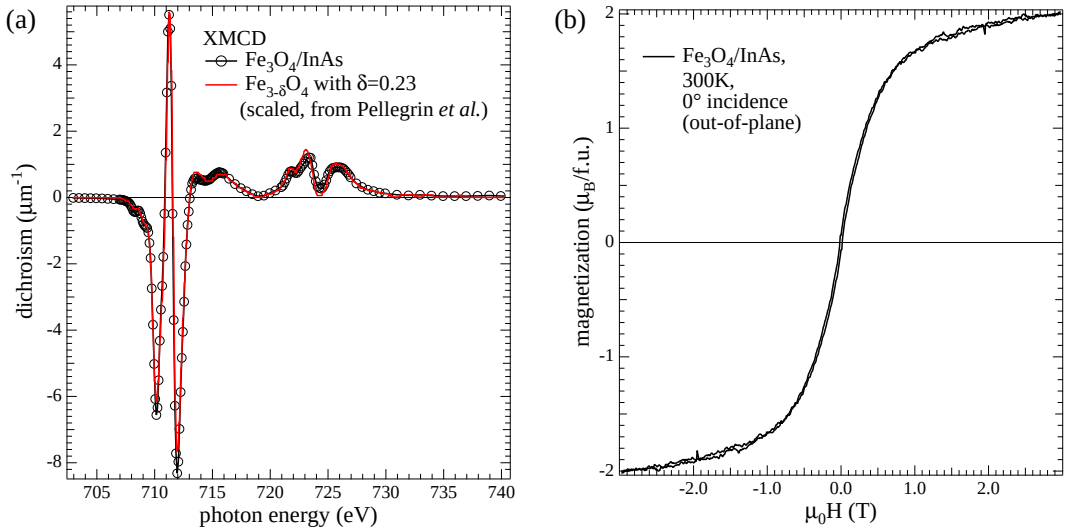

Figure 5.4: *XMCD characterization of an Fe_3O_4/InAs sample (sample no. 13). (a) XMCD spectrum and scaled reference spectrum of $Fe_{3-\delta}O_4$ with $\delta = 0.23$ from Pellegrin et al. [116] for comparison. (b) Magnetization curve measured at 300 K and 0° incidence.*

The magnetization curve in Fig. 5.4(b) was measured at the Fe^{2+}_{tet}-peak position for 0° incidence and at room temperature. It shows ferromagnetic behavior with almost

vanishing coercive field. Moreover, the curve is characteristic for out-of-plane anisotropy and shows a markedly slow approach to saturation. The slope is comparable to those of XMCD magnetization curves of Fe_3O_4/ZnO thin films.

The sum-rule derived magnetization measured at $\mu_0 H = 3\,\mathrm{T}$ is about $2\,\mu_B$/f.u. which is distinctly smaller than the bulk magnetization for stoichiometric magnetite and also the value estimated for $Fe_{2.77}O_4$, i.e., $3.39\,\mu_B$/f.u. (cf. Eq. (2.1)). The possible origin of the further reduction of the magnetization besides the off-stoichiometry effect was already discussed in detail in Sec. 4.5.3. However, here the polycrystalline nature of the film could also have a strong influence.

Figure 5.5(a) shows the in-plane magnetization of an Fe_3O_4/InAs sample determined by SQUID magnetometry. The diamagnetic contribution of the InAs substrate was removed from the signal by subtracting a linear slope analogously to the procedure applied to the film on the ZnO substrate. The magnetization was calculated by normalizing the experimental magnetic moment to the film area and thickness (obtained by TEM). Curves at different temperature were measured up to an applied field of only $\mu_0 H = 0.5\,\mathrm{T}$. Therefore, the magnetization most probably will not correspond to the actual saturation value and the shown curves represent minor magnetization loops. This becomes especially evident when one examines the curve taken at 10 K, which is hardly a closed loop. Also the variation of the maximum magnetization for the three shown temperatures is unusually high. The magnetization is distinctly smaller than the expected bulk magnetization of magnetite for all shown temperatures and is even smaller than the XMCD-derived magnetization. This also points towards a minor-loop behavior of the curves. Nevertheless, the magnetic response is clearly ferromagnetic for all curves. The coercive field strongly varies between 90 mT at low temperature and practically zero at room temperature.

The slow saturation behavior in the high-field regime, which was also observed for films on ZnO, cannot be confirmed by SQUID results, but by the XMCD magnetization curve. It can be assumed that the Fe_3O_4/InAs films contain a density of APBs similar to films on ZnO. In addition, the magnetic exchange interactions could be changed at the grain boundaries of the polycrystalline film like at APBs. However, there are not enough magnetometry and TEM data to make a final conclusion about the influence of these structural defects on the exchange interactions and magnetization.

The temperature-dependent magnetization measured in an applied field of 0.06 T is shown in Fig. 5.5(b). The zero-field-cooled warming cycle (red curve) exhibits a magnetization jump at a temperature of 100 K with vanishing magnetization in the low-temperature phase. It is interpreted as the sign of a Verwey transition shifted to lower temperature. In comparison with the curve measured for the film on ZnO, the transition is broad and the magnetization jump is small. In opposition to the warming cycle, the field-cooling cycle (blue) displays an incipient *increase* of the magnetization at roughly the same temperature.

Occurrence of the Verwey transition by itself demonstrates that at least some part of the Fe_3O_4/InAs sample exhibits a stoichiometry very close to the ideal bulk material.

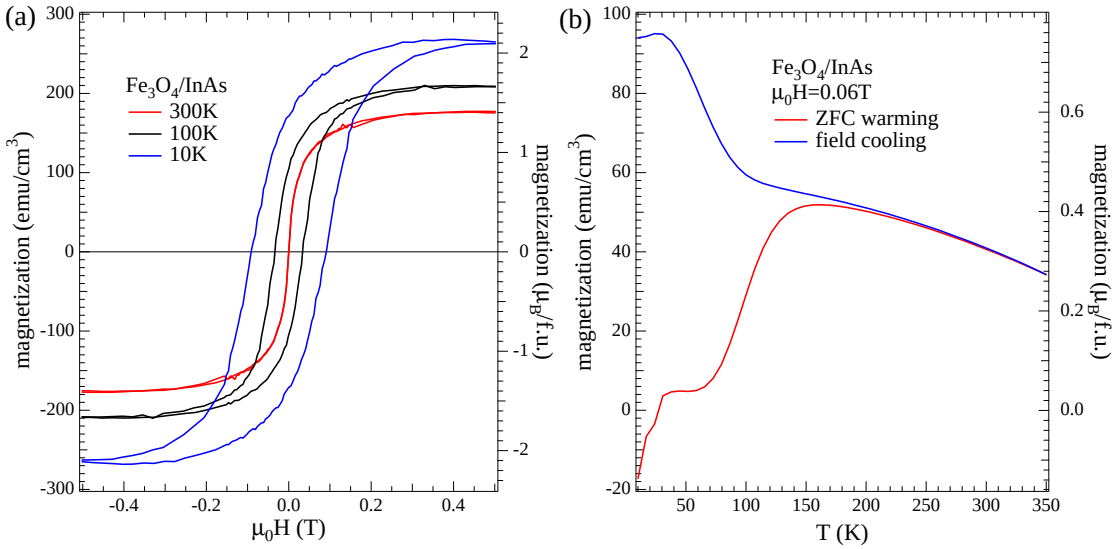

Figure 5.5: *SQUID characterization of an Fe_3O_4/InAs sample (sample no. 13) with an in-plane applied magnetic field. (a) Magnetization curves at three temperatures. (b) $M(T)$-curves measured in $\mu_0 H = 0.06$ T. Warming cycle of a zero-field-cooled sample (ZFC) and field-cooling cycle.*

However, both the low transition temperature and the broad temperature range over which the transition occurs indicate that the sample might be inhomogeneous and/or suffers from residual stress.

5.5 Discussion and outlook

Growths of an Fe_3O_4/InAs structure have only been reported by Preisler *et al.* [175] and Ferhat and Yoh [174] up to now. Both studies presented remarkably different results and, consequently, interpretations.

Ferhat and Yoh [174] report that magnetite grows pseudomorphic and in step-flow growth mode on an As-stabilized (2×4)-InAs(001) surface. They found an epitaxial relationship of $Fe_3O_4(001)[110] \,\|\mathrm{InAs}(001)[100]$ which corresponds to an in-plane rotation of the magnetite layer by 45° and minimizes the lattice-mismatch to $-1.6\,\%$, as has been explained above and sketched in Fig. 6.2. Surprisingly, the magnetic properties were found to be bulk-like with fast saturation behavior and bulk-like moments, both of which was interpreted as sign of a reduced APB density due to step-flow growth mode. Unfortunately, data on the chemical nature of the interface were not provided in that publication.

In opposition, Preisler *et al.* [175] found that PLD-grown magnetite has the epitaxial relationship $Fe_3O_4(110)[\bar{1}10] \,\|\mathrm{InAs}(001)[110]$. This relationship is highly unexpected since both lattices do not match up because of their different symmetries, viz. cubic and

rectangular. Their XPS results indicated a small fraction of indium oxide but no arsenic oxide in the case of growth on the As-stabilized $c(4 \times 4)$-InAs(001) surface.

In comparison, the lack of clear LEED patterns and the STEM results suggest polycrystalline quality of the films presented in this thesis. According to the general trend for epitaxy, improved growth results should be obtained at higher growth temperature since this promotes larger surface diffusion and better crystallization of the growing iron oxide. On the other hand, the crystalline quality certainly is also connected to the amount and crystallinity of the oxidic arsenic and indium phases. The amount of these phases, however, was shown to increase with growth temperature (cf. Sec. 5.3). In fact, the growth temperature used by Ferhat and Yoh was 300°C and is comparable to the ones employed here. Hence, an increase of the growth temperature might not be the key to improve the quality of Fe_3O_4 films.

Instead, it is conceivable that usage of an As-stabilized InAs surface with terrace widths in the micrometer regime in lieu of an In-rich surface critically influences the growth characteristics towards monocrystalline epitaxy. The presence of large terraces and polyatomic steps is known to favor step-flow growth mode. The specific surface reconstruction as well as the orientation and interaction of semiconductor dangling bonds with oxygen bonds could dictate the epitaxial orientation similar to the case of CeO_2 on Si(001) [179–181]. If this condition of bond orientation at the interface is not unique, e.g., in case of differently oriented domains of the reconstructed InAs surface, several differently oriented nuclei would coexist during growth, which finally would lead to polycrystalline films. According to these suggestions a more stringent control of the substrate surface with respect to reconstruction and morphology is desirable. Ultimately this would necessitate the use of connected semiconductor and oxide MBE growth chambers.

Another feasible pathway towards monocrystalline Fe_3O_4/InAs structures could be the optimization of the growth of an initial, elemental Fe layer and usage of a postoxidation procedure. Very likely this would lead to results similar to GaAs substrates (see chapter 6) with the associated properties such as intermixing at the Fe/InAs interface and the remainder of an Fe layer near the interface. First tests had shown that elemental Fe films on InAs grown at room temperature were not epitaxial, which could be linked to the large epitaxial mismatch of 5.4 %. However, as a matter of fact, epitaxial growth of Fe on InAs was demonstrated for an elevated growth temperature of 175°C in the literature [182].

6 Fe and Fe oxide thin films on GaAs

GaAs is ranked among the most interesting materials to use as the semiconducting channel in a spintronic device. Firstly, GaAs is the second-most widely used semiconductor besides Si. It has a high electron mobility and a direct band gap which predestines it for usage in electro-optical devices. Moreover, an injection efficiency of 90 % for a spin-polarized current into GaAs has already been demonstrated in 1999 by means of a BeMnZnSe spin aligner [183]. Spin injection into GaAs has been implemented by use of a Schottky barrier as well as a tunneling barrier up to now. Furthermore, a spin-diffusion length of several micrometers inside GaAs was verified [14].

6.1 Surface structures

6.1.1 Clean GaAs surface

The preparation of a GaAs template for epitaxy consists of two steps, viz. the removal of the natural oxide layer and annealing to reduce structural defects. Two recipes were followed in this work. For the first recipe, epitaxially grown GaAs layers with an additional amorphous As capping layer were provided by the III-V semiconductor group at the Chair for Experimental Physics 3 of the University of Würzburg. It was possible to blow off the amorphous As capping layer together with the topmost oxide layer at a temperature of approximately 350°C *in situ* immediately before growth. For the second recipe, blank commercial GaAs wafers (Wafer Technology Ltd.) were treated by an etching procedure consisting of *ex situ* wet-chemical etching with highly-concentrated sulphuric acid plus deionized water rinsing both under flow conditions and *in situ* Ar^+ sputtering. It was found in the course of experiments that the wet-chemical etching step shortens the ion-sputtering step, but is not absolutely necessary to fully remove the contaminations and the oxide layer.

After ion etching and annealing at temperatures up to 540°C, the GaAs surface is present in a slightly Ga-rich state as derived from PES measurements (cf. Sec. 6.3) and typically shows a (4×1) or a (4×6) reconstruction. Surfaces of the decapped GaAs-substrates treated without etching but solely by annealing are either As- or Ga-rich depending mostly on annealing conditions and display either (1×1) or (1×4) unit cells. Figure 6.1 shows a LEED pattern of the (4×6)-reconstructed Ga-rich GaAs(001)

surface (cf. Ref. [184]). The ×6 fractional order is clearly visible as individual spots, but the 4× reconstruction in the $[1\bar{1}0]$ direction is streaky indicating one-dimensional disorder. A similar disorder phenomenon was explained by Larsen and Chadi [185] for the As-stabilized surface with $c(2 \times 8)$ [or (2×4)] domains which are shifted against each other by half a unit cell in $[1\bar{1}0]$ direction.

According to Ohtake [186], the Ga-rich surface shows a (6×6) reconstruction and a $c(8 \times 2)$ reconstruction in the temperature range from 450 to 580°C and 600 to 680°C, respectively. Furthermore, the intrinsic, single-domain (4×6) reconstruction can only be obtained by deposition of 0.15 monolayer of Ga onto the Ga-rich (6×6) surface at 500°C, but not by exclusive annealing. However, if the surface with $c(8 \times 2)$ reconstruction is cooled down with a moderate cooling rate of about 1°C/s, the surface exhibits coexistence of $c(8 \times 2)$ and (6×6) phases, which is detected by electron diffraction as a (4×6) reconstruction.

Moosbühler *et al.* [187] argue that sputter-annealed (and previously uncapped) surfaces are Ga-rich and possess either (4×2) symmetry or (2×6) symmetry for final anneal temperatures of 600 and 500°C, respectively. For an intermediate temperature of 550°C, the surface exhibits domains with both phases whereby electron diffraction indicates a (4×6) reconstruction.

Based on the preceding arguments from literature the surface showing the LEED pattern in Fig. 6.1 features coexisting $c(8 \times 2)$ [or (4×2)] and (6×6) [or (2×6)] phases with one-dimensional disorder boundaries within $c(8 \times 2)$ [or (4×2)] domains.

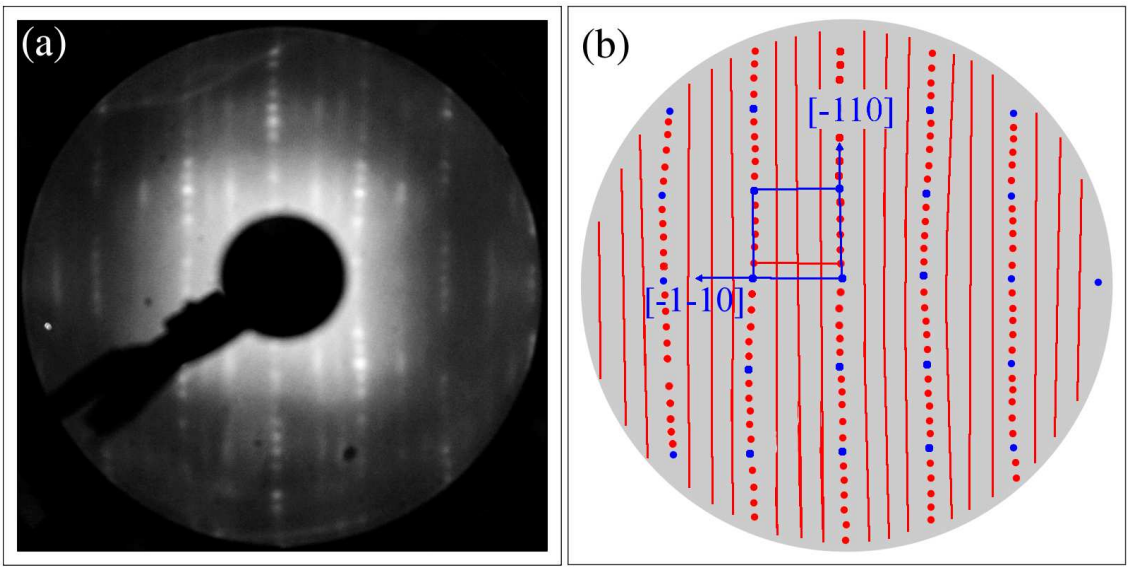

Figure 6.1: *(a) LEED pattern of a reconstructed, Ga-stabilized* (4×6)*-GaAs(001) surface with one-dimensional disorder lines taken with* $E = 61.2\,eV$*. (b) Sketch of the LEED pattern indicating the* (1×1) *spots and unit cell (blue) as well as the surface reconstruction (red).*

6.1.2 Fe on GaAs

Epitaxial growth of Fe on GaAs(001) has been demonstrated in various publications and is possible mainly due to the good lattice match between the Fe(001) and GaAs(001) planes. Assuming that four unit cells of bcc Fe grow on one unit cell of GaAs, the lattice mismatch is only +1.4 %. As can be seen in Fig. 6.2 the epitaxial relationship is Fe(001)[100] ‖GaAs(001)[100] in this case. The LEED pattern in Fig. 6.3 demonstrates the epitaxial quality of a typical grown Fe film and confirms this proposed relationship (the orientation of the GaAs substrate is the same as in Fig. 6.1). The square lattice constant determined from this and similar patterns is 2.86 ± 0.03 Å. With the given error of the LEED measurements it is not possible to distinguish unambiguously between a fully pseudomorphic (2.86 Å) and a relaxed Fe layer (2.83 Å). However, the value seems to be in better agreement with pseudomorphic growth.

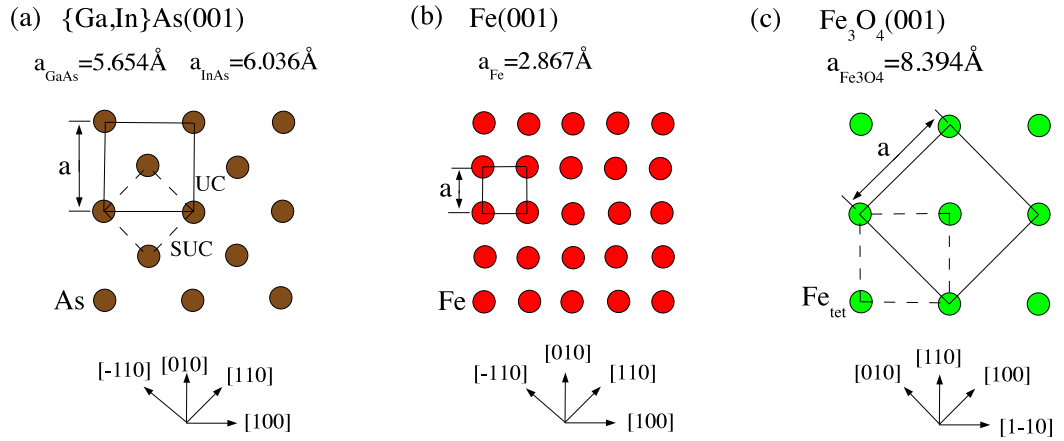

Figure 6.2: *Epitaxial relationship of Fe_3O_4 and Fe on GaAs or InAs. The projected bulk unit cell (UC) and the surface unit cell (SUC) are drawn as full and dashed lines, respectively. (a) Atomic order at the (001) surface of GaAs and InAs. The As sublattice is displayed, but the Ga or In sublattice exhibit the same symmetry. (b) Atomic order of Fe in the bcc Fe(001) surface. (c) Atomic arrangement of the Fe_{tet} ions at the Fe_3O_4(001) surface. Cf. Ref. [188].*

An effect of the specific GaAs surface reconstruction (As-stabilized or Ga-stabilized), which is a result of different preparation recipes as described above, on the structural properties of the Fe film was not observed. As is known from literature, the growth mode of Fe on GaAs(001) depends on the substrate reconstruction and temperature, and is, e.g., three-dimensional on Ga-rich $c(8 \times 2)$-GaAs(100) with islands coalescing above four monolayers [189] or predominantly layer-by-layer on As-rich (2×4)-GaAs(100) [190]. It is therefore assumed that the presented Fe layers, exhibiting typically thicknesses of several nanometers, are not island-like, but coalesced.

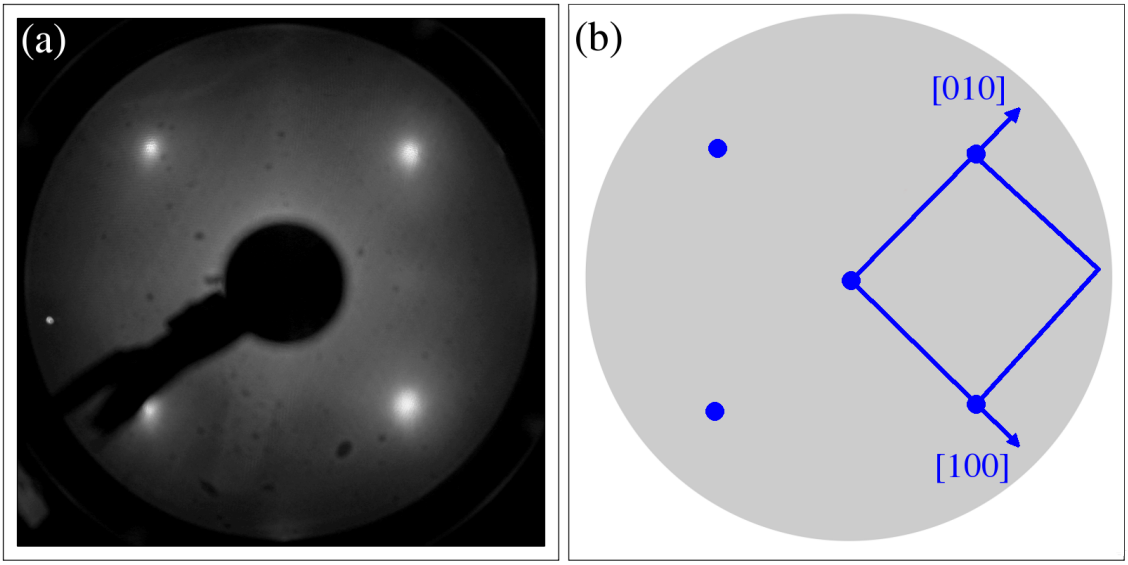

Figure 6.3: *(a) LEED pattern of an epitaxial Fe film of 2 nm thickness on GaAs taken with $E = 61.2\,eV$. (b) Sketch indicating the (1×1) spots, unit cell, and crystal direction of Fe (blue). The crystal directions of GaAs are the same.*

6.1.3 Fe_3O_4/GaAs film

Epitaxial Fe films on GaAs can be transformed into magnetite by a postoxidation procedure as was first demonstrated by Lu *et al.* [188]. Figure 6.4 displays a LEED pattern of an epitaxial Fe_3O_4 film fabricated by postoxidation annealing of an Fe film with an initial thickness of 4 nm in a molecular oxygen partial pressure of $p(O_2) = 5 \cdot 10^{-5}$ mbar at 300°C. The square lattice constant determined from this pattern yields 6.03 ± 0.08 Å which is roughly in agreement with a bulk-truncated $Fe_3O_4(001)$ square lattice of 5.94 Å size. From the LEED pattern alone, it can hardly be excluded that the surface corresponds to γ-$Fe_2O_3(001)$, which would show a lattice constant of 5.89 Å, if bulk-truncated.

Evaluation of the lattice constant for a set of growths and LEED measurements yields a lattice constant systematically larger by roughly 0.1 Å than the bulk value for magnetite. Since the epitaxial influence of the GaAs substrate or the initial Fe layer onto Fe_3O_4 is compressive, i.e., $a_{film} > a_{sub}$, this is an unexpected result. A reasonable explanation could be the crucial occurrence of an FeO layer at the early oxidation stage or as deeper-lying layer at the interface, which causes tensile, i.e., $a_{film} < a_{sub}$, behavior. Summing up, the magnetite films on GaAs are slightly tetragonally distorted, i.e., expanded in-plane by about 1.5 % (LEED) and contracted out-of-plane by −0.6 % (as derived from XRD, not shown here). As can be seen in Fig. 6.2 the epitaxial relationship between Fe_3O_4 and GaAs is $Fe_3O_4(001)[110] \parallel GaAs(001)[010]$, which corresponds to an in-plane rotation of the magnetite(001) face with respect to GaAs by 45°.

The LEED pattern is due to a (1×1), i.e., bulk-truncated Fe_3O_4, unit cell. However, a $(\sqrt{2} \times \sqrt{2})R45°$-reconstructed $Fe_3O_4(001)$ surface is typically observed for single crys-

tals [191] or thick films [22]. On our Fe_3O_4/GaAs samples and also in literature reports of such samples [188, 192] this reconstruction has never been found. Since this reconstruction is attributed to be the mechanism responsible to cancel the surface polarity, its absence in the present case could be due to the relatively small film thickness or due to surface contamination [22]. Furthermore, XPS reveals (cf. Sec. 6.3) that due to the postoxidation recipe the surface is always slightly Fe^{3+}-rich and as such resembles a γ-Fe_2O_3 surface, which inherently does not show a $(\sqrt{2} \times \sqrt{2})R45°$ reconstruction [104].

Referring to the initial Fe layer or the O sublattice common to all iron-oxide surfaces, the observed unit cell has to be labeled as a (2×2) reconstruction. Interestingly, in LEED patterns of not properly postoxidized Fe films it was observed that these (2×2) spots were missing and only a (1×1) unit cell corresponding to the O sublattice remained. To obtain such LEED patterns, atomic long-range order of the O sublattice is sufficient, while the Fe sublattice is not adequately ordered, which is ascribed to the off-stoichiometry of the surface. Such surfaces are therefore either an Fe layer with adsorbed O or an FeO-like layer.

The LEED pattern in Fig. 6.5 resembles the one in Fig. 6.4 but exhibits sharper contrast. It was obtained on a film grown by codeposition of Fe and O onto an Fe_3O_4/GaAs seed layer, following the method applied by Taniyama *et al.* [193]. This procedure opens up the possibility to grow magnetite films on GaAs which are several nanometers thick.

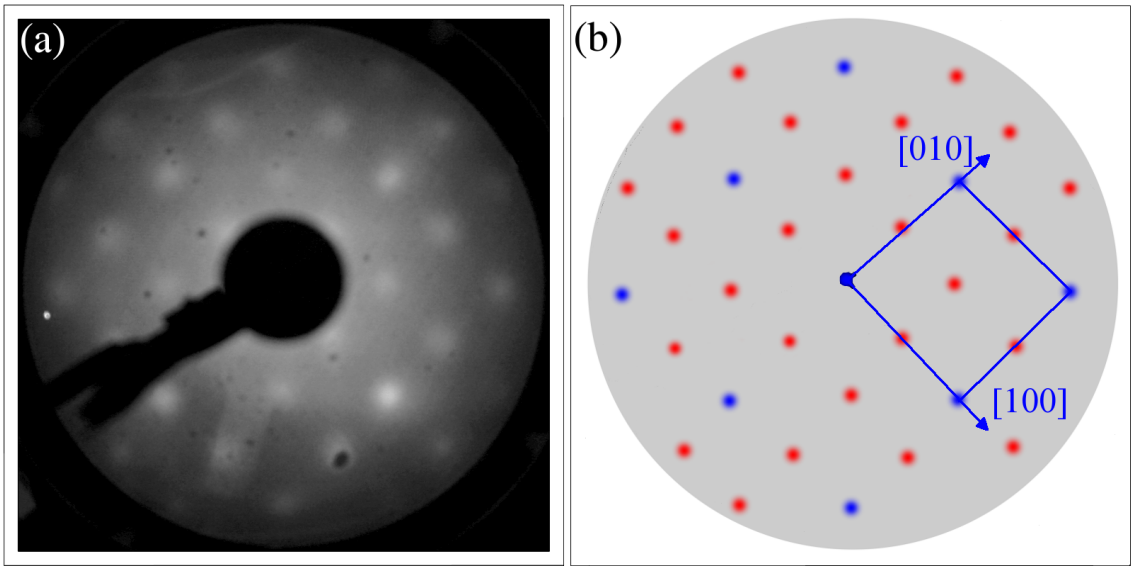

Figure 6.4: *LEED pattern of an epitaxial Fe_3O_4 film fabricated by postoxidation of a 4 nm thick Fe film on GaAs in $p(O_2) = 5 \cdot 10^{-5}$ mbar (sample no. 17). $E = 72.4$ eV. The blue (1×1) unit cell corresponds to the O sublattice. The (2×2) unit cell (red dots) corresponds to the Fe sublattice in the oxide and shows a lattice constant of 6.03 ± 0.08 Å indicative for magnetite.*

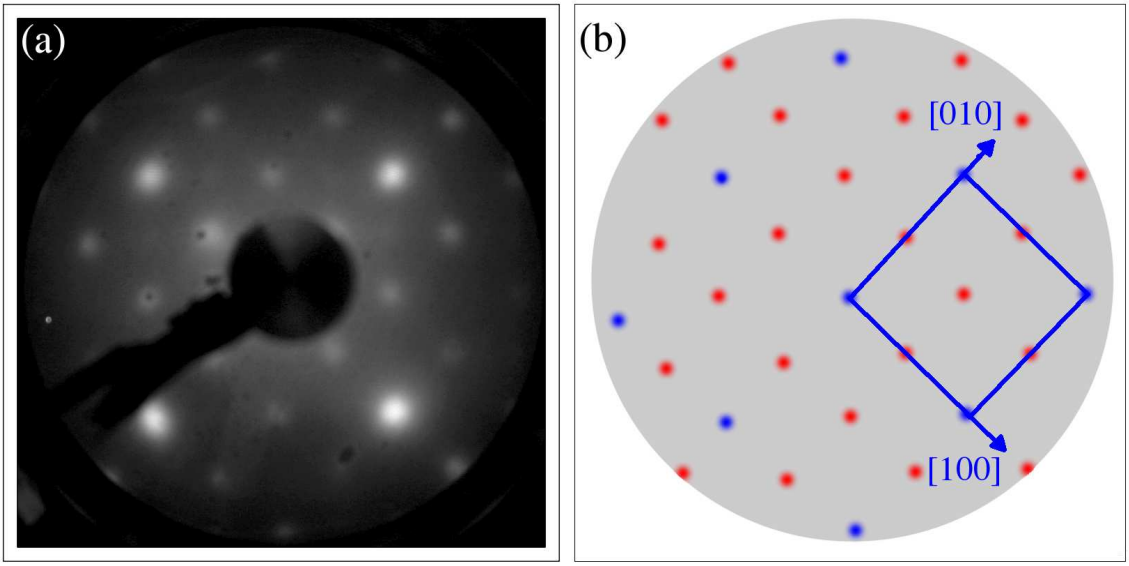

Figure 6.5: *LEED pattern of an epitaxial Fe_3O_4 film grown by codeposition of Fe and O on a thin Fe_3O_4/GaAs seed layer (sample no. 18). $E = 60.3\,eV$.*

6.2 Microstructure

Figure 6.6 shows a STEM micrograph and its according electron diffraction pattern of an Fe_3O_4/GaAs film[1]. The incoming electron beam was along the [110] direction of the GaAs substrate for both measurements.

So-called 'dumbbells', i.e., elongated features each consisting of a pair of an As and a Ga atom, are clearly resolved in the substrate region of the STEM image in Fig. 6.6(a). At the interface, an approximately 3.5 nm thick layer is visible, which appears bright in the HAADF mode. The bright contrast suggests that this layer consists of a high density of atoms with large atomic number, Z. As will be thoroughly discussed in the following and in Sec. 6.3.3, the layer consists of elemental Fe and is a remainder after the postoxidation procedure. The actual Fe_3O_4 layer is located on top of this interface layer, and a post-growth deposited Pt layer caps the magnetite surface.

The electron diffraction pattern in Fig. 6.6(b) allows to extract the epitaxial relationship of the whole structure. From a simulation of the diffraction pattern the epitaxial relationship $Fe_3O_4(001)[110] \parallel GaAs(001)[010]$ can be derived, which is in accordance with the LEED results. The Fe interface layer is not sufficiently thick to contribute to the diffraction pattern. Diffraction on the amorphous Pt layer causes the ring-like structure centered around the origin. The diffraction spots of GaAs are distinctly brighter than the ones of magnetite. GaAs diffraction spots lie on the blue lines and equivalent lines as indicated, while diffraction spots from magnetite are marked by the orange line.

[1]The STEM and diffraction measurements were performed by Dr. M. Kamp at the Chair for Applied Physics of the University of Würzburg.

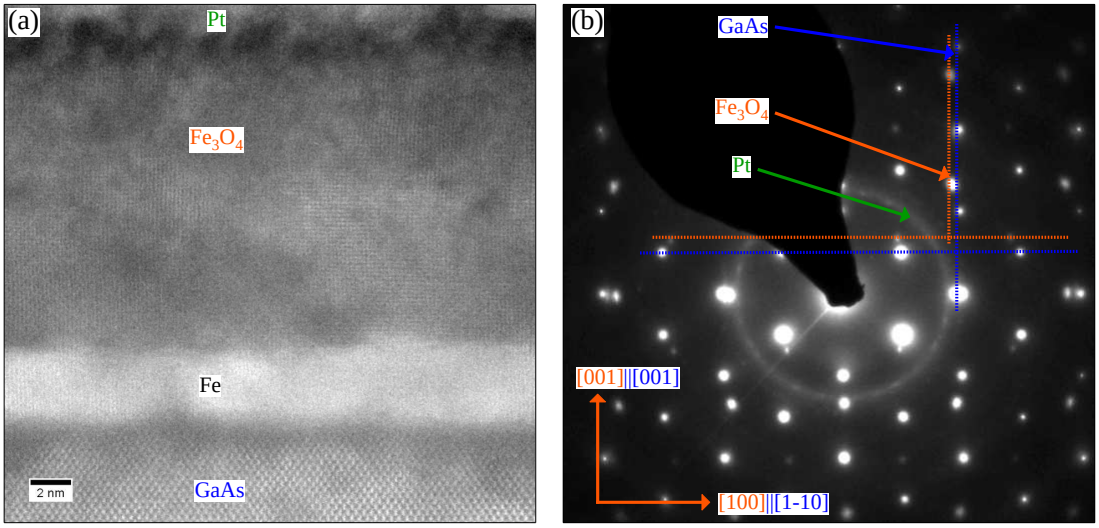

Figure 6.6: *(a) STEM image and (b) electron diffraction pattern of an epitaxial Fe_3O_4 film grown by codeposition of Fe and O on a thin Fe_3O_4/GaAs seed layer (sample no. 18).*

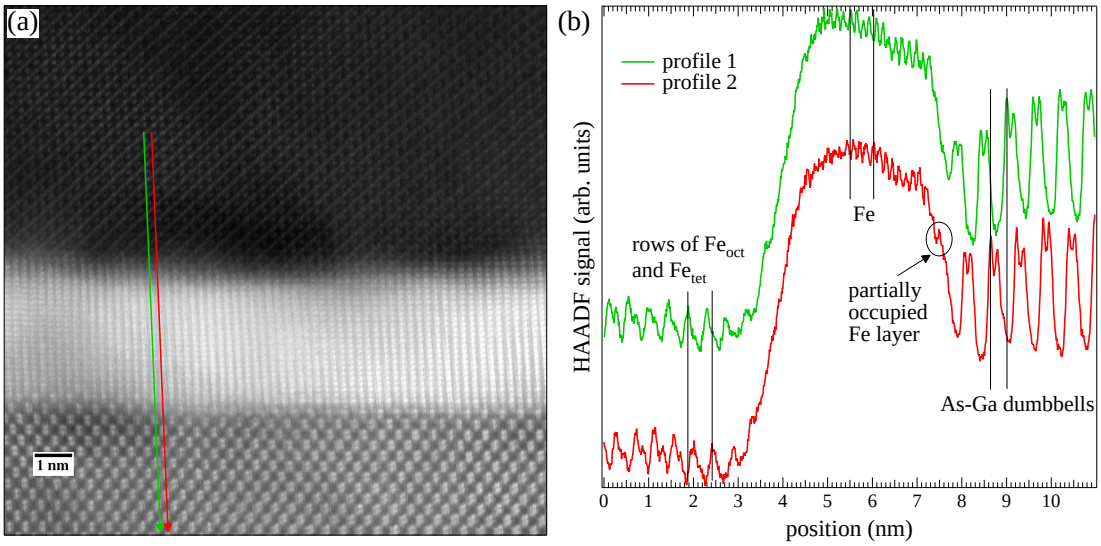

Figure 6.7: *(a) STEM image and (b) HAADF profiles of Fe_3O_4/Fe/GaAs interfaces (sample no. 18). The atomic corrugation is due to rows of Fe ions, due to Fe atoms, and As-Ga dumbbells inside the Fe_3O_4, the Fe, and the GaAs layer, respectively. The atomic corrugation in both profiles is shifted against each other.*

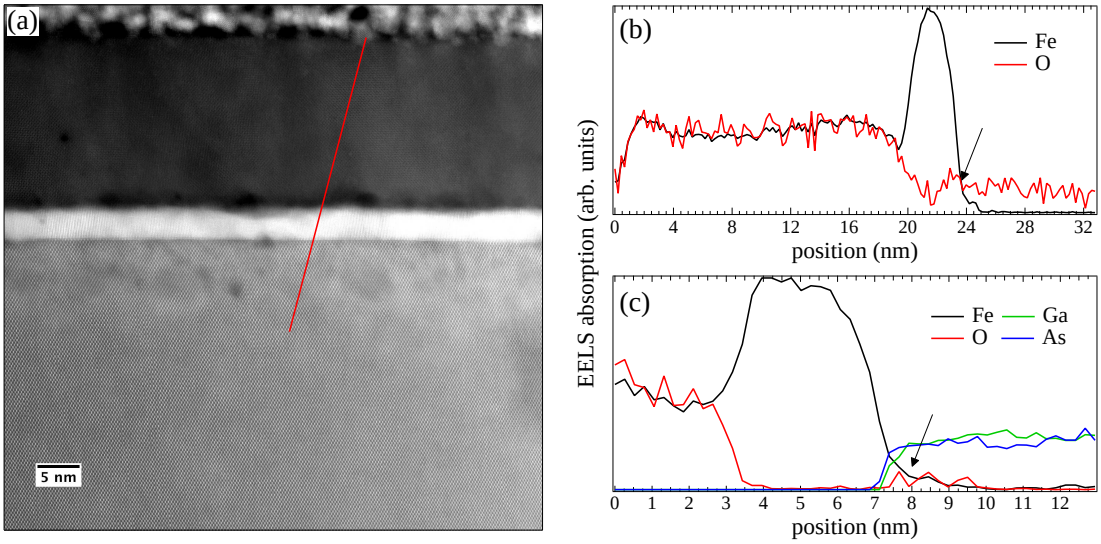

Figure 6.8: *(a) STEM image and (b) and (c) EELS absorption profiles of an Fe_3O_4/Fe/GaAs film (sample no. 18). The profile in (b) is indicated by the red line in image (a).*

All three layers—GaAs, Fe, and magnetite—exhibit clear atomic contrast in the high-resolution images[2] displayed in Fig. 6.7. The atomic structure of the Fe layer consists of columns of Fe atoms as seen from the [110] direction of bcc Fe. The atomic contrast of the HAADF line profile along such a column is due to single Fe atoms. The corrugation in the magnetite layer is due to rows consisting of Fe_{oct} and Fe_{tet} ions with a distance between neighboring rows of $a/\sqrt{2}$. These rows run diagonally from the lower left to the upper right, i.e., along an $Fe_3O_4[011]$ direction, without any phase shift. This means that no APB is observed in this area. However, APBs with a phase shift vector out of the $1/2\langle 100\rangle$ or the $1/4\langle 110\rangle$ family of directions would be visible only if the phase shift were not along the row direction and not along the electron-beam direction. Moreover, for a sufficiently thin cross section of the sample only one APD will be left in the imaged area and hence no APB can be found even if the phase shift vector is in principle observable. Between these rows of Fe ions other Fe_{tet} ions are imaged. Together all of the Fe_{tet} ions form a square mesh (cf. Fig. 6.2). At the very Fe/GaAs interface a partially occupied Fe plane between the terminating As plane and the first fully occupied Fe layer is present (see note in Fig. 6.7) in full accordance with the interface model of LeBeau *et al.* [194]. The partially ($1/4$) occupied Fe layer corresponds to Fe atoms replacing Ga atoms in the last GaAs dumbbell, which would be seen if the structure were imaged from the $Fe_3O_4[1\bar{1}0]$ direction (not done here).

All interface roughnesses are quite small in the imaged area. Especially the interface between GaAs and Fe is surprisingly abrupt (below 1 nm in Fig. 6.8). A discussion

[2]The STEM and EELS measurements were performed in the group of Dr. Jo Verbeeck at the Institute for Electron Microscopy for Materials Research of the University of Antwerp.

of the intermixing as seen by a change of the chemical environment in PES is given in Sec. 6.3. In the STEM images shown here the observed intermixing between the Fe layer and GaAs is very small. This is also evident from the EELS absorption profile given in Fig. 6.8(c). While the Ga and As signals decrease sharply at the interface and become exactly zero inside the Fe layer, a small Fe and, to a greater extent, an O signal persist in the GaAs layer (see arrows in Figs. 6.8(b) and (c)). It is possible that some of the O diffuses into the GaAs layer or occupies vacancies of the partial Fe layer. The bonding of O with Ga and As was also detected in the PES spectra of samples with different film and interface layer thicknesses (see Sec. 6.3.3).

The interface between Fe_3O_4 and elemental Fe layer is somewhat less defined and shows a roughness of 1 to 2 nm. The position and the roughness of this interface probably depend on the applied postoxidation parameters. From the atomically resolved STEM image in Fig. 6.7 it can, however, be concluded that no additional third phase such as FeO is existent.

The interface roughnesses and thicknesses of the single layers were also determined by a simulation of XRR data taken on the same sample as investigated by STEM. As can be seen in Fig. 6.9 the respective values are in agreement with the STEM investigation. The XRR confirms again that the interface layer consists of elemental Fe and not of a different iron oxide, e.g., FeO. A reasonable agreement between simulation and the experimental curve could only be obtained with the optical data for elemental Fe.

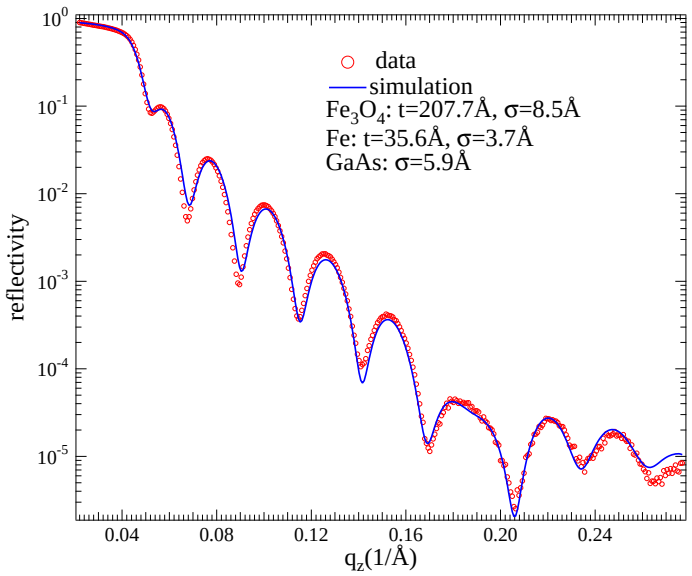

Figure 6.9: *XRR data and simulation of an Fe_3O_4/Fe/GaAs film (sample no. 18). The experimental data were simulated with the software "ReMagX" [136] in order to obtain the indicated fit parameters: film thickness $t_{Fe_3O_4}$, surface roughness $\sigma_{Fe_3O_4}$, elemental Fe layer thickness t_{Fe} and roughness $\sigma_{Fe_3O_4}$, and interface roughness σ_{GaAs}. The fit parameters of the simulation, are in agreement with the STEM observations.*

6.3 Investigation by photoelectron spectroscopy

6.3.1 Surface composition studied by extreme ultraviolet photoelectron spectroscopy

The following two Secs. 6.3.1 and 6.3.2 comprise results of EUPS and spin-resolved PES measurements of clean and postoxidized Fe/GaAs films, which were conducted at beamline U5UA at the National Synchrotron Light Source in Brookhaven. Firstly, the analysis of the chemical structure of these films at various preparation steps is presented. The shown spectra were taken with a resolution of approximately 150 meV and photon energies of 44 to 126 eV, which are settings optimized for high photoionization cross sections and a high surface sensitivity of the spectra ($\lambda \approx 5$ Å).

Figure 6.10 displays EUPS survey spectra which illustrate the main changes after respective preparation steps of Fe/GaAs thin films. The spectrum taken on an As-capped GaAs wafer consists of an elemental As 3*d* peak at 41.7 eV as the signal of the As capping and an arsenic-oxide peak at 44.5 eV, which indicates an additional arsenic-oxide layer (see also Tab. 6.1 for spectral intensities). Unexpectedly, there is also a Ga 3*d* peak present in the spectrum, although it is considerably less intense (the chemical ratio of As/Ga is roughly 2) than for a clean GaAs surface. The peaks at 19.3 eV and 20.5 eV binding energy are the signal of Ga segregated into the As capping layer and gallium oxide residing presumably on the top of the film, respectively. The amorphous As capping layer is several hundreds of nanometers thick, and therefore it can be safely excluded that the substrate is probed by EUPS measurements. The As capping layer protects the clean substrate from oxidation but is itself oxidized at its surface during storage at atmospheric oxygen pressure. In comparison with a clean substrate, both As and Ga 3*d* core-level spectra are shifted to higher binding energies most probably due to electric charging of the amorphous As capping layer. Secondly, Ga is incorporated in the As layer as an impurity and therefore each Ga atom is bound in a chemical environment with several As atoms resulting in a higher binding energy compared to the usual Ga-As bond (see Fig. 6.10).

Table 6.1: *Relative chemical composition (in %) of iron oxide on GaAs at various stages of fabrication inferred from intensities of core-level spectra. As $3d_{int}$ and Ga $3d_{int}$ are the intrinsic spectral weights.*

	As $3d_{int}$	As $3d_{oxide}$	Ga $3d_{int}$	Ga $3d_{oxide}$	O $2s$	Fe $3p$
As-capped GaAs	50.7	15.9	24.8	8.5	0	0
clean GaAs	48.3	0	51.7	0	0	0
Fe (30 Å)	54.4	0	1.6	0	0	44
Fe (78 Å)	4.2	0	0	0	0	95.8
1× postoxidized	0	0.2	0	0.9	73.6	25.3
2×postoxidized	0	0.3	0	0	77.1	22.7

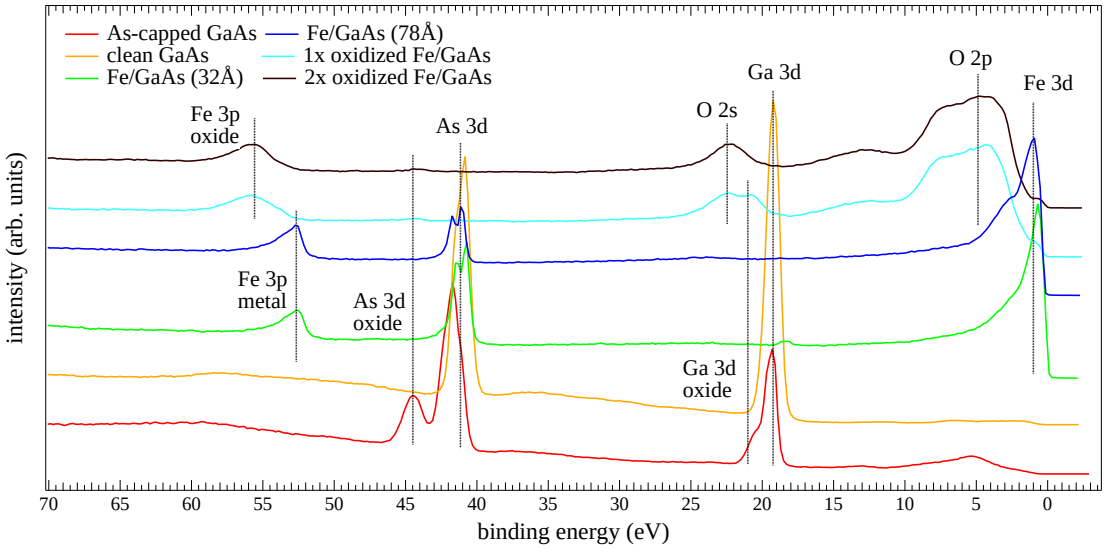

Figure 6.10: *EUPS survey spectra of iron oxide on GaAs at various stages of fabrication. The As-capped GaAs wafer, clean GaAs surface after several sputter-annealing cycles, 32 Å Fe deposited on GaAs, 70 Å Fe deposited on GaAs, Fe/GaAs postoxidized in* $p(O_2) = 2.67 \cdot 10^{-6}$ *mbar for 10 min, Fe/GaAs further postoxidized in* $p(O_2) = 4.93 \cdot 10^{-5}$ *mbar for another 10 min (sample no. 19).*

After an *in situ* cleaning procedure, which consisted of As decapping through thermal desorption and several sputter-annealing cycles, both oxide components and the elemental As component peaks vanish and are replaced by two intrinsic GaAs-derived peaks. Also, the VB structure becomes less intense because of the lack of the O 2*p* derived states. The As/Ga intensity ratio, which is strongly dependent on the atomic details and thermochemical history of the specific surface under study, varied between 0.54 and 1.08 for different cleaned surfaces. Compared with the As/Ga ratio obtained in earlier works with similar substrates [195, 196] the present values are relatively small indicating a Ga-rich surface status.

The deposition of Fe shows up in the appearance of Fe 3*p* levels at a binding energy of 52.7 eV and Fe 3*d* levels in the VB. After deposition of about 32 Å of Fe the As signal has considerably decreased, but still is clearly visible. It is not an As signal from the substrate which is simply obvious by comparison with the intensity of the Ga level. In several studies in the literature it was established that some monolayers of As are released from the GaAs substrate and subsequently segregate to the surface during the deposition of Fe ([189, 196, 197]). A smaller amount of the released As remains, however, near to the interface. At this Fe film thickness of 32 Å a marginal Ga 3*d* intensity is additionally visible which according to Thompson *et al.* is near-interface resident Ga [196]. This 'reacted' Ga making up a mixed interface layer of about 9 Å thickness is still visible in the PES signal because of the relatively small Fe overlayer thickness. In contrast, after the deposition of 70 Å of Fe, this Ga signal has completely vanished, but

the As signal has not, although the latter is further reduced compared to the case of smaller Fe film thickness (see Tab. 6.1). This and the fact that the As is converted into a very small arsenic oxide component after the oxidation step are further evidence for the residence of the As at the surface.

The postoxidation of a 70 Å thick Fe film in $p(O_2) = 2.67 \cdot 10^{-6}$ mbar at 260°C for 10 min results in a shift of the Fe 3*p* core level to 55.6 eV and the appearance of the O 2*s* core level at 22.4 eV. Besides, a Ga 3*d*-oxide level at 20.8 eV becomes visible presumably due to surface-segregated and subsequently oxidized Ga. In the VB a clear change from the intensive Fe 3*d* metal states to hybridized Fe 3*d*-O 2*p* states is observed. Here, the cross section of O 2*p* dominates in contrast to Fig. 3.9. Another postoxidation step in $p(O_2) = 4.93 \cdot 10^{-5}$ mbar at 260°C for 10 min does not change the spectrum strongly, but the spectral intensities in Tab. 6.1 indicate a continuing oxidation of the Fe film. The Ga 3*d*-oxide level vanishes again, and the Fe 3*d* level decreases further in intensity. The small As 3*d*-oxide component essentially is not changed.

Figures 6.11 displays the EUPS As 3*d* and Ga 3*d* spectra corresponding to the above explained preparation steps. The As 3*d* spectrum of the As-capped wafer shows a broad

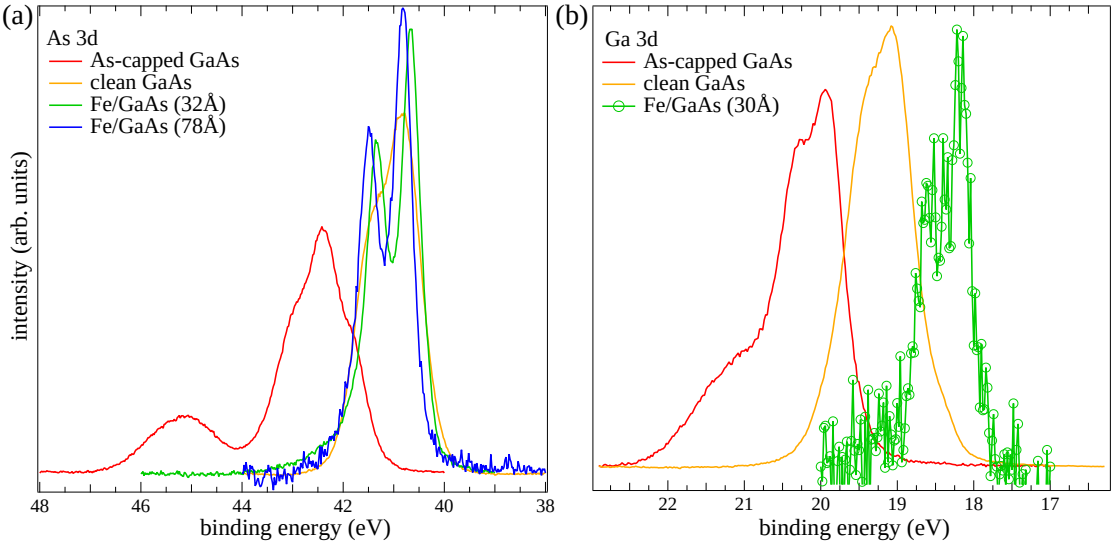

Figure 6.11: *(a) As 3d and (b) Ga 3d EUPS spectra of Fe on GaAs at various stages of fabrication. The As-capped GaAs wafer, clean GaAs surface after several sputter-annealing cycles, Fe deposited on GaAs (sample no. 19).*

arsenic-oxide peak at about 45 eV binding energy and a peak characteristic for elemental As at about 42.5 eV. This elemental As peak also is composed of various components due to several chemical environments as can be seen by the absence of the typical intensity ratio for spin-orbit split components and shows a broad shoulder at about 41.5 eV. Both Fe/GaAs films show spectra typical for reacted As residing at the surface of the Fe film. The overall spectrum consists of the spin-orbit split components with a splitting

of about 0.7 eV and widths of about 0.5 eV. It is slightly shifted by −0.1 eV in binding energy with respect to the clean substrate for the 32 Å film which is in accordance with the observation of Thompson *et al.* [196]. For the larger film thickness of 78 Å, such a shift is barely observable. According to the observation of Thompson *et al.* [196], other chemical environments of As exist near to the interface with their respective spectra shifted to *higher* binding energy. However, these are not seen here because of the high surface sensitivity ($\lambda = 5.25$ Å). They would only be detected for small film thicknesses below about 20 Å. In contrast to the Fe/GaAs case, the spectrum taken on the clean GaAs substrate is a mixture of several chemical environments (surface shifted components due to reconstructed bonds) and possesses a smooth line shape with hardly visible spin-orbit splitting.

Similarly, the Ga 3*d* spectra in Fig. 6.11(b) changes quite drastically after respective preparations steps. As was already discussed above, the Ga 3*d* level lies at high binding energies for the As-capped substrate due to charging of the capping layer. It consists of Ga solved in the amorphous arsenic and gallium oxide in the topmost oxide layer. For the cleaned GaAs surface the main peak exhibits a binding energy of about 19 eV and consists of surface-shifted components besides the bulk one. After deposition of Fe a shift to lower binding energy indicative of Ga in a metallic environment is seen. It corresponds to the 'reacted' Ga near to the interface.

Figure 6.12(a) displays a sketch of the chemical composition of an Fe/GaAs(001) sample as proposed by Thompson *et al.* [196]. A reacted interface layer with an extension of about 9 Å is present after deposition of 100 Å of Fe at room temperature. Similar reactions and an interface layer thickness of about 5 Å occur for the Fe/GaAs(110) system as observed by Ruckmann *et al.* [197]. According to Chambers *et al.*, the 'reacted' Ga and As atoms reside in interstitial face-center sites of Fe [189].

The present results are qualitatively in full agreement with this picture although the quantitative information about the thickness of the interface layers can neither be confirmed nor discarded because the deposited film thicknesses are quite large. The As layer at the top of the whole film is approximately only 0.4 Å thick according to the spectral intensities from Tab. 6.2 and assuming the atomic density of elemental As. In Sec. 6.3.3 it is discussed how the annealing and the oxygen dosage during the postoxidation treatment affect the vertical chemical composition of the sample (cf. Fig. 6.12(b)).

6.3.2 Spin polarization studied by extreme ultraviolet photoelectron spectroscopy

This section comprises the analysis of the spin polarization of clean and postoxidized thin Fe/GaAs films. Experiments were performed on an Fe/GaAs structure which had been prepared as described in the last section. Spin-resolved spectra were taken in a 45° incidence and normal emission geometry by means of a Mott detector integrated in the electron-analyzer system. The angle acceptance of the electron analyzer was set

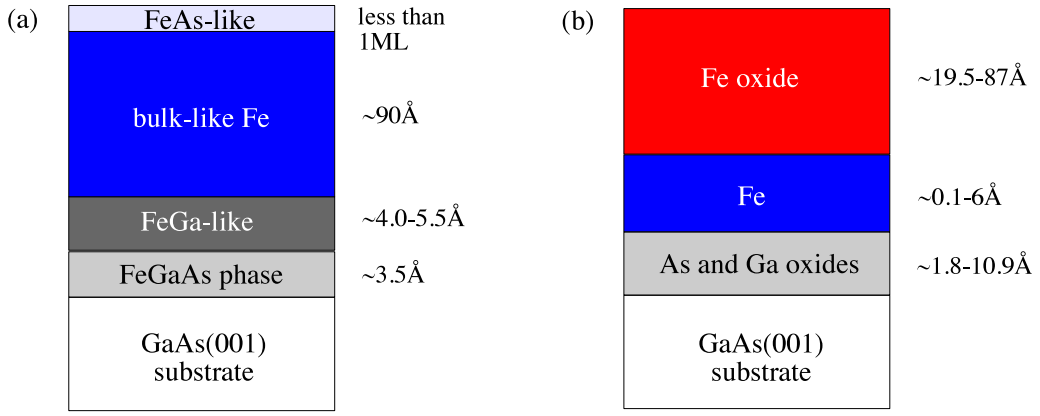

Figure 6.12: *Sketch of the vertical chemical composition of (a) 100 Å of Fe deposited on GaAs(001) at room temperature as proposed by Thompson et al. [196]. Arsenic continuously segregates to the surface and partially remains in the Fe layer. (b) Postoxidized Fe/GaAs for varying initial Fe layer thicknesses. Cf. Tab. 6.2.*

to 2°, which results in a k-resolution of 0.06 Å^{-1}. Therefore, the spectra cover only a small section of 2.7 % and 4.9 % around the Γ-point of the surface brillouin zone of Fe and Fe_3O_4(001), respectively. The photons were set to an energy of $h\nu = 44$ eV and a nearly 100 % horizontal polarization. Spectra were taken in remanent magnetization after a 2 T magnetization pulse was applied along the GaAs[100] in-plane direction, which coincides with the Fe[100] and Fe_3O_4[110] directions (see Fig. 6.2). The crystal direction was derived from the orientation of the cleaving edge of the GaAs wafer and therefore could be aligned along the magnetic field only by about ±10°. All values of the spin polarization are given for the remanent magnetization state, i.e., they do not correspond to the spin polarization in saturation.

Figure 6.13 shows that the 78 Å thick Fe layer is strongly polarized along a GaAs⟨110⟩ direction. This direction is labeled as [110] in Fig. 6.13(b), while the other curve with nearly zero polarization corresponds to a direction which is perpendicular (labeled [1$\bar{1}$0]). This means that the magnetization axis is rotated after the magnetization pulse from the [100] direction, which is also along the magnetic easy axis of bulk Fe, to a ⟨110⟩ remanent magnetization direction. Xu *et al.* and later Zhang *et al.* observed that an unidirectional easy axis along [1$\bar{1}$0] exists in the Fe/GaAs(001) system for coverages of less than 30 Å [198, 199] and that the remanent magnetization direction changes back to [100] at higher coverages. This unidirectional easy axis could also exist here.

The polarization curve in Fig. 6.13(b) indicates that the maximal polarization amounts to +75 % close to E_F and that most of the VB is polarized at values between +40 % and +60 %. These values are significantly greater than the ones usually observed for the Fe/GaAs system [199] indicating the high magnetic quality of the films. However, it has to be kept in mind that the presented measurements only show the magnetization of

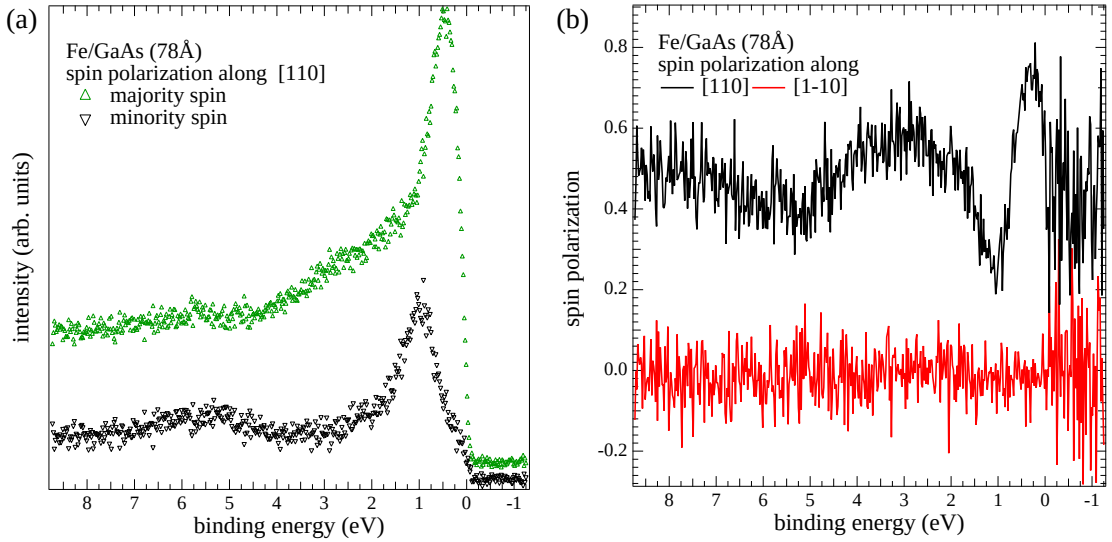

Figure 6.13: *(a) Spin-resolved VB spectra and (b) polarization of Fe/GaAs (thickness 78Å). The Fe layer is strongly polarized along GaAs*[110].

states from a small part around the Γ-point of the Fe surface brillouin zone. Note that the polarization exhibits a dip at around 1.5 eV binding energy which is a characteristic feature of the polarization of Fe films [199, 200].

Figures 6.14(a) and (b) display the spin-resolved VB and spin polarization of an Fe/GaAs layer after one postoxidation cycle, respectively. Here, the polarization is rotated by 90° in the film plane into the GaAs[1$\bar{1}$0] direction. If the layer is assumed to be completely oxidized to magnetite, this direction corresponds to the Fe_3O_4[100] direction, which is the magnetic hard axis for bulk magnetite.

The state near E_F is negatively polarized in agreement with LSDA calculations (see Sec. 2.3). According to ligand field theory this state corresponds to the $^6A_1$ multiplet final state of the Fe^{2+} ion in an octahedral crystal field. However, the magnitude of the polarization is much lower than the −100 % predicted by LSDA. It is also considerably lower than experimentally verified values of spin polarization of −40 to −55.5 % for the (001) surface [21, 201, 202] and −40 to −80 % for the (111) surface [23, 48]. The polarization is highest at 2 eV binding energy, the energetic positions of Fe 3*d*-like states, and decreases to nearly zero for the mostly O 2*p*-like states at higher binding energy (cf. VB spectra in Fig. 3.9(a)).

The spin polarization and the surface stoichiometry of the Fe_3O_4/Fe/GaAs layer as probed by EUPS was found to be best for oxygen dosages of about 1200 L or less (postoxidation in $p(O_2) = 2.67 \cdot 10^{-6}$ mbar for 10 min) in agreement with Refs. [203, 204]. On the other hand, when using more strongly oxidizing conditions, which result in a stoichiometric layer as probed by XPS, i.e., $p(O_2) = 5 \cdot 10^{-5}$ mbar for 10 min (cf. Sec. 6.3.3), the surface as probed by EUPS is presumably overoxidized and shows no spin polarization.

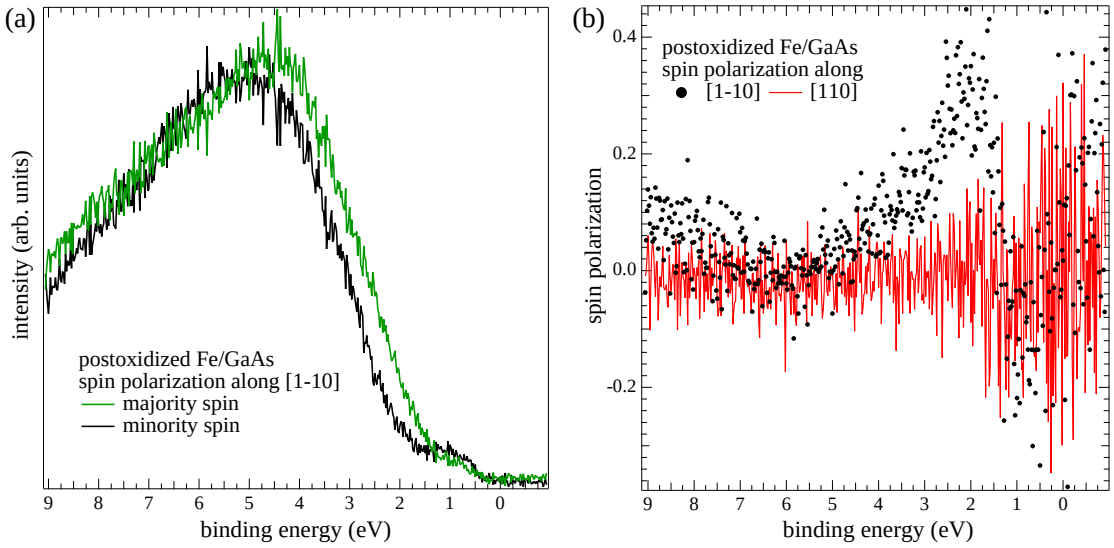

Figure 6.14: *(a) Spin-resolved VB spectra and (b) polarization of postoxidized Fe/GaAs. The iron-oxide layer is weakly polarized along GaAs*$[1\bar{1}0]$ *(sample no. 19).*

Insofar, the correct surface stoichiometry within the topmost few ångströms seems to be crucial for spin polarization measurements by EUPS. The absence of any discernible spin polarization for heavily oxidized samples could also be linked to the appearance of impurities such segregated arsenic and gallium oxides at the surface. Since EUPS is very surface-sensitive, these impurities would strongly decrease the detectable spin polarization. Additional evidence supporting this assumption is the overall structureless lineshape of the VB spectrum, which is in bad agreement with literature results (cf. Refs. [21, 201, 202]).

6.3.3 Electronic and chemical structure studied by (hard) x-ray photoelectron spectroscopy

This section deals with the chemical composition of Fe films on GaAs postoxidized to Fe_3O_4. The shown HAXPES measurements were performed at the HIKE endstation at BESSY II in Berlin in a similar manner as the measurements of films on ZnO (see Sec. 4.4). In contrast to the EUPS measurements, which probe the composition of a surface layer of only a few ångströms thickness, the spectra taken with Al-K_α radiation and hard x-rays exhibit considerably larger information depths.

Figure 6.15 displays Fe $2p$ spectra with different effective information depths taken on an Fe_3O_4/GaAs film with an additional Fe interface layer. The overall Fe $2p$ spectrum is a superposition of the broad spin-orbit split peaks at 710.5 and 724.0 eV indicative of magnetite and less intense, sharper peaks at 706.5 and 719.5 eV characteristic of elemental Fe. Comparing the spectra, it becomes obvious that the spectral weight of

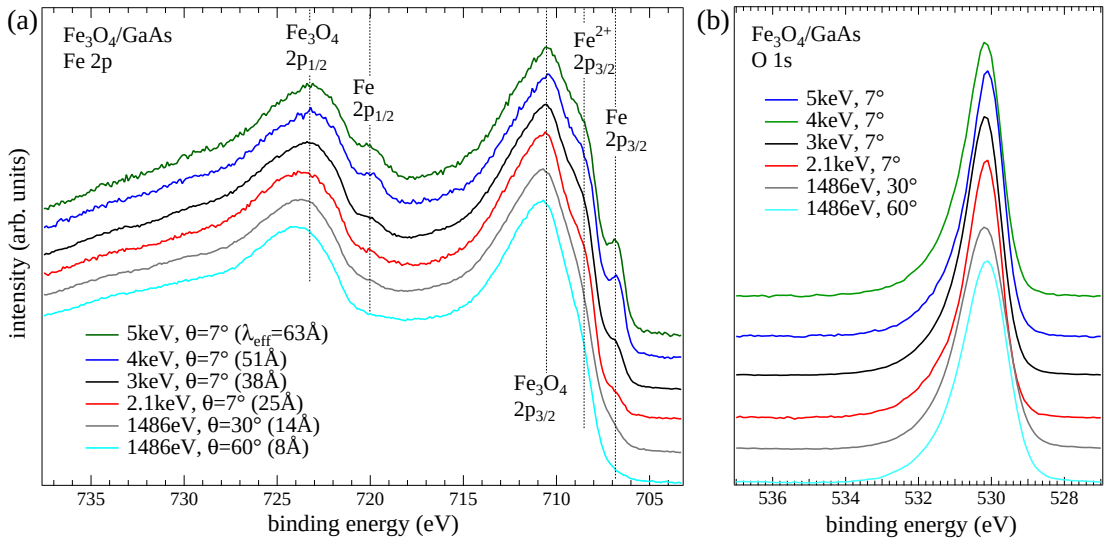

Figure 6.15: *(a) HAXPES Fe 2p spectra of an 80 Å thick Fe_3O_4/Fe/GaAs film (sample no. 20) at various photon energies and emission angles. The presence of an interfacial Fe layer is clearly revealed by the HAXPES spectra. (b) O 1s spectra taken under the same conditions.*

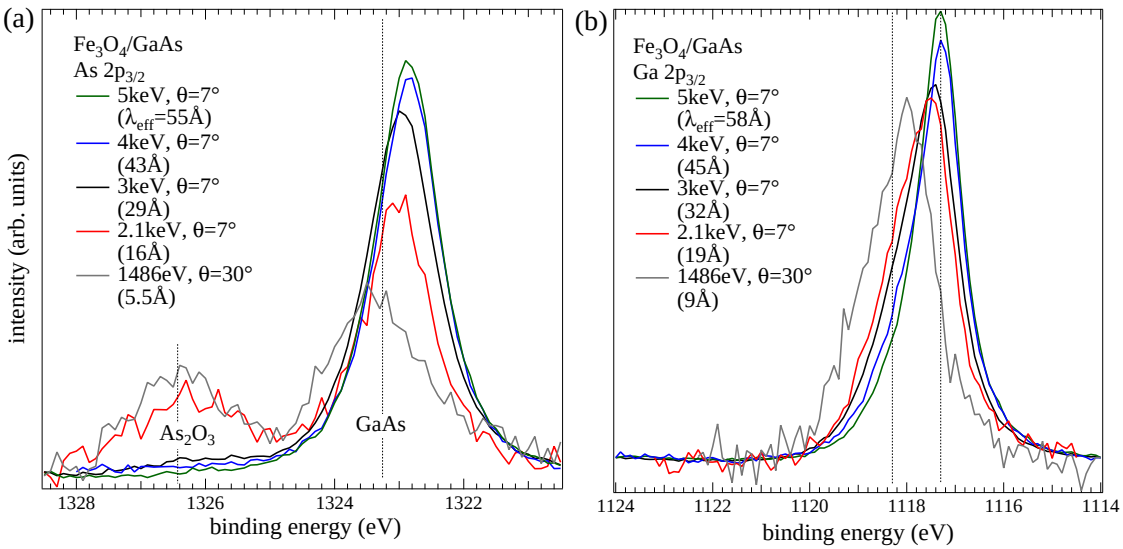

Figure 6.16: *(a) HAXPES As $2p_{3/2}$ spectra of an 80 Å thick Fe_3O_4/Fe/GaAs film (sample no. 20) at various photon energies and emission angles. (b) Respective Ga $2p_{3/2}$ spectra. All spectra are normalized to the same spectral weight.*

Table 6.2: *Relative chemical composition (in %) of an Fe_3O_4/GaAs film (sample no. 20) inferred from intensities of core-level spectra shown in Figs. 6.15 and 6.16.*

	As 2p			Ga 2p		O 1s	Fe 2p
(%)	GaAs	interfacial	oxide	GaAs	oxide		
5 keV, 7°	6.4	1.0	0	8.3	1.1	45.4	37.8
4 keV, 7°	3.3	0.5	0	4.1	1.0	56.2	34.9
3 keV, 7°	0.4	0.4	0	1.8	0.5	55.5	41.4
2.1 keV, 7°	0.1	0.1	0.1	0.4	0.1	64.3	34.9
1486 eV, 30°	0.03	0.1	0.1	0.5	0	54.0	41.9
1486 eV, 60°		0		0		54.7	40.6

the elemental Fe component is enhanced for increasing photon energy, i.e., for increasing information depth and hence interface sensitivity. On the other hand, the elemental Fe signal is suppressed in more surface-sensitive XPS spectra measured with Al-K_α radiation. This tendency strongly suggests that an elemental Fe layer is situated right at the interface to GaAs in accordance with the STEM image in Fig. 6.6 and the XRR data in Fig. 6.9. Such elemental Fe interface layer was present in most of the grown samples although its thickness varied as a result of different growth parameters.

Additionally, the shoulder at a binding energy of about 709 eV gains spectral weight for higher information depths, which indicates a larger fraction of Fe^{2+} at interface-near layers. A quantification of this increasing Fe^{2+}-content is difficult due to the similarity and broadness of magnetite and wüstite Fe 2p spectra, but qualitative comparison with HAXPES spectra in the literature [205] suggests that the actual fraction of Fe^{2+} surplus is a few percent only.

The thicknesses of the film and the interfacial layers were estimated from photoemission intensities (see Sec. 3.2.4). For this purpose the Fe 2p spectra were decomposed into their magnetite and Fe fractions and compared to the GaAs-component of the As or Ga $2p_{3/2}$ core level. Calculated layer thicknesses of different samples are summarized in Tab. 6.3.

Generally, the postoxidation procedure is expected to introduce a vertically varying oxidation profile inside the film, resulting in a high oxidation state at the film surface and lower oxidation state towards the interface. If the initial Fe layer is too thick or the oxidation conditions are too weak, an interface layer with elemental Fe remains at the interface. This behavior can be attributed to the limited permeability of the iron-oxide layer for O_2 molecules.

The Fe_3O_4 film thickness that can be produced with the described method is therefore restricted to only a few nanometers. However, higher film thicknesses beyond can, in principle, be attained with repeated Fe evaporation and postoxidation cycles or by using the first magnetite layer as a seed layer for growth by co-deposition (cf. Sec. 6.1.3). However, if the initial Fe layer is too thin or the oxidation conditions are too strong,

the film will be completely oxidized and the GaAs substrate also will become oxidized as explained below.

As $2p_{3/2}$ and Ga $2p_{3/2}$ spectra (see Fig. 6.16) indicate considerably less oxide-layer formation than observed in the Fe_3O_4/InAs system. A small arsenic-oxide component at 1325.6 eV is observed for small photon energy and hence information depth, but is strongly suppressed at higher excitation energies. This component is the signal from the oxidized, topmost layers of the GaAs substrate, of oxidized As from the FeGaAs interface phase, and the surface segregated and subsequently oxidized As (see Sec. 6.3.1). Note that all shown spectra are normalized to the same spectral weight and hence do not represent absolute intensities.

The energy-dependent depth-profiling data suggest that the small arsenic- and gallium-oxide signals originate from the interface. For the most surface-sensitive spectra the As and Ga levels are below the detection limit (see Tab. 6.2). Recall that the formation of gallium oxide is predicted by the thermodynamic consideration in Sec. 3.1.5 while the occurrence of arsenic oxide is not.

The initially grown Fe layers act as a barrier for the O_2 molecules and largely protect the substrate surface from unintentional oxidation deeper in the bulk. Oxidation of As and Ga, however, depends on the thickness, smoothness, and compactness of the initially grown Fe layer (see Sec. 6.3.1) and on the details of the postoxidation procedure such as annealing temperature and duration. For smaller initial Fe layer thicknesses the partial oxidation of As and Ga is enhanced because almost the complete Fe layer is oxidized, which, however, contains the intermixed FeGaAs phase. Therefore, some of these initially interface resident As and Ga species together with the topmost substrate layers are oxidized. Besides, the provision of thermal energy could induce a segregation of these As and Ga atoms into the remaining part of the Fe layer.

With decreasing information depth, i.e., smaller photon energy, the intrinsic As $2p_{3/2}$ and Ga $2p_{3/2}$ main peaks shift to higher binding energy. These shifts could be at first glance interpreted as a band-bending effect due to the metal layer on top of the semiconducting GaAs. However, the used substrate was a nominally un-doped GaAs buffer layer on a n(Si)-doped substrate and therefore a possible band-bending effect would shift both levels to lower binding energy. Moreover, the barrier height would be far too small (about 0.24 eV) and the width of the depletion layer too large (several tens of nanometers) to cause such a large binding-energy difference for an information depth much smaller than the width of the depletion layer [206].

This shift is therefore presumably ascribed to a larger contribution of covalently bound Fe-As and Fe-Ga to the spectra (see Sec. 6.3.1). Both, Ga and As possess several interface species with binding-energy shifts to lower *and* higher binding energies according to Thompson [196]. Thus, the stronger signal of these interface species in the spectra with higher information depth will either broaden the spectral line shape or could also shift the overall spectral weight to the higher binding-energy side. The energy scale of the shown spectra was fixed by positioning the O 1*s* level at 530.1 eV as an internal reference.

6.3.4 Discussion of optimal growth parameters and literature review

In this section, the PES results on the chemical structure of Fe_3O_4/GaAs are finally summarized and compared with the investigations of the microstructure. Also, a comparison with literature results is given.

The As layer that segregates to the surface during Fe deposition is easily oxidized to arsenic oxide and mostly volatilizes during the postoxidation step (see Sec. 6.3.1). The interface resident 'reacted' As and Ga components inside the initial Fe matrix are also partially oxidized. The degree of this oxidation process depends strongly on the initial Fe layer and postoxidation parameters such as duration, annealing temperature, and partial pressure of oxygen. For example, a larger initial Fe layer effectively buries these layers and diminishes the amount of oxygen that can react with them. However, as these reacted components only represent a tiny fraction of atoms detected by PES (cf. Sec. 6.3.1), they do not contribute considerably to the HAXPES spectra.

Table 6.3: *Experimental growth parameters (initial Fe layer thickness, oxidation pressure, temperature, and time) used for Fe_3O_4/Fe/GaAs samples and respective interface layer thicknesses determined by HAXPES experiments.*

sample no.	20†	21	22*	23*
initial Fe layer (Å)	50	33	23	36
$p(O_2)$ (mbar)	$5 \cdot 10^{-5}$	$1 \cdot 10^{-6}$	$1 \cdot 10^{-6}$	$5 \cdot 10^{-5}$
$T(O_2)$ (K)	600	650	700	600
$t(O_2)$ (min)	12	10	30	3
As_2O_3 layer (Å)	6.2 ± 2	0.6 ± 0.7	4.9 ± 1.6	1.1 ± 1
Ga_2O_3 layer (Å)	4.7 ± 0.8	1.2 ± 1.1	4.0 ± 1	1.2 ± 0.7
Fe interface layer (Å)	6 ± 1	2.2 ± 1.5	0.14 ± 0.06	0.11 ± 0.03
magnetite layer (Å)	87 ± 9	30 ± 4	19.5 ± 0.2	32 ± 9

†: cf. Ref. [177], *: cf. Ref. [207]

Because of the statistical nature of the oxygen diffusion into the film, some oxygen can always reach the interface and hence partly oxidize the GaAs substrate. This mechanism is again controlled by the quality of the initial Fe film and the used oxidation parameters, which complicates a comparison of different samples (see Tab. 6.3). Especially, the diffusion of oxygen towards the interface and the diffusion of As and Ga towards the surface is known to be linked to structural defects such as boundaries between coalesced islands inside the film [208]. It seems to be clear that a too large initial Fe layer thickness will always lead to an elemental Fe layer remaining at the interface because the thickness up to which Fe can be properly oxidized is limited to about 5 nm with the used postoxidation procedure [203]. Since it is believed that an elemental Fe layer could act as a Schottky barrier or could be antiferromagnetically coupled to the magnetite layer [204], the thickness of this Fe layer should be minimized as far as possible.

Based on these criteria an initial Fe layer with a thickness between 30 and 50Å is a good choice. It reduces considerably the amount of oxidation of the substrate in comparison with a co-deposition technique and itself becomes almost completely oxidized, leaving only a small fraction of elemental Fe (see Tab. 6.3).

The here presented results can be classified against the background of existing literature as follows. Former publications on Fe_3O_4/GaAs samples cover their fabrication by either postoxidation of Fe as in this study [188, 209, 210], by PLD [175], by reactive dc magnetron sputtering of an Fe target in an O_2 partial pressure [211], or by reactive MBE [193]. However, it is not reported in Refs. [193, 209–211] if interface phases exist after application of their respective growth method, which hampers a direct comparison with present results.

Lu *et al.* have postoxidized Fe to magnetite on GaAs(001) and inferred from the results of their XPS, XAS, and XMCD investigations the existence of an FeO layer at the interface. An increase of the Fe^{2+} spectral weight for larger information depth was also observed in the HAXPES spectra of Fig. 6.15. Such an FeO-like layer would most likely be located between the Fe and Fe_3O_4 layers. However, as already discussed above, it is considerably more difficult to discriminate FeO than elemental Fe from magnetite in the spectra because of the lower binding-energy difference and larger spectral width. The amount of FeO present in the film cannot be determined exactly. However, it is estimated that the FeO fraction is significantly smaller than the Fe fraction. The elemental Fe interface phase was also verified by STEM and XRR, whereas an additional FeO-phase was not detected (see Sec. 6.2). Kubaschewski and Hopkins argue that FeO does not appear at all during the oxidation of Fe below 400°C [212]. Furthermore, XPS normal emission spectra of films from Lu *et al.* [188, 213] also point towards the presence of Fe in deeper layers although this fact was not commented in these publications. Generally, there remains some doubt that the postoxidation procedure applied in Refs. [188, 209, 210] does not leave an Fe interface layer since applied postoxidation temperatures and oxygen dosages were relatively low in comparison with our studies (cf. Tab. 6.3).

Preisler *et al.* [175] proposed that their obtained (111)-oriented polycrystalline growth of Fe_3O_4 on GaAs(100) by means of PLD is triggered by the presence of an amorphous interface. Moreover, they noticed a strong shoulder in the Ga $3d$ spectrum measured with Al-K_α radiation indicating Ga-Fe bonding. There is no evidence for a (111) orientation, a polycrystalline film structure, or Ga-Fe bonding in our results. However, the moderate quality of some LEED patterns of very thin films could be linked to the presence of amorphous gallium- and arsenic-oxide interface phases. Since it can be safely assumed that elemental Fe is not deposited during the PLD process, the finding of a Ga-Fe species by Preisler *et al.* has to be explained by a stronger intermixing or a reduction of Fe_3O_4 to Fe at the interface, both of which in turn could be induced by the utilization of the PLD technique.

To better understand the results at hand concerning the nature of arsenic and gallium oxides, some experimental findings on the oxidation of GaAs surfaces found in the literature shall be shortly reviewed here. Experiments on the thermal oxidation of GaAs

have shown that at high temperatures (800-1000 K) primarily polycrystalline Ga_2O_3 and possibly $GaAsO_4$ are formed [176, 214]. At lower oxidation temperatures, the resulting products are amorphous and again mainly Ga_2O_3 and a smaller fraction of elemental As at the oxide/GaAs interface. As_2O_3 is additionally found for oxidation with molecular oxygen at low and intermediate temperatures.

Transferring these results to our case, the oxidation conditions for the GaAs substrate in Fe_3O_4/GaAs apparently are weak because of rather low temperatures, small oxygen partial pressure, and the presence of the easily oxidized Fe. In accordance, no $GaAsO_4$ has been observed, which could easily be detected by XPS due to the large chemical shift of about −4.8 eV with respect to the GaAs component in both As and Ga core levels. On the other hand, given weak oxidation conditions, elemental As should be found, which is, however, not largely present. Probably, the formation of elemental or 'reacted' As occurs only during the Fe deposition step. This component is hardly detectable after transformation of the Fe into magnetite. Instead, the emergence of arsenic and gallium oxide is favored by the present kinetic growth conditions.

6.4 Magnetic properties

6.4.1 X-ray magnetic circular dichroism

The XAS and XMCD spectra of magnetite films on GaAs differ among each other according to the exact preparation parameters, such as initial Fe layer thickness and duration and temperature of the postoxidation procedure. The spectral differences can be attributed to the degree of oxidation of the initial Fe film. Figure 6.17 displays the unpolarized XAS and XMCD spectra of an Fe_3O_4/GaAs sample which exhibits a substantial Fe layer at the interface after the postoxidation (black curve). The red curves in Fig. 6.17 are the same Fe_3O_4/ZnO spectra as displayed in Fig. 4.20. They are plotted for the sake of comparison and stand for nearly-stoichiometric magnetite.

The XMCD spectrum of Fe_3O_4/ZnO is scaled to the same height of the positive peak at the L_3-edge, which is attributed to the Fe^{3+}_{tet} ions, to facilitate a better comparison with the GaAs-based sample. Both negative peaks at the L_3-edge are higher for the film on GaAs assuming the same amount of Fe^{3+}_{tet} in both samples. The increased intensity of the first peak at 710.5 eV can be attributed to increased amounts of elemental Fe (Fe^0) or wüstite (Fe^{2+}) since Regan *et al.* have shown that the Fe^0 and Fe^{2+} peaks in the XAS spectrum occur at the same energy [215]. Lu *et al.* have attributed the increased height of this peak for their Fe_3O_4/GaAs samples to an FeO (Fe^{2+}) layer at the interface [213]. However, as was discussed in Sec. 6.3.3, our PES results clearly favor the presence of elemental Fe in samples prepared in such a way.

This spectral contribution of elemental Fe is also observed at the L_2-edge (see blue marked region in Fig. 6.17). The shown spectrum is a superposition of the three-peak structure indicative for magnetite and the broad single peak indicative for elemental

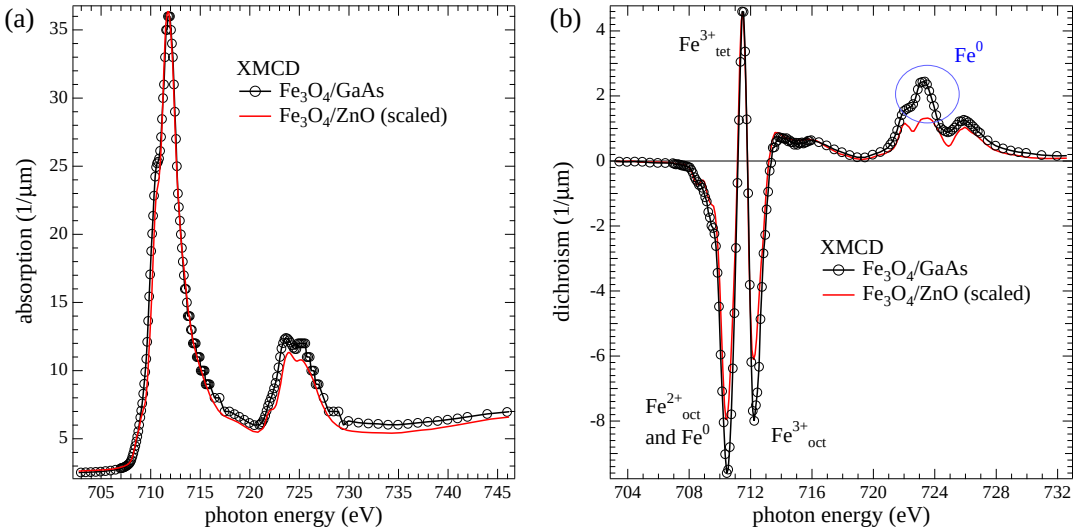

Figure 6.17: *(a) XAS and (b) XMCD spectrum of a 5 nm thick Fe_3O_4/GaAs film (sample no. 24) taken at 70° incidence in a magnetic field of $\mu_0 H = \pm 3\,T$ and at room temperature (black). The scaled spectrum of a Fe_3O_4/ZnO film is plotted for comparison (red).*

Table 6.4: *Results of a sum-rule analysis of 0° and 70° incidence XMCD spectra of ex situ and in situ prepared Fe_3O_4/GaAs samples. Measurements were taken in a field of $\mu_0 H = \pm 3\,T$ and at room temperature.*

sample no.		24	25	26	27	28
thickness		5.0 nm	3.3 nm	5.0 nm	3.3 nm	6.6 nm
XMCD performed		*ex situ*	*ex situ*	*in situ*	*in situ*	*in situ*
δ ($\lambda_{XAS} = 18 - 25$ Å)		0.08	—	0.12	0.169	0.112
0°	m^*_{spin} (μ_B/f.u.)	3.66	2.97	2.88	2.61	2.94
	m_{orb} (μ_B/f.u.)	0.0011	0.06	0.03	0.006	0.09
	m_{orb}/m^*_{spin}	0.0003	0.02	0.01	0.0023	0.031
70°	m^*_{spin} (μ_B/f.u.)	3.42	2.91	2.94	2.70	2.85
	m_{orb} (μ_B/f.u.)	0.09	0.12	0.03	0.09	0.014
	m_{orb}/m^*_{spin}	0.026	0.041	0.01	0.033	0.005

$\Delta\delta = 0.018$, $\Delta m_{spin} = 0.15\,\mu_B$/f.u., $\Delta m_{orb} = 0.06\,\mu_B$/f.u.

Fe. Since the XMCD effect of elemental Fe is much more pronounced than the one of magnetite, small amounts of elemental Fe are seen as a relative strong signal in the XMCD.

Additionally, the increase of the Fe^{3+}_{oct} peak points towards a larger off-stoichiometry parameter δ of the oxide layer in comparison to the ZnO-based samples. This is also reflected in the larger values of δ determined by fitting the XAS spectra (see Tab. 6.4). After application of the postoxidation procedure, the surface is more heavily oxidized than after application of the codeposition method as ZnO-based films.

The single contributions of valencies and sites are more difficult to discern in the unpolarized XAS spectrum in Fig. 4.20(a) at first glance. This is due to the fact that the peak position of elemental Fe at the L_3-edge is located at the same energy of 710 eV as the shoulder of the $Fe_{3-\delta}O_4$-spectrum that declines for larger δ. In the shown Fe_3O_4/GaAs spectrum, this shoulder decreases as the Fe^0 peak increases. Again the XAS spectrum was used to quantify the composition of the sample by fitting the experimental spectrum with data from Regan *et al.* and Pellegrin *et al.* [116, 215]. The contribution of the elemental Fe layer to the spectrum is $14 \pm 5\,\%$, and the remaining layer is $Fe_{3-\delta}O_4$ with $\delta = 0.08$.

Figure 6.18 shows magnetization curves of two different Fe_3O_4 films on GaAs measured at the position corresponding to the Fe^{2+}_{oct}-XMCD peak. Both samples possess reduced

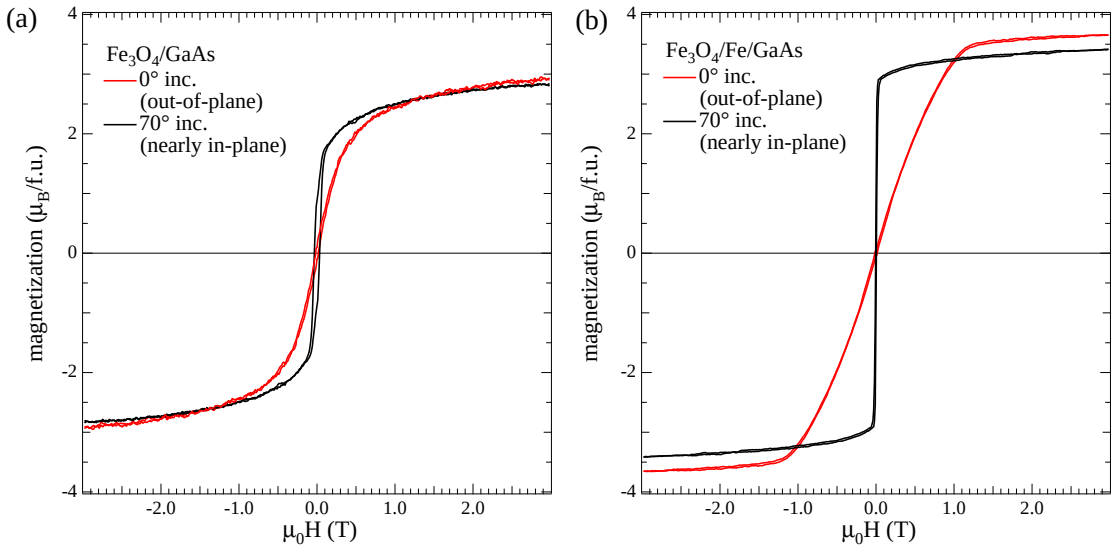

Figure 6.18: *XMCD magnetization curves of Fe_3O_4 films on GaAs. The magnetization was determined from a sum-rule analysis of XMCD spectra. (a) Fe_3O_4 film with $\delta = 0.12$ and negligible Fe contribution (sample no. 26). (b) Fe_3O_4 film with $\delta = 0.08$ and a contribution (about 14 %) of an elemental Fe interface-layer to the spectrum (sample no. 24).*

magnetization in comparison with bulk saturation. The curve in Fig. 6.18(a) shows slow saturation behavior similar to films on ZnO (see Fig. 4.21), while the one in Fig. 6.18(b)

exhibits a larger squareness and also increased magnetization (see also Tab. 6.4). The latter sample exhibits a contribution of 14 % of elemental Fe to the spectrum within the probing depth. Both samples exhibit larger magnetization for higher XAS probing depth, i.e., at 0° incidence. While this effect is only small in panel (a), it is more pronounced in panel (b). Measurements with larger probing depths are more sensitive to the Fe interface layer that is significantly larger for sample no. 24. In summary, the magnetic properties of the Fe_3O_4 films on GaAs are strongly influenced by the interface layer of elemental Fe.

Coercive fields of Fe_3O_4/GaAs samples range from 9 to 24 mT and their remanent magnetization is between 1 to 5 % of the value at $\mu_0 H = 3$ T for out-of-plane, i.e., 0° incidence, measurements.

The surface magnetization which was derived by a sum-rule analysis ranges from 2.61 to 2.97 μ_B/f.u. for sample nos. 25 to 28. These values are very similar to the ones obtained for ZnO-based samples (cf. Tab. 4.3). This suggests that the surface magnetization of these samples is comparable even though the off-stoichiometry is sightly larger. A discussion of the reduction of the magnetization values in comparison with the bulk value by about 1 μ_B/f.u. was already given in Sec. 4.5.3. This reduction is not solely due to the off-stoichiometry, i.e., the number of Fe^{2+}_{oct} site moments. Exclusively, sample no. 24 shows a relatively high magnetization because of its large interface layer.

6.4.2 Magnetometry

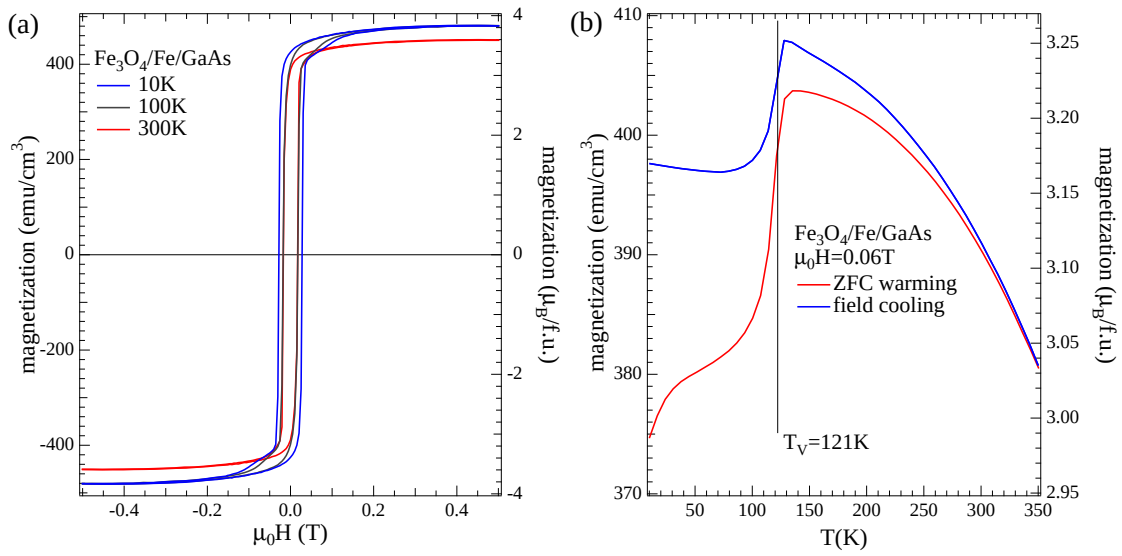

Figure 6.19: *SQUID characterization of an Fe_3O_4/Fe/GaAs sample (sample no. 18) with an in-plane applied field. (a) Magnetization curves at different temperatures. (b) $M(T)$-curves measured in $\mu_0 H = 0.06$ T. Warming cycle of a zero-field-cooled sample (ZFC) and field-cooling cycle.*

Figure 6.19 details the magnetic behavior of a 23 nm thick Fe_3O_4/GaAs sample possessing an elemental Fe interface layer of 3.5 nm thickness according to XRR (sample no. 18). For the shown curves the magnetic field is applied in-plane of the film so that the shape anisotropy field of the thin film is zero and the effective inner field is equal to the applied one. The diamagnetic contribution of the GaAs substrate was subtracted with a linear slope of $\chi = -0.845 \cdot 10^{-6}\,\mathrm{emu/(Oe{\cdot}cm^3)}$ (literature value $\chi_{\mathrm{GaAs}} = -1.211 \cdot 10^{-6}\,\mathrm{emu/(Oe{\cdot}cm^3)}$ [216]). Note that the shown magnetization is normalized to the complete film thickness, i.e., thickness of the magnetite layer plus elemental Fe layer.

The magnetization at the highest applied field of 0.5 T is about $3.6\,\mu_B$/f.u. at room temperature and therefore only slightly lower than the expected bulk saturation of magnetite. However, part of the magnetization originates from the Fe interface layer. The $M(H)$-curves in Fig. 6.19(a) show clear ferromagnetic hysteresis and increasing saturation magnetization and coercive field for decreasing temperature. Generally, the coercive field of a sample depends strongly on its structural quality and history. In the case of magnetite, the coercive field also varies with temperature, namely its magnitude decreases on lowering the temperature and shows a dip around the isotropic point near to the Verwey-transition temperature [160].

In comparison with single crystals, the approach to saturation of the Fe_3O_4/GaAs sample is rather slow, however in comparison with the monocrystalline film on a ZnO substrate, it is relatively fast. Also, the squareness, which is the ratio of the remanence to the saturation magnetization, is larger than for the ZnO-based films (see Sec. 4.5) and MgO-based films found in the literature. The law of approach to saturation can be well described by Eq. (2.2), i.e., with the one-dimensional model for antiferromagnetic coupling at APBs. The best fit parameter, viz. $b = 0.023 \pm 0.03\,\mathrm{T^{1/2}}$, is smaller by about a factor of five in comparison with the film on ZnO indicating a significantly smaller APB density inside the sample. This is in line with the fact that, in contrast to the ZnO films, no APB was detected by the STEM investigation of the Fe_3O_4/GaAs sample in Sec. 6.2.

The elemental Fe interface layer plays a crucial role for the magnetic behavior of the sample. Firstly, it enhances the overall magnetization since Fe possesses a considerably higher saturation magnetization, viz. $1752\,\mathrm{emu/cm^3}$ [7], than magnetite. Secondly, the Fe layer is easily magnetized at low fields because its magnetocrystalline easy axis lies in-plane and the film defects in Fe are less important with respect to the approach to saturation. Therefore, the magnetized Fe layer aligns the magnetization of the magnetite layer at relatively low fields. It is also likely that postoxidation of Fe films produces a different, possibly smaller APB density than the reactive co-deposition of Fe and O, which was employed in case of ZnO and InAs substrates. Magen *et al.* found larger squareness, increased saturation moments, and lower APB densities for Fe_3O_4/Fe and Fe_3O_4/Cr bilayers deposited on MgO in comparison to single magnetite layers [217].

Figure 6.19(b) shows the temperature-dependent magnetization in an applied field of 0.06 T that is considerably smaller than the saturation field. Recall that the magnitude

of the magnetization jump depends crucially on the applied field and is largest for relatively low fields around 0.1 T (see Sec. 2.2). The $M(T)$-curve exhibits a jump of the magnetization in the vicinity of the Verwey-transition temperature of $T_V = 121\,\mathrm{K}$. In comparison with films on ZnO and InAs, both, the magnetization jump at the transition and the temperature region over which the transition takes place, are small. This could also be due to the elemental Fe layer, which of course does not participate in the transition. The occurrence of this phase transition evidences the good structural and electronic properties of the magnetite layer.

7 Summary and outlook

The present thesis deals with the growth of magnetite thin films on semiconducting substrates and the characterization of their structural, chemical, electronic, and magnetic properties. Integration of magnetite with the template materials ZnO, InAs, and GaAs was motivated by the potential application of a magnetic oxide in semiconductor technology and particularly in spintronics.

High-quality growth of Fe_3O_4 on the (001) and (00$\bar{1}$) surfaces of ZnO was demonstrated. This thesis contains the first report of successful growth of this structure by means of MBE. The films are highly oriented along (111) in the growth direction and exhibit the in-plane epitaxial relationship $Fe_3O_4[2\bar{1}\bar{1}]$ ||ZnO[100] and $Fe_3O_4[1\bar{1}0]$ ||ZnO[110]. A small interface roughness of less than 1 nm has been confirmed by several methods for films of different thicknesses. No indications for interfacial reactions or intermixing have been found. Growth proceeds in a wetting layer plus island-mode and a later coalescence of islands as was verified by electron diffraction, topography measurements of the surface, and the investigation of the microstructure. Due to this island-like growth mode, a domain structure with anti-phase boundaries (APBs) and twin boundaries (rotational twinning) forms upon coalescence of the islands. X-ray diffraction results indicate that grown films nearly exhibit the lattice constant of bulk magnetite with less than $\pm 0.6\,\%$ unrelaxed macro strain. X-ray absorption spectroscopy and x-ray photoelectron spectroscopy (XPS) have been used to study the stoichiometry of *in situ* and *ex situ* prepared surfaces in detail and show that the off-stoichiometry parameter δ of $Fe_{3-\delta}O_4$ typically is only about 0.05 inside a surface region of about 2 nm thickness. Growth of very thin films with constant Fe/O_2 flux ratio results in a thin FeO-like interface layer. Using a decreased Fe/O_2 flux ratio at the early growth stage forces the films to be fully stoichiometric also at the interface. Besides the discussed small off-stoichiometries, the samples are phase-pure magnetite according to all present results. Magnetometry of the 'volume' of the films, with a superconducting quantum interference device confirms a nearly bulk-like saturation magnetization. However, the approach to saturation is by far slower than in single crystals due to reduced magnetization at APBs in low fields, which is similar to reports on magnetite films grown on other substrates found in the literature. A 40 nm thick film showed a clear Verwey transition in the temperature-dependent magnetization data. A sum-rule analysis of x-ray magnetic circular dichroism (XMCD) spectra revealed that the magnetization of the surface layer is lower by roughly $1\,\mu_B$/f.u. than the 'volume' magnetization. Different error sources and intrinsic properties have been thoroughly discussed to explain this phenomenon. It has been concluded that a magnetically 'dead' surface layer of about 0.6 nm thickness does not contribute to the

net magnetization. This reduced surface magnetization also occurs for films grown on the other two substrates.

For the Fe_3O_4/InAs system, polycrystalline growth has been evidenced for films which were about 8 nm thick. XPS spectra which were measured *in situ* showed that nearly stoichiometric magnetite could be grown. However, interfacial reactions occur which result in the presence of arsenic oxide and possibly indium oxide and cause an indium-enrichment near the interface. Inferior magnetic properties, viz. low magnetization values and a broad Verwey transition, in comparison with films on ZnO substrates were found. It is likely that the structural and magnetic properties are related to the poorly crystallized interface phases.

For the fabrication of Fe_3O_4/GaAs films, the method of postoxidation of thin Fe films was applied. It was shown that this method induces an improvement of the structural and magnetic properties in comparison with films on the similar InAs substrate. As has been demonstrated by diffraction, the structure is well oriented and has the epitaxial relationship $Fe_3O_4(001)[110] \| GaAs(001)[010]$. Growth proceeds by a transformation of the topmost Fe layers into magnetite. Depending on the exact preparation conditions either the complete Fe film is transformed or an elemental Fe layer remains at the interface. Such an Fe interface layer causes an increase of the magnetization and a faster approach to saturation. We argue that the fast approach to saturation is connected to a decreased density of APBs inside the magnetite film. Interface phases, viz. arsenic and gallium oxides, exist for the GaAs substrate as in the case of InAs substrates. However, the postoxidation method and the introduction of the Fe interface layer considerably reduce the amount of theses phase. The spin polarization of the surface, which was measured by photoelectron spectroscopy, was absent when using oxidation conditions anticipated as optimal according to XPS and about $-20\,\%$ when using more weakly oxidizing conditions.

In summary, it has been demonstrated how epitaxy and a real, i.e., imperfect, crystal structure crucially determine the physical properties of magnetite thin films. The films have been thoroughly studied by standard techniques and also by advanced spectroscopy methods such as XMCD. The present thesis gives direct insight into the fabrication and the understanding of properties of magnetite films grown on semiconductor substrates. It identifies some of the complications which arise when performing direct growth of an oxide on a semiconductor. The Fe_3O_4/ZnO structure seems to be very promising for futures studies and applications. Probably, its properties could be further optimized by exploring a wider space of growth parameters. For example, the effect of sample annealing on the microstructure and the APB density would be very interesting to study. The structural and magnetic properties of Fe_3O_4/InAs and Fe_3O_4/GaAs films possibly can be further improved. An optimization of previously known growth recipes for Fe_3O_4/GaAs films has been given here. In the case of Fe_3O_4/InAs films, the next step would consist in investigating the influence of the substrate surface reconstruction on the growth result. Finally, spin-dependent transport would be the ultimate test of such structures for prospective applications.

Appendix

Table A.1: *Table of reported samples. T_g is the growth temperature, and t the film thickness. *adjustment of the Fe/O_2 flux ratio during growth. †fabricated by postoxidation of Fe.*

sample (no.)	place	date	substrate	T_g (°C)	Fe flux (Å/min)	$p(O_2)$ (mbar)	t (nm)
1*	Würzburg	10.09.2009	ZnO(001)	405	5	$3.75 \cdot 10^{-6}$	16
2	Vancouver	18.10.2008	ZnO(00$\bar{1}$)	505	8	$3.97 \cdot 10^{-6}$	30
3	Vancouver	20.10.2008	ZnO(00$\bar{1}$)	530	8	$3.97 \cdot 10^{-6}$	36
4	Vancouver	29.09.2008	ZnO(001)	490	10	$3.77 \cdot 10^{-6}$	12
5	Vancouver	07.10.2008	ZnO(00$\bar{1}$)	485	8.5	$3.99 \cdot 10^{-6}$	25
6*	Würzburg	18.09.2009	ZnO(00$\bar{1}$)	410	5	$3.75 \cdot 10^{-6}$	62.4
7*	Würzburg	13.09.2009	ZnO(00$\bar{1}$)	410	5	$3.75 \cdot 10^{-6}$	40.5
8	Würzburg	08.08.2009	ZnO(001)	400	5	$4.00 \cdot 10^{-6}$	14
9	Vancouver	29.05.2008	ZnO(00$\bar{1}$)	530	10	$3.87 \cdot 10^{-6}$	21
10*	Würzburg	13.09.2009	ZnO(00$\bar{1}$)	410	5	$3.70 \cdot 10^{-6}$	8
11*	Würzburg	13.09.2009	ZnO(00$\bar{1}$)	410	5	$3.70 \cdot 10^{-6}$	4
12*	BESSY	18.10.2009	ZnO(00$\bar{1}$)	420	5	$3.70 \cdot 10^{-6}$	8
13*	Würzburg	11.02.2009	InAs(001)	280	3	$5.00 \cdot 10^{-6}$	8
14*	Würzburg	13.02.2009	InAs(001)	280	3	$5.00 \cdot 10^{-6}$	8
15*	Würzburg	15.02.2009	InAs(001)	350	3	$3.70 \cdot 10^{-6}$	8
16*	Würzburg	08.02.2009	InAs(001)	360	3	$8.00 \cdot 10^{-6}$	6
17†	Würzburg	20.05.2009	GaAs(001)	315	4	$5.00 \cdot 10^{-5}$	5
18	Würzburg	19.09.2009	GaAs(001)	310	5	$9.00 \cdot 10^{-7}$	22.8
19†	NSLS	30.06.2009	GaAs(001)	260	2.6	$4.93 \cdot 10^{-5}$	10
20†	Würzburg	22.05.2009	GaAs(001)	300	4.2	$5.00 \cdot 10^{-5}$	9.3
21†	Würzburg	20.07.2007	GaAs(001)	350	2.2	$1.00 \cdot 10^{-6}$	3.2
22†	Würzburg	21.07.2007	GaAs(001)	400	2.7	$1.00 \cdot 10^{-6}$	2.0
23†	Würzburg	22.07.2007	GaAs(001)	300	4.2	$5.00 \cdot 10^{-5}$	3.2
24†	Würzburg	15.09.2009	GaAs(001)	335	5	$5.00 \cdot 10^{-5}$	5
25†	Würzburg	15.09.2009	GaAs(001)	335	5	$5.00 \cdot 10^{-5}$	3.3
26†	BESSY	11.10.2009	GaAs(001)	315	4.2	$5.00 \cdot 10^{-5}$	5
27†	BESSY	11.10.2009	GaAs(001)	315	4.2	$5.00 \cdot 10^{-5}$	3.3
28†	BESSY	14.10.2009	GaAs(001)	320	5	$5.00 \cdot 10^{-5}$	6.6

Bibliography

[1] P. A. Dowben and R. Skomski, Journal of Applied Physics **95**, 7453 (2004).

[2] A. M. Haghiri-Gosnet, T. Arnal, R. Soulimane, M. Koubaa, and J. P. Renard, Physica Status Solidi A **201**, 1392 (2004).

[3] S. A. Wolf et al., Science **294**, 1488 (2001).

[4] S. Datta and B. Das, Applied Physics Letters **56**, 665 (1990).

[5] A. Waag, Akademie-Journal **1/2004**, 32 (2004).

[6] Z. Szotek et al., Physical Review B **74**, 174431 (2006).

[7] B. D. Cullity and C. D. Graham, *Introduction to Magnetic Materials*, John Wiley and Sons, Hoboken, 2nd edition (2009).

[8] A. Yanase and N. Hamada, Journal of the Physical Society of Japan **68**, 1607 (1999).

[9] P. A. Miles, W. B. Westphal, and A. V. Hippel, Reviews of Modern Physics **29**, 279 (1957).

[10] M. I. Klinger and A. A. Samokhvalov, Physica Status Solidi B **79**, 9 (1977).

[11] G. Schmidt, D. Ferrand, L. W. Molenkamp, A. T. Filip, and B. J. van Wees, Physical Review B **62**, R4790 (2000).

[12] A. Fert and H. Jaffrès, Physical Review B **64**, 184420 (2001).

[13] I. Pallecchi et al., Physical Review B **81**, 165311 (2010).

[14] P. Kotissek et al., Nature Physics **3**, 872 (2007).

[15] Y. J. Kim, Y. Gao, and S. A. Chambers, Surface Science **371**, 358 (1997).

[16] F. C. Voogt et al., Physical Review B **60**, 11193 (1999).

[17] S. K. Arora, R. G. S. Sofin, I. V. Shvets, and M. Luysberg, Journal of Applied Physics **100**, 073908 (2006).

[18] W. Weiss and M. Ritter, Physical Review B **59**, 5201 (1999).

[19] F. Schedin et al., Journal of Magnetism and Magnetic Materials **211**, 266 (2000).

[20] S. F. Alvarado, M. Erbudak, and P. Munz, Physical Review B **14**, 2740 (1976).

[21] S. A. Morton et al., Surface Science **513**, L451 (2002).

[22] M. Fonin et al., Physical Review B **72**, 104436 (2005).

[23] Y. S. Dedkov, U. Rüdiger, and G. Güntherodt, Physical Review B **65**, 064417 (2002).

[24] A. M. Bataille et al., Journal of Magnetism and Magnetic Materials **316**, E963 (2007).

[25] G. Hu and Y. Suzuki, Physical Review Letters **89**, 276601 (2002).

[26] J. M. D. Coey and S. Sanvito, Journal of Physics D: Applied Physics **37**, 988 (2004).

[27] B. Bryson, *A Short History of Nearly Everything*, Random House, London, 1st edition (2004).

[28] M. E. Fleet, Acta Crystallographica Section B **37**, 917 (1981).

[29] R. L. Blake, R. E. Hessevic, T. Zoltai, and L. W. Finger, American Mineralogist **51**, 123 (1966).

[30] C. Pecharromán, T. Gonzalez-Carreño, and J. E. Iglesias, Physics and Chemistry of Minerals **22**, 21 (1995).

[31] H. Fjellvåg, F. Grønvold, S. Stølen, and B. Hauback, Journal of Solid State Chemistry **124**, 52 (1996).

[32] L. Néel, Annales de Physique **3**, 137 (1948).

[33] M. Uhl and B. Siberchicot, Journal of Physics: Condensed Matter **7**, 4227 (1995).

[34] Y. Yafet and C. Kittel, Physical Review **87**, 290 (1952).

[35] M. A. Willard, Y. Nakamura, D. E. Laughlin, and M. E. McHenry, Journal of the American Ceramic Society **82**, 3342 (1999).

[36] Z. Kąkol and J. M. Honig, Physical Review B **40**, 9090 (1989).

[37] M. Penicaud, B. Siberchicot, C. B. Sommers, and J. Kubler, Journal of Magnetism and Magnetic Materials **103**, 212 (1992).

[38] R. M. Cornell and U. Schwertmann, *The Iron Oxides: Structure, Properties, Reactions, Occurence and Uses*, Wiley-VCH, Weinheim, 2nd edition (2003).

[39] J. García and G. Subías, Journal of Physics: Condensed Matter **16**, R145 (2004).

[40] D. T. Margulies et al., Physical Review B **53**, 9175 (1996).

[41] F. C. Voogt et al., Physical Review B **57**, R8107 (1998).

[42] D. T. Margulies et al., Physical Review Letters **79**, 5162 (1997).

[43] T. Hibma et al., Journal of Applied Physics **85**, 5291 (1999).

[44] S. Celotto, W. Eerenstein, and T. Hibma, European Physical Journal B **36**, 271 (2003).

[45] H. Zijlstra, IEEE Transactions on Magnetics **15**, 1246 (1979).

[46] B. Dieny, D. Givord, and J. M. B. Ndjaka, Journal of Magnetism and Magnetic Materials **93**, 503 (1991).

[47] J.-B. Moussy et al., Physical Review B **70**, 174448 (2004).

[48] A. M. Bataille et al., Physical Review B **74**, 155438 (2006).

[49] T. Kasama, R. E. Dunin-Borkowski, and W. Eerenstein, Physical Review B **73**, 104432 (2006).

[50] M. Friák, A. Schindlmayr, and M. Scheffler, New Journal of Physics **9**, 5 (2007).

[51] R. A. De Groot and K. H. J. Buschow, Journal of Magnetism and Magnetic Materials **54-57**, 1377 (1986).

[52] Z. Zhang and S. Satpathy, Physical Review B **44**, 13319 (1991).

[53] H. T. Jeng and G. Y. Guo, Physical Review B **65**, 094429 (2002).

[54] H. T. Jeng, G. Y. Guo, and D. J. Huang, Physical Review Letters **93**, 156403 (2004).

[55] Z. Szotek et al., Journal of Physics: Condensed Matter **16**, S5587 (2004).

[56] Z. Szotek et al., Physical Review B **68**, 054415 (2003).

[57] E. J. W. Verwey, Nature **144**, 327 (1939).

[58] E. J. W. Verwey, P. W. Haayman, and F. C. Romeijn, Journal of Chemical Physics **15**, 181 (1947).

[59] R. Aragon, Physical Review B **46**, 5328 (1992).

[60] J. P. Shepherd, J. W. Koenitzer, R. Aragon, J. Spalek, and J. M. Honig, Physical Review B **43**, 8461 (1991).

[61] Z. Kąkol, Journal of Solid State Chemistry **88**, 104 (1990).

[62] V. A. M. Brabers, F. Walz, and H. Kronmüller, Physical Review B **58**, 14163 (1998).

[63] M. Matsui, S. Todo, and S. Chikazumi, Journal of the Physical Society of Japan **42**, 1517 (1977).

[64] M. G. Chapline and S. X. Wang, Journal Of Applied Physics **97** (2005).

[65] J. E. Lorenzo et al., Physical Review Letters **101**, 226401 (2008).

[66] K. P. Belov, Physics-Uspekhi **163**, 56 (1993).

[67] A. R. Muxworthy and E. McClelland, Geophysical Journal International **140**, 101 (2000).

[68] D. G. Schlom, L. Q. Chen, X. Q. Pan, A. Schmehl, and M. A. Zurbuchen, Journal of the American Ceramic Society **91**, 2429 (2008).

[69] K. W. Kolasinski, *Surface Science: Foundation of Catalysis and Nanoscience*, John Wiley and Sons, Chichester, 2nd edition (2008).

[70] J. O'Hanlon, *A User's Guide to Vacuum Techology*, John Wiley and Sons, New York, 2nd edition (1989).

[71] J. A. Venables, G. D. T. Spiller, and M. Hanbucken, Reports on Progress in Physics **47**, 399 (1984).

[72] T. Fujii, M. Takano, R. Katano, Y. Bando, and Y. Isozumi, Journal of Applied Physics **66**, 3168 (1989).

[73] W. Eerenstein, T. T. M. Palstra, T. Hibma, and S. Celotto, Physical Review B **68**, 014428 (2003).

[74] R. F. C. Farrow et al., Journal of Applied Physics **93**, 5626 (2003).

[75] S. Little and A. Zangwill, Physical Review B **49**, 16659 (1994).

[76] A. P. Sutton and R. W. Baluffi, *Interfaces in Crystalline Materials*, Calendron Press, Oxford, 1st edition (1995).

[77] O. Y. Gorbenko, S. V. Samoilenkov, I. E. Graboy, and A. R. Kaul, Chemistry of Materials **14**, 4026 (2002).

[78] K. Balakrishnan, S. K. Arora, and I. V. Shvets, Journal of Physics: Condensed Matter **16**, 5387 (2004).

[79] M. Ohring, *Materials Science of Thin Films*, Academic Press, New York, 2nd edition (2002).

[80] A. Fischer, H. Kühne, and H. Richter, Physical Review Letters **73**, 2712 (1994).

[81] F. Niu, A. L. Meier, and B. W. Wessels, Journal of Vacuum Science and Technology B **24**, 2586 (2006).

[82] C. Boothman, A. M. Sánchez, and S. van Dijken, Journal of Applied Physics **101**, 123903 (2007).

[83] K. J. Hubbard and D. G. Schlom, Journal of Materials Research **11**, 2757 (1996).

[84] R. Beyers, Journal of Applied Physics **56**, 147 (1984).

[85] I. Barin, *Thermochemical Properties of Inorganic Substances*, Springer, Berlin, 1st edition (1973).

[86] F. Reinert and S. Hüfner, New Journal of Physics **7**, 97 (2005).

[87] S. Hüfner, *Photoelectron Spectroscopy*, Springer, Berlin, 3rd edition (2003).

[88] A. Damascelli, Physica Scripta **T109**, 61 (2004).

[89] S. Tanuma et al., Surface and Interface Analysis **37**, 833 (2005).

[90] J. J. Yeh and I. Lindau, Atomic Data and Nuclear Data Tables **32**, 1 (1985).

[91] M. B. Trzhaskovskaya, V. Nefedov, and V. G. Yarzhemsky, Atomic Data and Nuclear Data Tables **77**, 97 (2001).

[92] P. Ruffieux et al., Review of Scientific Instruments **71**, 3634 (2000).

[93] R. W. Bernstein and J. K. Grepstad, Surface and Interface Analysis **14**, 109 (1989).

[94] Z. Liu et al., Journal of Vacuum Science and Technology A **21**, 212 (2003).

[95] T. Fujii et al., Physical Review B **59**, 3195 (1999).

[96] C. R. Brundle, T. J. Chuang, and K. Wandelt, Surface Science **68**, 459 (1977).

[97] N. S. McIntyre and D. G. Zetaruk, Analytical Chemistry **49**, 1521 (1977).

[98] P. Mills and J. L. Sullivan, Journal of Physics D: Applied Physics **16**, 723 (1983).

[99] S. Gota, E. Guiot, M. Henriot, and M. Gautier-Soyer, Physical Review B **60**, 14387 (1999).

[100] R. J. Lad and V. E. Henrich, Physical Review B **39**, 13478 (1989).

[101] D. Schrupp, *Hoch- und Niederenergie- Photoelektronenspektroskopie an Fe_3O_4: Polaronische Physik und Verwey-Übergang*, Dissertation, Universität Augsburg (2005).

[102] S. Gota, J. B. Moussy, M. Henriot, M. J. Guittet, and M. Gautier-Soyer, Surface Science **482**, 809 (2001).

[103] T. Kendelewicz et al., Surface Science **453**, 32 (2000).

[104] S. A. Chambers and S. A. Joyce, Surface Science **420**, 111 (1999).

[105] T. Yamashita and P. Hayes, Applied Surface Science **254**, 2441 (2008).

[106] B. L. Henke, E. M. Gullikson, and J. C. Davis, Atomic Data and Nuclear Data Tables **54**, 181 (1993).

[107] H. Wende, Reports on Progress in Physics **67**, 2105 (2004).

[108] W. Kuch, *Abbildende magnetische Mikrospektroskopie*, Habilitationschrift, Universität Halle-Wittenberg (2002).

[109] H. Ebert, Reports on Progress in Physics **59**, 1665 (1996).

[110] K. Fauth et al., Physica Status Solidi B **247**, 1170 (2010).

[111] B. T. Thole, P. Carra, F. Sette, and G. Van der Laan, Physical Review Letters **68**, 1943 (1992).

[112] P. Carra, B. T. Thole, M. Altarelli, and X. D. Wang, Physical Review Letters **70**, 694 (1993).

[113] E. Goering, S. Gold, M. Lafkioti, and G. Schütz, Europhysics Letters **73**, 97 (2006).

[114] D. J. Huang et al., Physical Review Letters **93**, 077204 (2004).

[115] R. Nakajima, J. Stöhr, and Y. U. Idzerda, Physical Review B **59**, 6421 (1999).

[116] E. Pellegrin et al., Physica Status Solidi B **215**, 797 (1999).

[117] P. Kuiper, B. G. Searle, L.-C. Duda, R. M. Wolf, and P. J. van der Zaag, Journal of Electron Spectroscopy and Related Phenomena **86**, 107 (1997).

[118] C. Klingshirn, M. Grundmann, A. Hoffmann, B. Meyer, and A. Waag, Physik Journal **5**, 33 (2006).

[119] H. Morkoç and U. Özgür, *Zinc Oxide: Fundamentals, Materials and Device Technology*, Wiley-VCH, Weinheim, 1st edition (2009).

[120] S. Ghosh et al., Applied Physics Letters **86**, 232507 (2005).

[121] O. Dulub, L. A. Boatner, and U. Diebold, Surface Science **519**, 201 (2002).

[122] O. Dulub, U. Diebold, and G. Kresse, Physical Review Letters **90**, 016102 (2003).

[123] M. Valtiner, S. Borodin, and G. Grundmeier, Physical Chemistry Chemical Physics **9**, 2406 (2007).

[124] M. Valtiner, M. Todorova, G. Grundmeier, and J. Neugebauer, Physical Review Letters **103**, 065502 (2009).

[125] C. Wöll, Progress in Surface Science **82**, 55 (2007).

[126] M. Kunat, S. Gil Girol, T. Becker, U. Burghaus, and C. Wöll, Physical Review B **66**, 081402 (2002).

[127] B. J. Hopkins, R. Leysen, and P. A. Taylor, Surface Science **48**, 486 (1975).

[128] D. C. Reynolds et al., Journal of Applied Physics **95**, 4802 (2004).

[129] N. J. C. Ingle, A. Yuskauskas, R. Wicks, M. Paul, and S. Leung, Journal of Physics D: Applied Physics **43**, 133001 (2010).

[130] J. M. Van Hove, P. Pukite, P. I. Cohen, and C. S. Lent, Journal of Vaccum Science and Technology A **1**, 609 (1983).

[131] S. Barrett, *Image SXM 1.89: Image Analysis Software*, Surface Science Research Centre, Liverpool, www.liv.ac.uk/∼sdb/ImageSXM (2009).

[132] W. Weiss and W. Ranke, Progress in Surface Science **70**, 1 (2002).

[133] Y. Gao, Y. J. Kim, S. A. Chambers, and G. Bai, Journal of Vacuum Science and Technology A **15**, 332 (1997).

[134] E. Chason and T. M. Mayer, Critical Reviews in Solid State and Materials Sciences **22**, 1 (1997).

[135] L. Spieß, G. Teichert, R. Schwarzer, H. Behnken, and C. Genzel, editors, *Moderne Röntgenbeugung: Röntgendiffraktometrie für Materialwissenschaftler, Physiker und Chemiker*, Vieweg und Teubner, Wiesbaden, 2nd edition (2009).

[136] S. Macke, S. Brück, P. Audehm, and E. Goering, *ReMagX: x-ray magnetic reflectivity tool*, Max-Planck Institute for Metals Research, Stuttgart, www.mf.mpg.de/remagx.html (2010).

[137] A. Nielsen et al., Applied Physics Letters **93**, 162510 (2008).

[138] B. D. Cullity and S. R. Stock, *Elements of X-ray Diffraction*, Prentice Hall, Upper Saddle River, 3rd edition (2001).

[139] V. M. Kaganer, R. Köhler, M. Schmidbauer, R. Opitz, and B. Jenichen, Physical Review B **55**, 1793 (1997).

[140] P. Kidd, P. F. Fewster, and N. L. Andrew, Journal of Physics D: Applied Physics **28**, A133 (1995).

[141] P. Gay, P. B. Hirsch, and A. Kelly, Acta Metallurgica **1**, 315 (1953).

[142] C. W. Teplin et al., Applied Physics Letters **96**, 201901 (2010).

[143] B. Heying et al., Applied Physics Letters **68**, 643 (1996).

[144] R. J. Kennedy and P. A. Stampe, Journal of Crystal Growth **207**, 200 (1999).

[145] N. Rega, *Photolumineszenz von epitatktischen Cu(In,Ga)Se_2 Schichten*, Dissertation, Freie Universität Berlin (2004).

[146] M. A. Moram and M. E. Vickers, Reports on Progress in Physics **72**, 036502 (2009).

[147] P. Van der Sluis, Journal of Physics D: Applied Physics **26**, A188 (1993).

[148] V. V. Roddatis, D. S. Su, C. Kuhrs, W. Ranke, and R. Schlögl, Thin Solid Films **396**, 78 (2001).

[149] C. H. Chen, D. J. Werder, S.-W. Cheong, and H. Takagi, Physica C **183**, 121 (1991).

[150] P. Haasen, *Physikalische Metallkunde*, Springer, Berlin, 3rd edition (1994).

[151] F. Schäfers, M. Mertin, and M. Gorgoi, Review of Scientific Instruments **78**, 123102 (2007).

[152] M. Gorgoi et al., Nuclear Instruments and Methods in Physics Research Section A **601**, 48 (2009).

[153] A. Ruff, *Wachstum und Charakterisierung dünner Magnetit-Filme auf den oxidischen Substraten Magnesiumoxid und Zinkoxid*, Diplomarbeit, Universität Würzburg (2008).

[154] A. Müller et al., *Epitaxial growth of Fe_3O_4 thin films on ZnO and MgO substrates*, http://arxiv.org/abs/0911.3572v1 (2009).

[155] C. A. F. Vaz, D. Prabhakaran, E. I. Altman, and V. E. Henrich, Physical Review B **80**, 155457 (2009).

[156] L. S. Dake, D. R. Baer, and J. M. Zachara, Surface and Interface Analysis **14**, 71 (1989).

[157] D. Wett, A. Demund, H. Schmidt, and R. Szargan, Applied Surface Science **254**, 2309 (2008).

[158] E. Goering, M. Lafkioti, S. Gold, and G. Schütz, Journal of Magnetism and Magnetic Materials **310**, e249 (2007).

[159] M. Kallmayer et al., Journal of Applied Physics **103**, 07D715 (2008).

[160] F. Delille et al., Journal of Magnetism and Magnetic Materials **294**, 27 (2005).

[161] K.-H. Hellwege and A. M. Hellwege, editors, *Landolt-Börnstein: Magnetic and Other Properties of Oxides and Related Compounds*, volume 4 of *New Series*, Springer, Berlin (1970).

[162] R. B. Lal, Solid State Communications **4**, 529 (1966).

[163] D. Reisinger, *Magnetit in ultradünnen, epitaktischen Schichtsystemen für die Spinelektronik*, Dissertation, Technische Universität München (2004).

[164] C. T. Chen et al., Physical Review Letters **75**, 152 (1995).

[165] J. P. Crocombette, B. T. Thole, and F. Jollet, Journal of Physics: Condensed Matter **8**, 4095 (1996).

[166] V. N. Antonov, B. N. Harmon, and A. N. Yaresko, Physical Review B **67**, 024417 (2003).

[167] E. Goering, S. Gold, A. Bayer, and G. Schütz, Journal of Synchrotron Radiation **8**, 434 (2001).

[168] D. Kufer, *Wachstum und Charakterisierung von Magnetit auf Halbleitersubstraten*, Diplomarbeit, Universität Würzburg (2010).

[169] S. S. P. Parkin, R. Sigsbee, R. Felici, and G. P. Felcher, Applied Physics Letters **48**, 604 (1986).

[170] P. A. A. van der Heijden et al., Journal of Magnetism and Magnetic Materials **159**, L293 (1996).

[171] N. Pérez et al., Applied Physics Letters **94**, 093108 (2009).

[172] D. Schrupp et al., Annalen der Physik **13**, 78 (2004).

[173] J. Orna et al., Physical Review B **81**, 144420 (2010).

[174] M. Ferhat and K. Yoh, Applied Physics Letters **90**, 112501 (2007).

[175] E. J. Preisler, J. Brooke, N. C. Oldham, and T. C. McGill, Journal of Vacuum Science and Technology B **21**, 1745 (2003).

[176] G. Hollinger, R. Skheytakabbani, and M. Gendry, Physical Review B **49**, 11159 (1994).

[177] R. Claessen et al., New Journal of Physics **11**, 125007 (2009).

[178] D. H. Laughlin and C. W. Wilmsen, Thin Solid Films **70**, 325 (1980).

[179] M. Yoshimoto, H. Nagata, T. Tsukahara, and H. Koinuma, Japanese Journal of Applied Physics **29**, L1199 (1990).

[180] H. Koinuma and M. Yoshimoto, Applied Surface Science **75**, 308 (1994).

[181] N. C. Oldham, *Investigation of Spintronic Materials Systems: Deposition and Characterization*, PhD thesis, California Institute of Technology (2004).

[182] Y. B. Xu, E. T. M. Kernohan, M. Tselepi, J. A. C. Bland, and S. Holmes, Applied Physics Letters **73**, 399 (1998).

[183] R. Fiederling et al., Nature **402**, 787 (1999).

[184] A. J. Van Bommel, J. E. Crombeen, and T. G. J. Vanoirschot, Surface Science **72**, 95 (1978).

[185] P. K. Larsen and D. J. Chadi, Physical Review B **37**, 8282 (1988).

[186] A. Ohtake, Surface Science Reports **63**, 295 (2008).

[187] R. Moosbühler, F. Bensch, M. Dumm, and G. Bayreuther, Journal of Applied Physics **91**, 8757 (2002).

[188] Y. X. Lu et al., Physical Review B **70**, 233304 (2004).

[189] S. A. Chambers et al., Physical Review B **34**, 6605 (1986).

[190] E. Kneedler et al., Journal of Applied Physics **79**, 5125 (1996).

[191] M. Paul, *Oberflächenuntersuchungen am Übergangsmetalloxid Magnetit*, Diplomarbeit, Universität Augsburg (2005).

[192] Y. X. Lu et al., Journal of Applied Physics **97**, 10C313 (2005).

[193] T. Taniyama et al., Journal of Applied Physics **103**, 07D705 (2008).

[194] J. M. LeBeau, Q. O. Hu, C. J. Palmstrøm, and S. Stemmer, Applied Physics Letters **93**, 121909 (2008).

[195] G. Lelay, D. Mao, A. Kahn, Y. Hwu, and G. Margaritondo, Physical Review B **43**, 14301 (1991).

[196] J. D. W. Thompson et al., Journal of Applied Physics **104**, 024516 (2008).

[197] M. W. Ruckman, J. J. Joyce, and J. H. Weaver, Physical Review B **33**, 7029 (1986).

[198] Y. B. Xu et al., Physical Review B **58**, 890 (1998).

[199] T. Zhang et al., Applied Physics Letters **78**, 961 (2001).

[200] B. Sinkovic, E. Shekel, and S. L. Hulbert, Physical Review B **52**, R8696 (1995).

[201] D. J. Huang et al., Journal of Magnetism and Magnetic Materials **239**, 261 (2002).

[202] E. Vescovo, H.-J. Kim, and J. M. Ablett, Journal of Applied Physics **98**, 084507 (2005).

[203] H. J. Kim, J. H. Park, and E. Vescovo, Physical Review B **61**, 15284 (2000).

[204] H. J. Kim, J. H. Park, and E. Vescovo, Physical Review B **61**, 15288 (2000).

[205] J. Takaobushi et al., Physical Review B **76**, 205108 (2007).

[206] S. M. Sze and K. N. Kwok, *Physics of Semiconductor Devices*, Wiley-VCH, Hoboken, 3rd edition (2007).

[207] M. Paul et al., Physical Review B **79**, 233101 (2009).

[208] H. J. Grabke, ISIJ International **29**, 529 (1989).

[209] E. Wada et al., Applied Physics Letters **96**, 102510 (2010).

[210] Y. Li et al., Physical Review Letters **105**, 167203 (2010).

[211] S. M. Watts, K. Nakajima, S. van Dijken, and J. M. D. Coey, Journal of Applied Physics **95**, 7465 (2004).

[212] O. Kubaschewski and B. E. Hopkins, *Oxidation of Metals and Alloys*, Butterworths, London, 2nd edition (1967).

[213] Y. X. Lu et al., IEEE Transactions on Magnetics **41**, 2008 (2005).

[214] C. W. Wilmsen, Journal of Vacuum Science and Technology **19**, 279 (1981).

[215] T. J. Regan et al., Physical Review B **64**, 214422 (2001).

[216] S. Adachi, Journal of Applied Physics **58**, R1 (1985).

[217] C. Magen, E. Snoeck, U. Lüders, and J. F. Bobo, Journal of Applied Physics **104**, 013913 (2008).

List of own publications

- M. Paul, M. Sing, R. Claessen, D. Schrupp, and V. A. M. Brabers, *Thermodynamic stability, atomic and electronic structure of reduced Fe_3O_4(111) single crystal surfaces*, Physical Review B **76**, 075412 (2007).

- M. Paul, A. Müller, A. Ruff, B. Schmid, G. Berner, M. Sing, R. Claessen, and M. Mertin, *Probing the interface of Fe_3O_4/GaAs thin films by hard x-ray photoelectron spectroscopy*, Physical Review B **79**, 233101 (2009).

- R. Claessen, M. Sing, M. Paul, G. Berner, A. Wetscherek, A. Müller, and W. Drube, *Hard x-ray photoelectron spectroscopy of oxide hybrid and heterostructures: a new method for the study of buried interfaces*, New Journal of Physics **11**, 125007 (2009).

- A. Hofmann, X. Y. Cui, J. Schäfer, S. Meyer, P. Höpfner, C. Blumenstein, M. Paul, L. Patthey, E. Rotenberg, J. Bünemann, F. Gebhard, T. Ohm, W. Weber, and R. Claessen, *Renormalization of bulk magnetic electron states at high binding energies*, Physical Review Letters **102**, 187204 (2009).

- N. J. C. Ingle, A. Yuskauskas, R. Wicks, M. Paul., and S. Leung, *The structural analysis possibilities of reflection high energy electron diffraction*, Journal of Physics D: Applied Physics **43**, 133001 (2010).

- M. Paul, D. Kufer, A. Müller, S. Brück, E. Goering, M. Kamp, M. Kamp, J. Verbeeck, H. Tian, G. Van Tendeloo, N. J. C. Ingle, M. Sing, and R. Claessen, *Fe_3O_4/ZnO: A high-quality magnetic oxide-semiconductor heterostructure by reactive deposition*, Applied Physics Letters **98**, 012512 (2011).

- A. Müller, A. Ruff, M. Paul, A. Wetscherek, G. Berner, U. Bauer, C. Praetorius, K. Fauth, M. Przybylski, M. Gorgoi, M. Sing, and R. Claessen, *Fe_3O_4 on ZnO: a spectroscopic study of film and interface properties*, submitted to Thin Solid Films.